REPORT DOCUMENTATION PAGE

Form Approved OMB NO. 0704-0188

1. REPORT DATE (DD-MM-YYYY)	2. REPORT TYPE	3. DATES COVERED (From - To)
31-08-2015	Ph.D. Dissertation	-

4. TITLE AND SUBTITLE

Light Management in Nanostructures: Nanowire Solar Cells and Optical Epitaxial Growth

5a. CONTRACT NUMBER
W911NF-09-1-0473

5b. GRANT NUMBER

5c. PROGRAM ELEMENT NUMBER
611102

6. AUTHORS
Ningfeng Huang

5d. PROJECT NUMBER

5e. TASK NUMBER

5f. WORK UNIT NUMBER

7. PERFORMING ORGANIZATION NAMES AND ADDRESSES
University of Southern California
Dept of Contracts and Grants
University of Southern California
Marina del Rey, CA 90292 -6601

8. PERFORMING ORGANIZATION REPORT NUMBER

9. SPONSORING/MONITORING AGENCY NAME(S) AND ADDRESS (ES)

U.S. Army Research Office
P.O. Box 12211
Research Triangle Park, NC 27709-2211

10. SPONSOR/MONITOR'S ACRONYM(S)
ARO

11. SPONSOR/MONITOR'S REPORT NUMBER(S)
56801-MS-PCS.16

12. DISTRIBUTION AVAILIBILITY STATEMENT

Approved for public release; distribution is unlimited.

13. SUPPLEMENTARY NOTES

The views, opinions and/or findings contained in this report are those of the author(s) and should not contrued as an official Department of the Army position, policy or decision, unless so designated by other documentation.

14. ABSTRACT

This dissertation work studies the use of nanostructures to control the flow of light in two application areas: photovoltaics and material self-assembly, which are discussed in I and Part II, respectively.

The work in photovoltaics focuses on designing high-efficiency nanowire array solar cells. Nanowire arrays are a promising candidate for the next generation

15. SUBJECT TERMS

optical trapping, self assembly, optical forces

16. SECURITY CLASSIFICATION OF:			17. LIMITATION OF ABSTRACT	15. NUMBER OF PAGES	19a. NAME OF RESPONSIBLE PERSON
a. REPORT	b. ABSTRACT	c. THIS PAGE			Michelle Povinelli
UU	UU	UU	UU		19b. TELEPHONE NUMBER 213-740-8682

Report Title

Light Management in Nanostructures: Nanowire Solar Cells and Optical Epitaxial Growth

ABSTRACT

This dissertation work studies the use of nanostructures to control the flow of light in two application areas: photovoltaics and material self-assembly, which are discussed in I and Part II, respectively.

The work in photovoltaics focuses on designing high-efficiency nanowire array solar cells. Nanowire arrays are a promising candidate for the next generation of low-cost, high efficiency, flexible photovoltaic cells. Nanowire structures relax the lattice-matching constraints and allow the usage of materials with different lattice constants for multijunction cells. This opens up a much wider range of materials choices than for traditional, planar cells. The design of a high-efficiency cell involves two factors: optical absorption and carrier collection. In this dissertation, I first use the full-wave electromagnetic simulation to investigate the absorption properties of periodic nanowire arrays and provide the optimal designs in a single junction and a tandem wire-on-substrate cell configurations. I then study strategies for optimal carrier collection by finite-element method electronic device simulations. I optimize the p-n junction geometry, doping parameters, and surface passivation scheme. This work not only establishes the fundamental limits of nanowire solar cells' designs but also provides practical guidelines and solutions for high performance nanowire solar cell devices.

The work of material self-assembly is based on the light-assisted, templated self-assembly (LATS) technique developed in our group. In this method, we shine light through a photonic crystal (or template) to create an array of optical traps. The traps drive the self-assembly of nanoparticles into regular patterns. In this dissertation work, I discover the crucial effect of inter-particle interactions on the pattern formation of metallic particles in the LATS system. I envision the analogy between the optical assembly of nanoparticles and atomic level epitaxial growth and suggest that the system can be viewed as "optical eptaxial growth". I develop the modeling and simulation technique to explain and predict experimental results. Such model leads to the first successful demonstration of the optical assembly of a 2D periodic gold nanoparticle array.

LIGHT MANAGEMENT IN NANOSTRUCTURES: NANOWIRE SOLAR CELLS AND OPTICAL EPITAXIAL GROWTH

by

Ningfeng Huang

A Dissertation Presented to the
FACULTY OF THE USC GRADUATE SCHOOL
UNIVERSITY OF SOUTHERN CALIFORNIA
In Partial Fulfillment of the
Requirements for the Degree
DOCTOR OF PHILOSOPHY
(ELECTRICAL ENGINEERING - ELECTROPHYSICS)

May 2015

Dedication

To my parents, Baojian Huang, Ju Zhuang and Chen Zhang.

Thank you for all of your support along the way.

Acknowledgments

First of all, I would like to sincerely thank my research advisor, Professor Michelle Povinelli, for the privilege of starting my research career; I not only gained invaluable knowledge in the field of *photonics*, but also learned how to be a good scholar. Under her guidance, I was given the freedom to pursue my research in my own way. I wouldn't have joined the LATS project and written the second part of this dissertation without such freedom. It was always a great pleasure to work and discuss with her. Thanks for supporting and encouraging me through these years.

I would also like to thank the former and current Nanophotonics Group members. Chenxi Lin initially guided me into the solar cell modeling project and constantly provided comments and help until his graduation. He also served as a role model of a systematic and diligent researcher to me. Luis Javier Martínez, Eric Jaquay and Camilo Mejia achieved great progress on the LATS project, which makes the second half of this dissertation possible. They were also great mentors to lead me into this project. Luis and Eric spent a lot of time training me on the machines in the clean room and the optical setup in our lab. Luis also shared with me his expertise in photonic crystal design. Camilo always came up with fascinating ideas and insightful questions on the project. I also enjoyed working with Mehmet Solmaz, who put a great effort in emphasizing the importance of

experimental work; Jing Ma, who always impressed me with her confidence and efficiency; Roshni Biswas and Duke Anderson, who shared and discussed with me their very interesting work; and Shao-Hua Wu and Aravind Krishnan, who worked with me very hard in the last year to pick up the optical assembly project from me quickly.

I feel tremendously lucky to have had the opportunity to work with many outstanding professors and scholars at USC. I would like to express my gratitude towards them. In regards to the study on nanowire solar cell in Center for Energy Nanoscience (CEN), I thank Professor Dan Dapkus, Professor Chongwu Zhou and Professor Stephen Cronin as well as their group members for the continuous effort in growing, testing and improving nanowires. They continuously provided insight and comment from the experimental side which pushed my modeling work forward and towards a more realistic and accurate direction. I would also like to thank Maoqing Yao and Chunyung Chi from Dr Dapkus' group, Sen Cong and Anuj Madaria from Dr Zhou's lab, and Chia-Chi Chang and Shermin Arab from Dr. Cronin's group for their help and support in collaborative projects. For the optical epitaxial growth project, I would like to thank Professor Aiichiro Nakano's input on the simulation. I also would like to thank Professor Anthony Levi and Professor Wei Wu for serving on my qualifying exam and thesis defense committee.

Last, but certainly not least, I would like to thank my dear wife, Chen Zhang, for her unconditional love, support and encouragement. I also owe a great debt of gratitude to my parents, Baojian Huang and Ju Zhuang. They are always ready to offer whatever they have to support me moving forward, and I dedicate this dissertation to them.

Contents

List of Tables

List of Figures

Abstract

This dissertation work studies the use of nanostructures to control the flow of light in two application areas: photovoltaics and material self-assembly, which are discussed in I and Part II, respectively.

The work in photovoltaics focuses on designing high-efficiency nanowire array solar cells. Nanowire arrays are a promising candidate for the next generation of low-cost, high efficiency, flexible photovoltaic cells. Nanowire structures relax the lattice-matching constraints and allow the usage of materials with different lattice constants for multijunction cells. This opens up a much wider range of materials choices than for traditional, planar cells. The design of a high-efficiency cell involves two factors: optical absorption and carrier collection. In this dissertation, I first use the full-wave electromagnetic simulation to investigate the absorption properties of periodic nanowire arrays and provide the optimal designs in a single junction and a tandem wire-on-substrate cell configurations. I then study strategies for optimal carrier collection by finite-element method electronic device simulations. I optimize the p-n junction geometry, doping parameters, and surface passivation scheme. This work not only establishes the fundamental limits of nanowire solar cells' designs but also provides practical guidelines and solutions for high performance nanowire solar cell devices.

The work of material self-assembly is based on the light-assisted, templated self-assembly (LATS) technique developed in our group. In this method, we shine light through a photonic crystal (or template) to create an array of optical traps. The traps drive the self-assembly of nanoparticles into regular patterns. In this dissertation work, I discover the crucial effect of inter-particle interactions on the pattern formation of metallic particles in the LATS system. I envision the analogy between the optical assembly of nanoparticles and atomic level epitaxial growth and suggest that the system can be viewed as "optical eptaxial growth". I develop the modeling and simulation technique to explain and predict experimental results. Such model leads to the first successful demonstration of the optical assembly of a 2D periodic gold nanoparticle array.

Part I

Nanowire Solar Cells

Chapter 1

Introduction

1.1 Solar energy and photovoltaic cells

Energy is one of the most important technical issues nowadays. The power generation nowadays mainly relies on the burning of fossil fuels, which emits large amount of carbon dioxide and other pollution. More importantly, fossil fuel will eventually run out in the near future. In order to make sustainable development of the civilization and cause less harm to the environment, new sources of substitute clean energy are required.

Solar energy is an important alternative energy source to fossil fuel. Solar energy is the planet's most plentiful and widely distributed renewable energy source. All wind, fossil fuel, hydro and biomass energy have their origins in sunlight. The earth receives 120 petawatts (PW $=10^{15}$ W) of incoming solar radiation on the surface [4], which means the solar energy captured by the Earth in 80 minutes equals to the annual global energy consumption in the year 2012 [5].

A range of technologies have been developed to harness the abundant solar energy, such as solar heating, solar thermal energy, artificial photosynthesis and solar photovoltaics [6]. Solar photovoltaics technology is one of the most promising of them, which directly converts sunlight to electricity without any moving parts or environmental emissions. Solar photovoltaic power plants can be deployed comparatively faster and easier than other renewable energy power plants such as wind, hydro and solar thermal power. Moreover, since arid or semi-arid areas usually

are more suitable for building solar power stations, the occupation of large areas of land by large utility stations will not be a serious problem.

Despite all the technological advantages that a photovoltaics system has and dramatic market growth, total PV power is now around 138.9 GW (data from 2013 [7]), which is still small relative to the world's 5550 GW of installed electric generation capacity (2.55% for data from 2012 [8]). The most critical issue becomes economics. Over the past 20 years, the photovoltaic power industry has experienced drastic technology advances and price drops, however, the levelized cost of energy (LCOE) for PV plants is still above the range of conventional generation options and other renewable generation options such as wind plants, even taking into account the impact of the U.S. federal 30% investment tax credit [9].

The difficulty has always been converting solar energy in an efficient and cost-effective way. On one hand, the advance of technologies leads to very high efficiency solar cell devices with efficiencies very close to the Shockley-Queisser detailed balance limit. More sophisticated multiple junction solar cells have efficiencies far beyond the SQ limit. However, most high efficiency devices rely on expensive crystalline materials. On the other hand, emerging thin-film technologies produce lower cost but lower energy conversion efficiency. The lower efficiency results in higher installation cost, with the result that there is near cost parity at the installed-system level. So far, a solar photovoltaics system with high efficiency at low cost, which can challenge the LCOE of conventional generation options, has not been achieved.

1.2 Nanostructured solar cells

The nanostructured solar cells discussed in this dissertation are *nanowire array solar cells*, shown in Figure 1.1. They are made of a periodic array of semiconductor nanowires. Both the diameter and spacing between wires are below 1 micrometer. Because of the extended periodic structure, the device is fully compatible with current solar panels for large area solar energy harvesting.

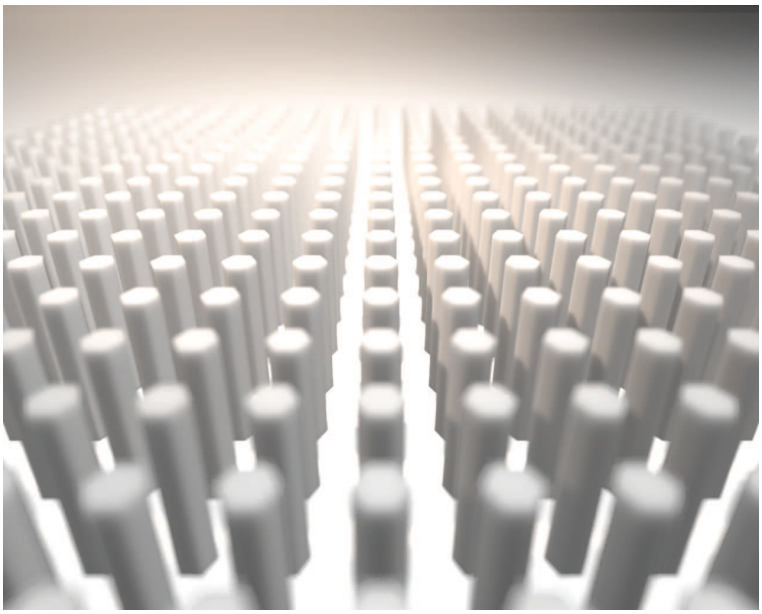

Figure 1.1: Rendering of a vertically-aligned semiconductor nanowire array.

The nanowire structure has been studied extensively in recent years, and it is advantageous for photovoltaic applications in several aspects. Firstly, by proper design, the nanowire structure can absorb the same amount or even a larger amount of light than a planar structure while using much less material, which greatly reduces the material and process cost. Secondly, the nanowire structure can relax the atomic lattice-matching constraints, enabling wider and more optimal material choices for multi-junction solar cells and yielding a higher efficiency. Non-lattice-matched growth of nanowire arrays also makes possible the growth of high quality

optoelectronic material such as gallium arsenide on a relative cheaper substrate such as silicon. Thirdly, the ultra-thin nanowire array structures are flexible and stretchable, which can enable novel applications in addition to the conventional solar power plant electricity generation.

Designing and modeling these miniature sub-micrometer nanowire solar cell devices are challenging. Optically, the sub-wavelength structure has intriguing and counter-intuitive properties which cannot be explained by the traditional ray-optics or effective-medium modeling approach. Full-wave electromagnetic simulation is required to get accurate results. Electrically, the nanowires are inherently three dimensional structures, different from the traditional planar, one-dimensional cells. This opens up larger design parameter space. Furthermore, nanowire structures have a much larger surface-to-volume ratio. Surface effects must be considered carefully, and a robust surface passivation scheme is required for high performance devices.

1.3 Outline of PART I

In the first part of the dissertation, I use accurate electromagnetic simulations coupled with electrical device simulations to provide design guidelines for nanowire array solar cells. Both the theoretical limit of perfect carrier collection and practical designs that consider non-ideal bulk and surface properties are discussed.

Chapter 2 focuses on a systematic study of the optical properties of semiconductor nanowire arrays made of various semiconductor materials for photovoltaic applications. It is shown that by optimizing the structural parameters, the nanowire array can absorb more sunlight than an equally-thick thin film made of

the same material. The height dependence of the absorption is also discussed, which is important for minimizing the material usage.

Chapter 3 presents the study of a III-V nanowire array on silicon, double-junction solar cell. Such a tandem solar cell is an ideal proof-of-concept model and key intermediate goal towards high efficiency, low cost, multijunction nanowire-array solar cells on cheap and lattice-mismatched substrates. In this chapter, I address the importance of current matching in nanowire-array-on-silicon solar cells and how to tune the parameter of the nanowire array to achieve current matching. The electrical consideration of the nanowire solar cell design is also discussed. The junction position and geometry affect the efficiency strongly. The radial junction outperforms the axial junction geometry in the case with bad surface quality.

To solve the issue of the inferior performance of the axial junction nanowire solar cells, which are essential building blocks for high efficiency multi-junction nanowire solar cells, in Chapter 4, I propose a high performance and robust surface passivation design to mitigate undesired surface effects.

Chapter 2

Broadband absorption of semiconductor nanowire arrays for photovoltaic applications

A version of the results in this chapter was published as Ref. [10].

2.1 Introduction

Semiconductor nanowire solar cells are promising candidates for next-generation, thin-film photovoltaic devices due to their attractive anti-reflection and light-trapping properties. Recent experimental work has demonstrated vertically aligned semiconductor nanowire arrays in silicon [11, 12, 13, 14, 15, 16, 17, 18, 19], germanium [20], various direct band gap materials [21, 22, 23, 24, 25, 26, 27, 28], and combined systems [29, 30, 31]. Nanowire arrays can be fabricated by either top-down [11, 12, 32] or bottom-up [13, 20, 22, 31] methodologies. By using different patterning techniques [20, 24, 25, 27, 33] regular arrays of nanowires have been achieved. Junctions have been made between semiconductor nanowires and substrate [22] and between the core and shell of semiconductor nanowires [23, 33]. Experiments on hybrid nanowire/polymer systems have also been conducted [34, 35].

In this section, we use electromagnetic simulations to map out the limiting efficiencies of nanowire solar cells. We focus on structures for which the nanowires themselves function as the broadband absorber. Ideally, a photovoltaic cell will absorb as large a fraction of incident photons as possible over the entire solar spectrum. Previous work has shown that the structural parameters of the nanowire array strongly influence the broadband absorption [36, 37]. Given proper design, light-trapping effects yield high broadband absorption, even for nanowire heights shorter than the bulk absorption length. Specifically, work from my group has shown that the ultimate efficiency of an optimized silicon nanowire array exceeds that of an equal-height thin film, even though it contains less absorptive material [37]. Similar optimization work has been carried out for silicon nanowires on silicon thin films [38], as well as for InP/InAs [39], InP [40] and GaAs/AlGaAs nanowire arrays [41].

However, previous work has been restricted either to a fixed height or to a very limited height range. The dependence of broadband absorption on height has not been determined. It is important to determine the extent to which light trapping can be used to minimize material usage while maintaining acceptably high photovoltaic efficiency. Material usage can have important implications for the cost of a process. For bottom-up growth methods such as MOCVD, for example, it is of particular interest to know what heights are sufficient to guarantee acceptable efficiencies, given the potentially time-consuming and expensive nature of the growth process. For photovoltaic space applications, the material volume affects the total weight, which correlates with the launch cost. From a scientific standpoint, it is of interest to determine how fast the efficiency degrades as the height of a nanowire array is reduced, in order to determine whether optimized structures will allow approach to an 'ultra-thin' film limit.

In this section, we systematically study the broadband absorption of vertically-aligned nanowire arrays made of six common photovoltaic materials. For each material, we study how the ultimate efficiency depends on the height of the array. At each value of height, we optimize the structural parameters of the array to maximize the broadband absorption. Thus, the results we present concisely describe the trade-offs between material usage and maximum achievable efficiency in semiconductor nanowire array solar cells. We further compare the optimized nanowire arrays to thin films of the same height and show that for all six materials, and over the entire range of heights tested (100 nm - 100 μm), the ultimate efficiencies of the arrays exceed those of equal-height thin films. Our results suggest that nanowire array solar cells hold strong potential for the development of next-generation, thin-film solar cells.

2.2 Methods

Figure 2.1 shows a schematic of a vertically-aligned semiconductor nanowire array. The array is illuminated by sunlight from the top, as indicated by the red arrow in Figure 2.1(a). The electric field of the incident light is polarized in either the x- or the y-direction. As shown in Figure 2.1(b), nanowires with diameter d are arranged in a hexagonal lattice with lattice constant a.

We consider nanowire arrays composed of one of six common photovoltaic materials. Among the materials considered, silicon and germanium are indirect band gap materials, while GaAs, InP, $In_{0.48}Ga_{0.52}P$, and CdTe are direct band gap materials. The optical constants (refractive indices and absorption lengths) are taken from the literature: Si [42], Ge [42], GaAs [42], InP [43], $In_{0.48}Ga_{0.52}P$ [44], and

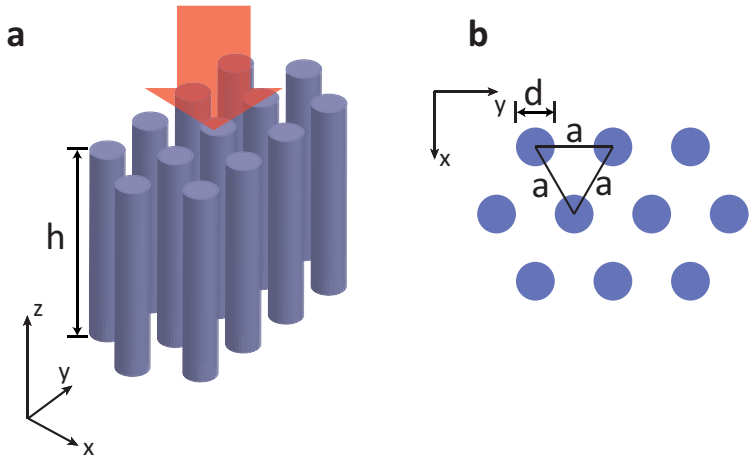

Figure 2.1: Schematic of a vertically-aligned semiconductor nanowire array. (a) Perspective view. (b) Cross-sectional view.

CdTe [45] (Figure 2.2). Si has a relatively large absorption length in the 400-1100 nm wavelength range compared to the other materials.

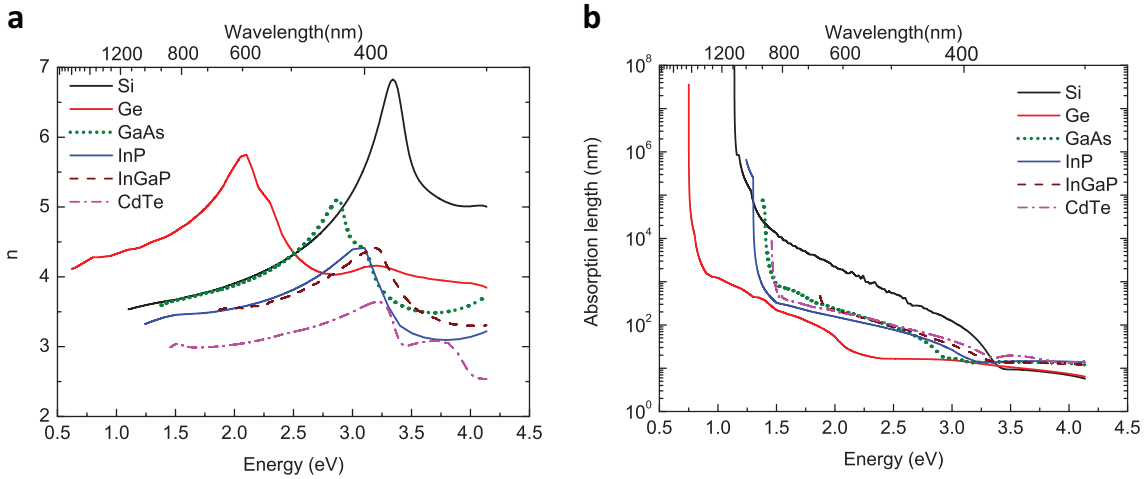

Figure 2.2: Materials' optical properties (a) Refractive indices (b) Absorption lengths.

We use the ISU-TMM simulation package [46, 47], an implementation of the transfer matrix method [48, 49], to calculate the broadband absorption of semiconductor nanowire arrays. The software can determine the wavelength-dependent

transmittance $T(\lambda)$ and reflectance $R(\lambda)$. The absorptance spectrum $A(\lambda)$ is obtained from the relation $A(\lambda) = 1 - T(\lambda) - R(\lambda)$. We average the results for x- and y-polarized incident light. The spectral resolution is chosen to be 5 nm in the wavelength range of interest.

We use the ultimate efficiency [50] to quantify the broadband absorption, as in previous work [36, 37]. The ultimate efficiency is given by

$$\eta = \frac{\int_{300\text{ nm}}^{\lambda_g} I(\lambda)A(\lambda)\frac{\lambda}{\lambda_g}\mathrm{d}\lambda}{\int_{300\text{ nm}}^{4000\text{ nm}} I(\lambda)\mathrm{d}\lambda} \tag{2.1}$$

where λ is the wavelength, and λ_g is the wavelength corresponding to the band gap of the semiconductor. $I(\lambda)$ is the ASTM AM1.5 solar spectral irradiance [1], which is plotted as a black line in Figure 2.3. $A(\lambda)$ is the absorption spectrum. We set the lower limit of integration to 300 nm in Equation 2.1 because the solar irradiance is negligible below this value. The ultimate efficiency is an upper bound on the achievable efficiency of a solar cell, assuming that each absorbed photon with energy greater than the band gap produces exactly one electron-hole pair at the energy of the gap, $E_g = hc/\lambda_g$. The ultimate efficiency can be related to the maximum short circuit current by assuming perfect carrier collection efficiency, i.e., every photogenerated carrier can reach the electrodes and contribute to the photocurrent. Within this approximation, we do not explicitly consider the junction geometry. In this case,

$$J_{sc} = \int_{300\text{ nm}}^{\lambda_g} I(\lambda)A(\lambda)\frac{e\lambda}{hc}\mathrm{d}\lambda = \eta\frac{e\lambda_g}{hc}\int_{300\text{ nm}}^{4000\text{ nm}} I(\lambda)\mathrm{d}\lambda \tag{2.2}$$

In the case of perfect absorption, we may set $A(\lambda) = 1$ in Equation 2.1 to obtain the limiting value of ultimate efficiency η_{max} [50]. The value of η_{max} is plotted as

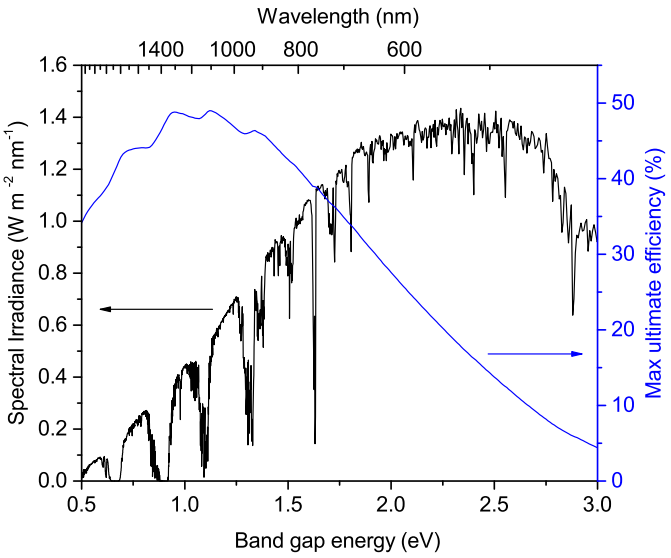

Figure 2.3: Direct+circumsolar spectral irradiance AM1.5 (black line), reprinted from Ref. [1], and the perfect-absorption limit of the ultimate efficiency (blue line).

a function of E_g in Figure 2.3 and obtains a maximum of 49% for a band gap of 1.12 eV.

For nanowire arrays, as for any realistic structure, the ultimate efficiency will always be less than η_{max} due to incomplete absorption. Below, we determine the extent to which structural optimization of a nanowire array can yield efficiency values approaching the perfect-absorption limit. Moreover, we determine the optimized ultimate efficiency as a function of nanowire height.

We optimize the ultimate efficiencies of nanowire arrays with respect to the structural parameters as follows. For fixed nanowire height h, we vary the lattice constant a and the ratio of the lattice constant to diameter, a/d. Seven height values were used: 100 nm, 300 nm, 1 μm, 3 μm, 10 μm, 30 μm and 100 μm. Figure 2.4 shows an example of a parameter sweep for 3 μm long silicon nanowire arrays. The lattice constant was varied from 200 to 1000 nm in steps of 100 nm and the a/d parameter was varied from 1 (for which the nanowires touch) to 4

in steps of 0.2. The value of the ultimate efficiency is given by the color bar and depends strongly on the structural parameters. In this specific case, the ultimate efficiency varies from a minimum of 5% to a maximum of 26% in the parameter space we consider. Below, we refer to the maximum value of ultimate efficiency, optimized over a and a/d for a particular material and nanowire height, as the optimized ultimate efficiency.

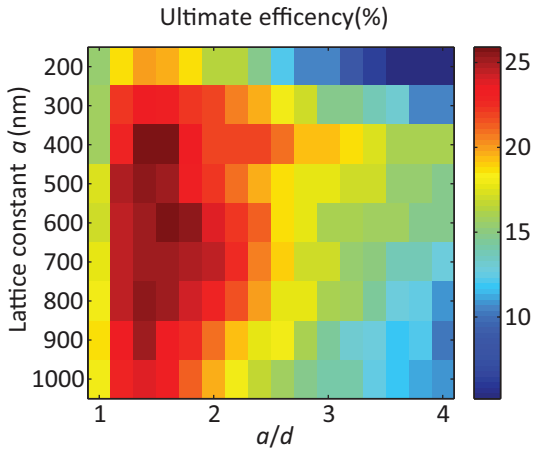

Figure 2.4: Optimization of the ultimate efficiency with respect to the structural parameters for a silicon nanowire array of 3 μm height.

2.3 Results and discussion

In Figure 2.5(a), we plot the optimized ultimate efficiency as a function of height for all six materials considered. For each material, the optimized ultimate efficiency increases with increasing height of the nanowire array. For the direct band gap materials (GaAs, InP, InGaP, CdTe), the ultimate efficiency increases quickly and is relatively flat for heights above 5 μm. For Si, which is an indirect band gap material, the ultimate efficiency slowly increases over the entire range shown (up to 100 μm). The data for Ge represent an intermediate case.

In Figure 2.5(b), we plot the optimized ultimate efficiency as a function of bandgap energy. The black solid line is the perfect-absorption limit of ultimate efficiency ($\eta_{\max}$), identical to the blue line in Figure 2.3. The colored symbols represent identical data to Figure 2.5(a). The data for each set of nanowire arrays are aligned to the bandgap energy of the constituent material. Different colors represent different heights of the nanowire array. From this plot, the saturation behavior of the ultimate efficiency may be clearly observed. For direct band gap materials, the optimized ultimate efficiency approaches the perfect-absorption limit much more quickly than for indirect band gap materials. For the materials studied, an optimized nanowire array of 3 μm height provides an ultimate efficiency that is >92% of the perfect-absorption limit for InP, GaAs, CdTe, and GaInP, while only 53% for Si and 78% for Ge.

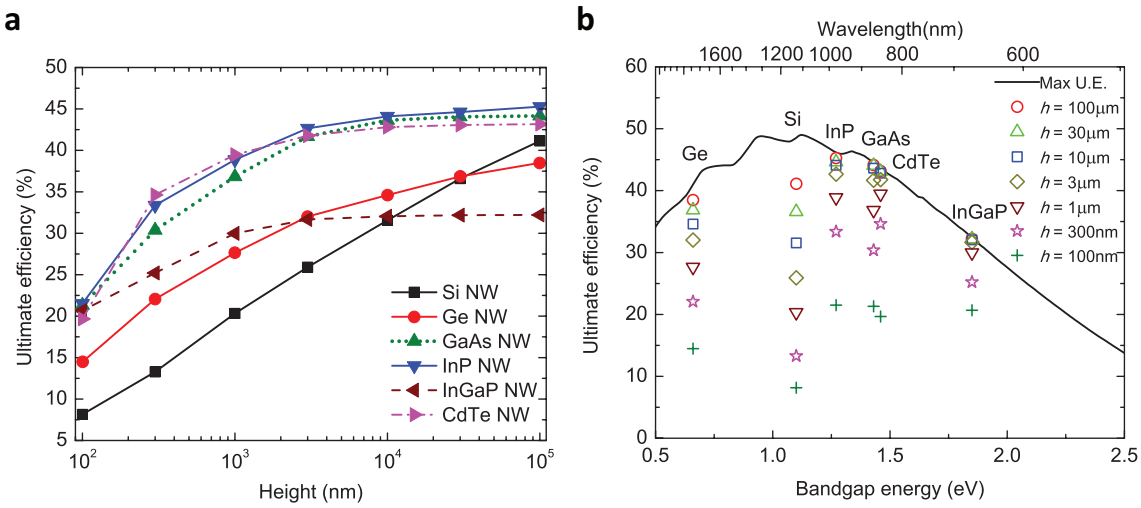

Figure 2.5: Optimized ultimate efficiencies for nanowire arrays composed of different materials: (a) shown as a function of array height; (b) shown as a function of the bandgap energy of the material.

Each data point in Figures 2.5(a) and (b) is obtained by optimizing the structural parameters of the nanowire array to maximize the ultimate efficiency. The

optimal values of a and a/d are shown in Figures 2.6(a) and (b), respectively. Different color lines represent different materials. From Figure 2.6(a), we observe that there is no obvious trend in the optimal lattice constant. However, most values are comparable to the wavelength of visible light ($\sim 400 - 700$ nm). Figure 2.6(b) shows that the optimal value of a/d increases with increasing nanowire height. Larger values of a/d correspond to sparser arrays. Intuitively, as the nanowire height increases, it becomes comparable to or larger than the absorption length in the material. In this limit that the nanowire height exceeds the absorption length over the whole solar spectrum, the ultimate efficiency will be maximized by minimizing the reflection from the top surface, which may be achieved by increasing a/d. From Figure 2.6(b), it may also be observed that the optimal value of a/d increases more quickly with length for direct band gap materials than for Si and Ge.

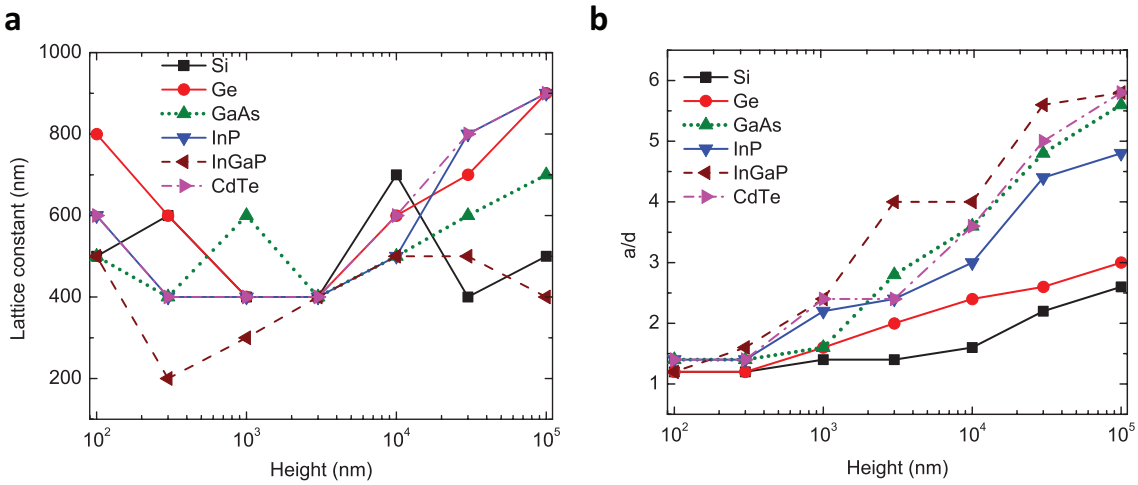

Figure 2.6: Optimal structural parameters for different heights of different materials: (a) lattice constant; (b)a/d ratio.

In Figure 2.7, we compare the performance of optimal nanowire arrays to thin films of the same height. The plot shows that in the entire height range we consider, optimal nanowire arrays have higher ultimate efficiencies than their thin-film

counterparts. This holds true even though the nanowires contain a smaller volume of absorbing materials than the thin films. Nanowire structures tend to have a lower reflection from their top surface than a thin film. Moreover, the nanowires can also couple normally incident light into modes that propagate in the plane of the array, a form of light trapping.

Above, we have considered free-standing nanowire arrays in air. The methods we use can be straightforwardly adapted to model particular choices of substrate material, contact geometries and materials. As one example of a more complex geometry, we consider the effect of a substrate on the ultimate efficiency. We choose GaAs as a representative direct band gap material and compare three possible substrate choices (no substrate, GaAs substrate, and glass substrate) using FDTD calculations. We assume that the solar cell is designed such that photogenerated carriers are collected only from the nanowire region. Hence, we calculate the ultimate efficiency using $A(\lambda)$ for the nanowire region alone. Absorption spectra, $A(\lambda)$, are obtained from the FDTD simulation by monitoring the flux difference between flux planes located above and below the nanowire array. We vary the height of the nanowire array as in the calculations above. For each height, we use the optimal structural parameters from Figure 2.6, which were obtained for the free-floating structure.

The black line in Figure 2.8 shows the ultimate efficiency of GaAs nanowire arrays without a substrate, corresponding to the green dotted line in Figure 2.5(a). The red and blue lines represent the ultimate efficiencies achieved for a GaAs and a glass substrate ($n = 1.55$) underneath the nanowires, respectively. As one would expect, the glass substrate has a smaller effect on the ultimate efficiency than the higher index, GaAs substrate. Moreover, we observe that when the height of the nanowire array is longer than about 3 μm, the effect of a glass or GaAs

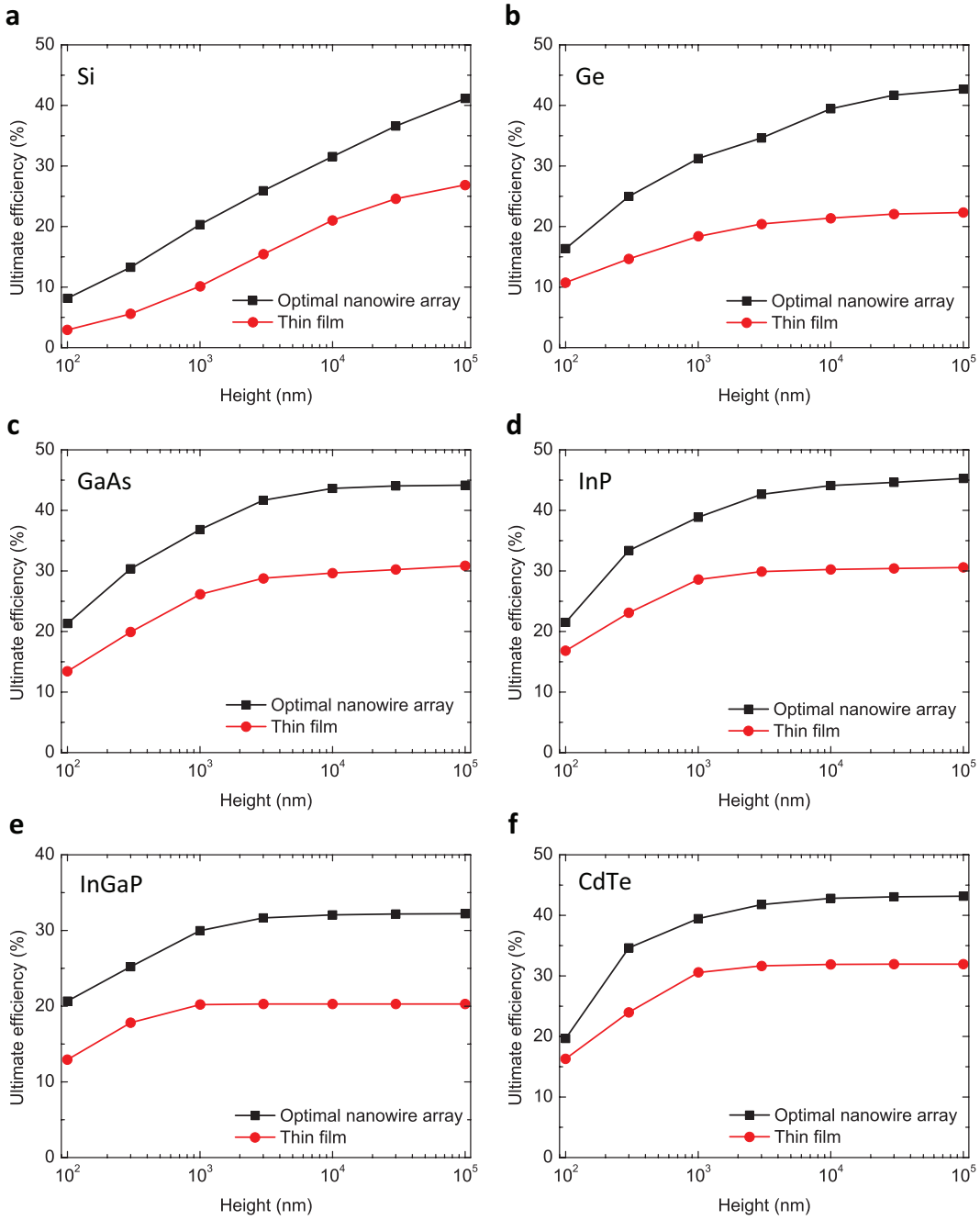

Figure 2.7: Comparison of the ultimate efficiencies of optimized (a) Si, (b) Ge, (c) GaAs, (d) InP, (e) InGaP, and (f) CdTe nanowire arrays with the ultimate efficiencies of thin films made of the same material and of the same height.

substrate on the ultimate efficiency is minimal. Intuitively, when the height of the nanowire array is large enough, most light will be absorbed without reflecting from the interface between the nanowires and the substrate. We observe that this height scale is similar to that at which the ultimate efficiency of the nanowire array approaches the perfect-absorption limit (Figure 2.5(b)). We note that the ultimate efficiencies shown by the blue and red lines in Figure 2.8 are not necessarily the maximum values achievable in the presence of a substrate; re-optimizing the structural parameters for a particular substrate of interest is likely to increase the ultimate efficiency.

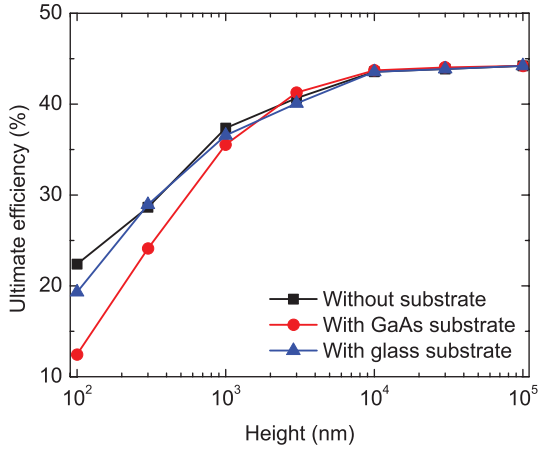

Figure 2.8: Effect of the substrate on the absorption in nanowire arrays.

2.4 Summary

In summary, we use electromagnetic simulation tools to quantitatively determine how the ultimate efficiency of optimized semiconductor nanowire arrays approaches the perfect-absorption limit as a function of nanowire height. Moreover, we demonstrate that optimized nanowire arrays in six different materials and for a range of heights from 100 nm to 100 μm all outperform unpatterned thin films

of equal height. The results will assist in the design of highly-efficient nanowire solar cells, while minimizing material usage.

In this chapter, we have considered nanowire arrays consisting of a single semiconductor material. Of the materials considered, GaAs, $In_{0.48}Ga_{0.52}P$ and Ge are commonly used in triple-junction solar cells. In the next chapter, we will extend our modeling to a III-V nanowire array on silicon dual-junction nanowire geometry. We will also incorporate both optical and electrical properties in a more detailed model to guide cell design.

Chapter 3

Limiting efficiencies of tandem solar cells consisting of III-V nanowire arrays on silicon

A version of the results in this chapter was published as Ref.[51]

3.1 Introduction

In the previous chapter, we have optimized the optical properties of single-junction nanowire arrays with respect to nanowire size and spacing. We showed that optimized arrays have a higher broadband absorption than a thin film of the same height, increasing efficiency while shrinking material usage.

Nanowire tandem cells promise further increases in photovoltaic efficiency [52, 53, 54]. Tandem solar cells use multiple semiconductor materials with different band gaps to selectively absorb different wavelength ranges of the solar spectrum, reducing thermal loss and increasing efficiency [55]. However, the choice of materials is traditionally constrained by lattice-matching requirements. Nanowire structures [56, 57, 58] have a high tolerance of lattice mismatch, enabling more material choices. Moreover, large-area fabrication of III-V nanowire arrays with controlled structural parameters has been successfully demonstrated using scalable patterning techniques such as nanosphere lithography [59].

In this chapter, we focus on double-junction cells in which the top junction is formed in a III-V nanowire array, and the bottom junction is formed in a silicon substrate. This system is promising for several reasons. First, III-V direct gap alloys are highly absorptive and provide a wide range of band gap choices. Recent experiments [53, 60, 61, 62, 63] have successfully demonstrated the fabrication of III-V nanowire arrays on relatively inexpensive silicon substrates. Second, this approach leverages previous development of highly optimized, single junction, crystalline silicon cells, used here as the bottom cell. Previous work in the literature has simulated a nanowire on silicon tandem cell for a III-V material with 1.7 eV band gap, assuming a simple Beer-Lambert model of absorption. Experiments have demonstrated a nanowire on silicon tandem cell in InGaAs [64], a material with a suboptimal bandgap. However, a number of important general questions remain. How should the nanowire array be designed to achieve current matching between top and bottom cell? How does the achievable efficiency vary with the band gap of the top material, and what nanowire size and spacing optimizes it? And lastly, how should the nanowire p-n junction be designed to achieve high carrier collection efficiency?

In this chapter, we first calculate the limiting efficiency of III-V nanowire on silicon tandem solar cells, using realistic 3D electromagnetic simulations to model absorption and a detailed-balance model to estimate current collection. We consider several choices of III-V material with different band gaps. For each, we find the optimal structural parameters (lattice constant and nanowire diameter) as a function of nanowire height. We discuss the implications of current matching on the array design. We then conduct more accurate device simulations, using finite element modeling of the drift-diffusion equations. We study the effect of the p-n junction design and surface recombination on carrier collection and compare to

the results of the detailed-balance model. Taken together, our results provide a comprehensive set of design guidelines for the optimization of III-V nanowire on silicon tandem cells.

3.2 Optical absorption modeling and detailed balance analysis

In this section, we use optical absorption modeling and detailed balance analysis [50] to estimate an upper bound on the efficiency of III-V nanowire on silicon tandem solar cells. We first consider the detailed balance limit for an idealized tandem cell. We then use three-dimensional, full vectorial simulations of Maxwell's equations to obtain the absorptance of various actual nanowire arrays. We optimize the nanowire structural parameters so as to provide tandem cell efficiencies as close as possible to the ideal limit. We describe how current matching conditions affect the optimal parameters for nanowire arrays composed of different materials, specifically those with band gaps above and below the ideal value.

3.2.1 III-V nanowire array on silicon structure

For the purpose of optical modeling, we consider the structure shown in Figure 3.1. The nanowires form a vertically aligned, hexagonal array, characterized by the distance between adjacent nanowires a, nanowire diameter d, and nanowire height h. We assume a semi-infinite silicon substrate. In practice, this means that the bottom silicon cell is assumed to be thick enough to absorb any light above its band gap that is not absorbed in the nanowire array. It is assumed that each subcell (nanowire array, silicon cell) contains a p-n junction, and that the two subcells are connected in series.

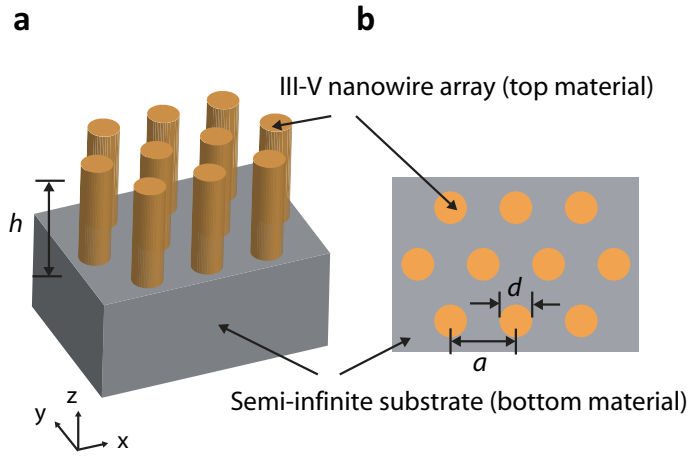

Figure 3.1: Schematic of a vertically aligned III-V nanowire array on a semiinfinite substrate. (a) Perspective view and (b) Top view.

We consider four different III-V materials for the nanowire array, each with a different band gap energy (InP 1.34 eV, GaAs 1.43 eV, $Al_{0.2}Ga_{0.8}As$ 1.72 eV, and $Ga_{0.5}In_{0.5}P$ 1.9 eV).

3.2.2 Detailed balance analysis

We use a modified detailed balance analysis to estimate the efficiency of the nanowire tandem solar cell. In each subcell, the short circuit current can be related to the absorptance by

$$J_{\mathrm{sc,i}} = \frac{e}{hc} \int_{310\ \mathrm{nm}}^{\lambda_{\mathrm{g,i}}} I(\lambda) A_{\mathrm{i}}(\lambda) \lambda \mathrm{d}\lambda \tag{3.1}$$

where the subscription i=1,2 represents the nanowire array or silicon substrate, respectively. Here, λ is the wavelength, λ_{g} is the wavelength corresponding to the band gap of the absorbing material, $I(\lambda)$ is the ASTM AM1.5D solar spectral irradiance [1], and $A_{\mathrm{i}}(\lambda)$ is the absorptance spectrum of the subcell. Equation 3.1

assumes one absorbed photon can generate one electron hole pair and perfect carrier collection, so represents an upper bound on the short circuit current.

We use the $J-V$ characteristic of an ideal diode to describe the electrical properties of each subcell

$$V_{\mathrm{i}}(J) = \frac{k_B T}{e} ln\left(\frac{J_{\mathrm{sc,i}} - J}{J_{0,\mathrm{i}}} + 1\right), \tag{3.2}$$

where $J_{0,\mathrm{i}}$ is the reverse saturation current density. In the detailed-balance analysis, $J_{0,\mathrm{i}}$ is calculated by assuming that the only loss process in the dark is radiative relaxation of electrons through spontaneous emission, which is in detailed balance with the absorption of ambient blackbody radiation at room temperature [50]. Absorption is assumed to occur at all photon energies above the semiconductor material's band gap. The reverse saturation current density can then be written as an integral of the Planck distribution,

$$J_{0,\mathrm{i}} = \frac{2\pi e}{h^3 c^2} \int_{E_{\mathrm{g,i}}}^{\infty} \frac{E^2}{exp(E/k_B T) - 1} \mathrm{d}E \tag{3.3}$$

The current matching condition dictates that because the two subcells are connected in series, the current density J is the same for both. The total $J-V$ curve can be obtained from

$$V_{\mathrm{total}}(J) = V_1(J) + V_2(J). \tag{3.4}$$

J cannot exceed the minimum J_{sc} of the two cells. Given $A_{\mathrm{i}}(\lambda)$ for each subcell, we can find the maximum power point on the $J-V$ curve numerically to determine the efficiency of the structure. Below, we calculate the efficiencies obtained from two models for $A_{\mathrm{i}}(\lambda)$: an idealized model based only on the band gap of the

material, and an accurate model based on full, electromagnetic simulations of the nanowire-on-silicon structure.

Detailed balance efficiency limit: Idealized model

Ideally, any incident photons with energy above the band gap of either the nanowire material or the silicon would be absorbed by the tandem cell structure and contribute to the current. However, in an actual structure, some photons are always reflected from the device and do not contribute. We first study ideal conditions to determine an upper bound on the tandem cell efficiency. Following the analysis in Ref. [65], we consider two cases: "perfect" absorption, where the nanowire array absorbs all incident photons with energy above its band gap, and "imperfect" absorption, where the nanowire array absorbs only a portion of such photons. We calculate the efficiencies for these two cases using the detailed balance analysis described above.

Figure 3.2(a) shows the case of perfect absorption. The efficiency is plotted as a function of the band gap energies of the top and bottom subcells. The highest limiting efficiency (45.3%) occurs when the band gaps of the top and bottom subcells are 1.57 eV and 0.935 eV, respectively. The dashed line shows the band gap for silicon (1.1 eV). For certain band gap combinations, shown as the blue, solid line in graph, the number of photons absorbed in the top layer is the same as the number of photons absorbed in the bottom layer. These cases provide current matching and yield higher efficiency. For band gap combinations below and to the right of the current matching line, the top cell's band gap is higher than optimal, and it limits the current due to insufficient absorption. For the band gap combinations above and to the left of current matching line, the top cell

absorbs too much light, limiting the amount of photons available for the bottom cell. In this case, the bottom cell limits the current.

We next consider the case of imperfect absorption. We choose the value of fractional absorption in the top cell to maximize the efficiency. The fractional absorption is defined as the percentage of photons with energy above the band gap of the top cell that are absorbed therein. Results are shown in Figure 3.2(b). In the region of the plot below the current matching line, 100% absorption is optimal. Above the line, imperfect absorption maximizes the efficiency. Figure 3.2(c) shows the efficiency obtained using the fractional absorption of Figure 3.2 (b). From the figure, it can be seen that in the region below and to the right of the current matching line, the limiting efficiencies are the same as those for perfect absorption case. However, in the region above and to the left of the current matching line, the efficiency is higher than for the case of perfect absorption. This is due to current matching constraints. By decreasing the absorption in the top cell, the solar flux can be evenly divided between the two subcells, yielding higher efficiency.

In Figure 3.2(d), we plot the efficiency values along the dashed lines in Figures 3.2(a) and 3.2(c), corresponding to the specific case where the bottom cell is silicon. We see that the ideal band gap value of the top cell is close to 1.7 eV. For a range of values below 1.7 eV, the limiting efficiency can be higher than 30% provided that the absorption in the top cell is optimized. This can be achieved in an actual nanowire structure by tuning the structural parameters, as investigated below.

Detailed balance efficiency limit: Full electromagnetic simulations

We next determine the efficiency limit of the nanowireon-silicon tandem cell using the calculated absorptance spectra for realistic nanowire structures. We optimize the detailed balance efficiency via an exhaustive scan over the structural

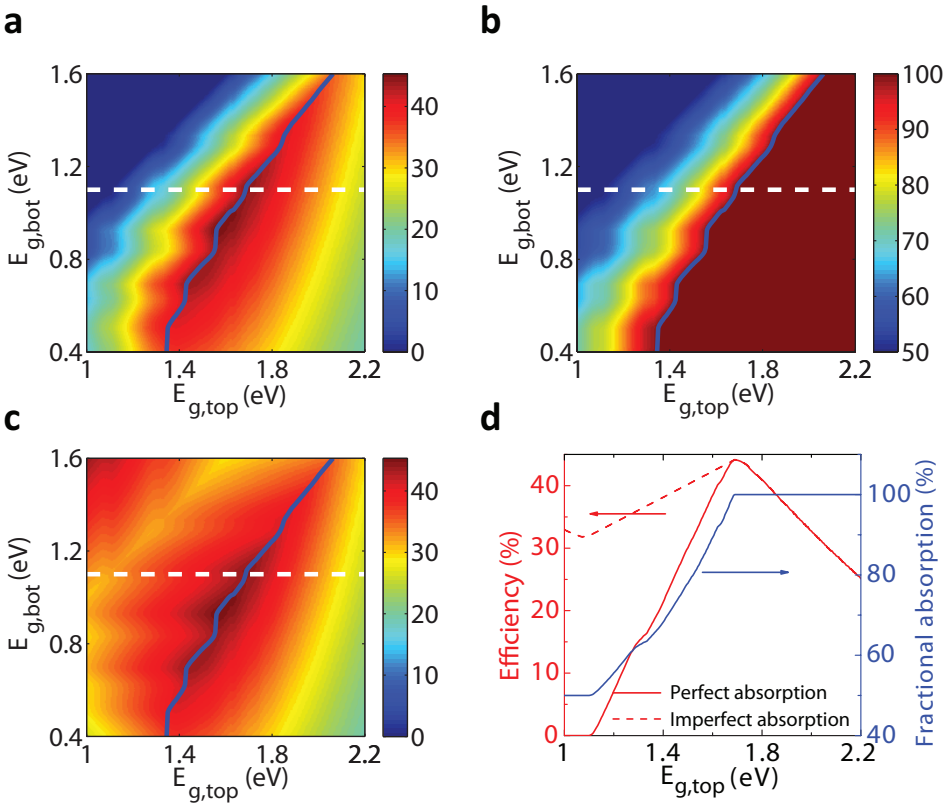

Figure 3.2: (a) Limiting detailed balance efficiency for double junction solar cells as a function of band gap energies assuming perfect absorption in the top cell. (b) Optimal fractional absorption in the top cell that maximizes the total efficiency. (c) Limiting detailed balance efficiency with optimal fractional absorption in the top cell given in (b). (d) Limiting efficiencies (left axis) and optimal fractional absorption (right axis) as a function of the band gap of the top cell, for a fixed bottom cell band gap energy of 1.1 eV (silicon), corresponding to the white, dashed lines in (a)-(c).

parameters (lattice constant a and d/a ratio) for each nanowire height h and for each nanowire material considered. We use a modified version of the ISU-TMM simulation package [46], an implementation of the scattering matrix method, to calculate the wavelength-dependent absorptance in both the nanowire array ($A_{\mathrm{NW}}(\lambda)$) and the silicon substrate ($A_{\mathrm{S}}(\lambda)$). The optical constants of each material (refractive index and absorption length) used in the simulation are taken from Ref. [45].

In Figure 3.3(a), we plot the optimized detailed balance efficiencies as a function of height for all four nanowire materials considered. We see that the efficiencies of InP and GaAs nanowire arrays peak at a relatively short height of $\sim$ 550 nm, while the efficiencies of the other two materials continue to increase with nanowire height, up to heights of 10 μm. Figure 3.3(b) shows the same set of data, where the efficiency values for each material are aligned with the band gap energy of the material. Different symbols represent different nanowire heights. The solid lines show the limiting efficiency.

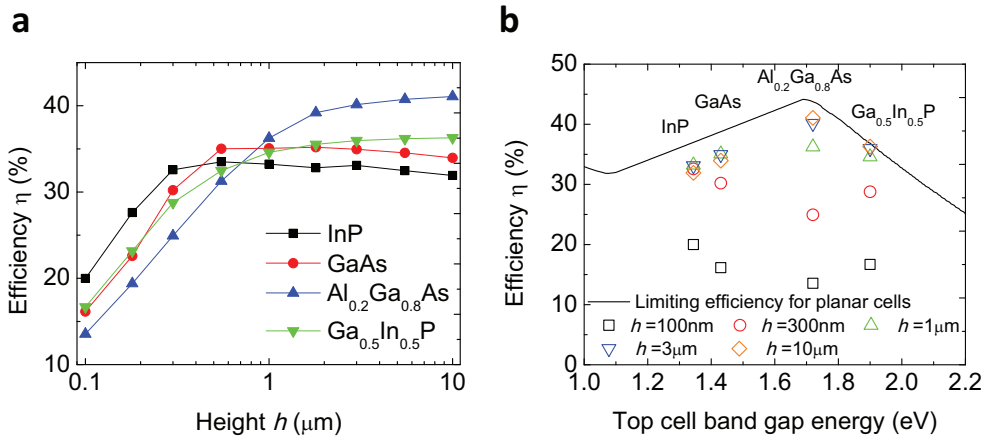

Figure 3.3: (a) Optimized detailed balance efficiency as a function of nanowire height for different nanowire materials. (b) Optimized detailed balance efficiency as a function of nanowire band gap energy for nanowire arrays of different heights. The solid lines give the limiting detailed balance efficiency, identical to the red dashed line in Figure 3.2(d).

Optical structural parameters

The optimized efficiencies in Figure 3.3 correspond to particular values of the nanowire structural parameters. These values are shown in Figure 3.4. For all four materials, the optimal lattice constant increases with height. For InP and GaAs, the optimal lattice constant increases more rapidly with height than for

AlGaAs and GaInP. The ratio of the diameter to the lattice constant (d/a) tends to decrease with height for all four materials. The optimal diameter has relatively little variation with nanowire height. The results indicate that as the nanowire height increases, the optimal array is sparser, corresponding to a smaller filling fraction.

For InP and GaAs, as the height increases, making the array sparser helps to reduce the fractional absorption in the top cell to the optimal value (shown in Figure 3.2(b)). For AlGaAs and GaInP, 100% absorption is desired. However, for larger heights, high absorption can be achieved with sparser wires, which simultaneously reduce reflection from the top surface.

The optimal structural parameters depend on the current matching constraint. In Figure 3.5, we consider 1.8 μm-tall GaAs and GaInP nanowire arrays as illustrative examples. GaAs has a bandgap energy of 1.43 eV, below the optimal band gap (1.7 eV), while GaInP has a bandgap of 1.9 eV, larger than optimal.

Figure 3.5(a) shows the percentage of photons with energy above the band gap of Si (1.12 eV) that are absorbed by the GaAs nanowire array (blue) and the silicon substrate (red) as a function of lattice constant (a) and d/a ratio. Depending on the structural parameters, the nanowire array absorbs either more or less light than the silicon substrate. Figure 3.5 shows the detailed balance efficiency map as a function of the structural parameters. Along the white line, the number of photons absorbed in the nanowire array and in the substrate is the same, and the efficiency is high. Note that the white line corresponds to the curve along which the two surfaces in Figure 3.5(a) cross.

For the GaInP case in Figure 3.5(c), no matter how we change the structural parameters, the absorption in the GaInP nanowire array is lower than the absorption in the silicon substrate. Figure 3.5(d) shows the efficiency map as a function

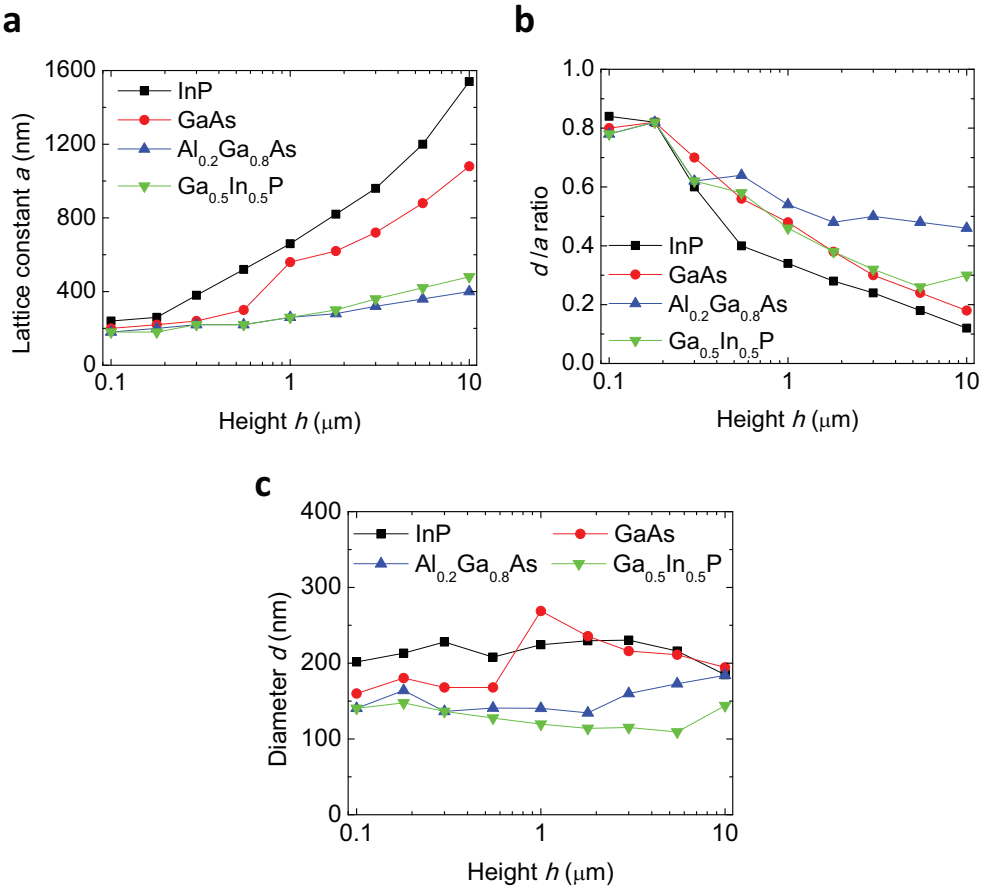

Figure 3.4: Optimal structural parameters for different materials as a function of nanowire height: (a) lattice constant a, (b)d/a ratio, and (c) diameter d.

of the structural parameters (efficiency value indicated by color bar). Overlaid on this plot are contours indicating the fractional absorption in the GaInP nanowire array (white lines/numbers). Note that the contour lines correspond to the data shown by the blue surface in Figure 3.5(c). The highest efficiencies occur when the absorption in the nanowire array is highest.

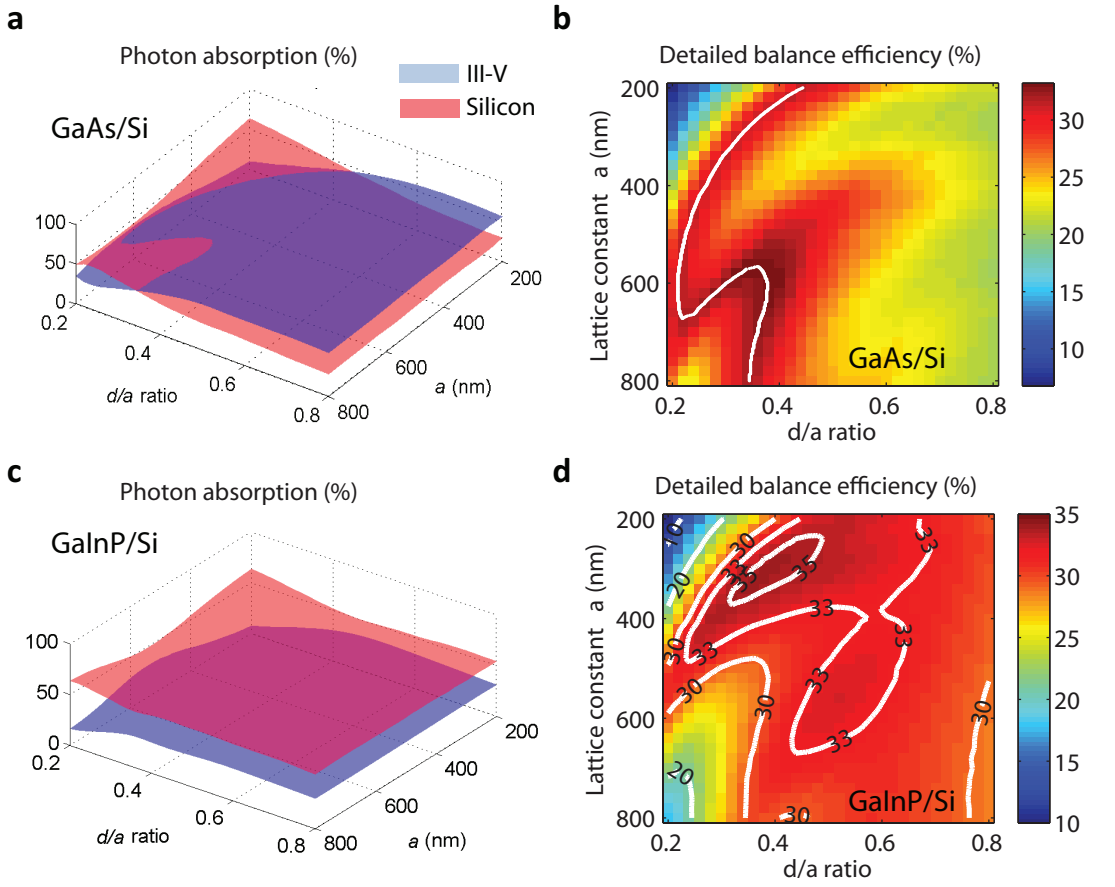

Figure 3.5: Relationship of photon absorption to detailed balance efficiency for materials with band gaps above and below the optimal value. (a) and (b) 1800 nm-tall GaAs NW array on silicon. (c) and (d) 1800 nm tall GaInP NW on silicon. (a) and (c) The percentage of photons with energy above the bandgap of silicon absorbed by the nanowire array (blue) and silicon layer (red) as functions of lattice constant and d/a ratio. (b) The detailed balance efficiency for the GaAs NW tandem cell. The white line indicates the structural parameters for which the percentage of photons absorbed in GaAs and silicon is equal. (d) The detailed balance efficiency for the GaInP NW tandem cell. Overlaid contours show the percentage of photons absorbed in GaInP.

We can relate the insight gained from Figure 3.5 to the difference in saturation behavior with height seen in Figure 3.3(a). For GaAs and InP, the highest efficiencies are obtained when the absorption in each subcell is the same, and perfect absorption in the nanowire array is not required. As a result, large nanowire heights are not necessary. For AlGaAs and GaInP, the largest efficiencies are obtained when the absorption in the nanowire array is maximized. This absorption increases with increasing height.

3.3 Electrical transport modeling

Above, we have used detailed balance analysis to find an upper limit on the efficiency of nanowire-on-silicon tandem cells, and we have found the nanowire structural parameters that optimize this efficiency. In this section, we show how electrical transport modeling can be used to design nanowire p-n junctions with efficiencies as close as possible to the detailed-balance limit. In particular, we compare radial and axial junction designs for a sample, GaAs nanowire array and compare the effect of surface recombination in the two types of junction.

3.3.1 Junction geometry

Figure 3.6 shows two possible junction geometries in the nanowires, radial (a) and axial (b). Transparent conductive oxide (TCO) and metal contacts are placed at the top and bottom of the structure. The structural parameters used in simulation come from the optimization of a GaAs nanowire array on silicon based on the detailed-balance model (a=560 nm, d=268 nm, and h=1 μm). Single-junction silicon solar cells have been the subject of extensive development. We thus focus on the transport properties of the upper GaAs nanowire cell, as shown

in Figures 3.7(a) and 3.7(b). In electrical simulations below, for the purpose of calculating nanowire $J-V$ curves, we will assume ideal ohmic contacts at the top and bottom of the nanowire.

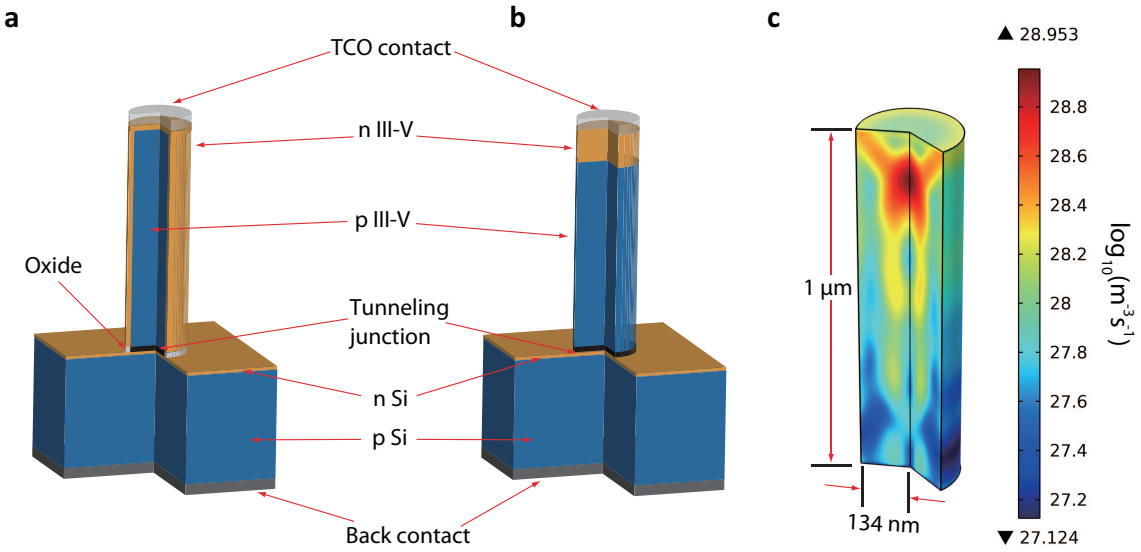

Figure 3.6: Junction designs for III-V NW on silicon tandem cells with (a) radial junction and (b) axial junction in the nanowire. The thickness of the silicon substrate is not to scale. (c) Carrier generation rate profile in GaAs nanowire.

3.3.2 Electrical transport simulation methods

In order to accurately simulate the $J-V$ response of nanowire solar cell, we first need to calculate the positiondependent carrier generation rate. The position-dependent absorptance normalized to incident power (P_{in}) in unit of (m^{-3}) is

$$A(\mathbf{r},\lambda) = \frac{1}{2}\omega\epsilon''|\mathbf{E}(\mathbf{r},\lambda)|^2/P_{\text{in}} \tag{3.5}$$

where ϵ'' is the imaginary part of the position-dependent permittivity. The electric field intensity is obtained by finitedifference time domain (FDTD) simulation using

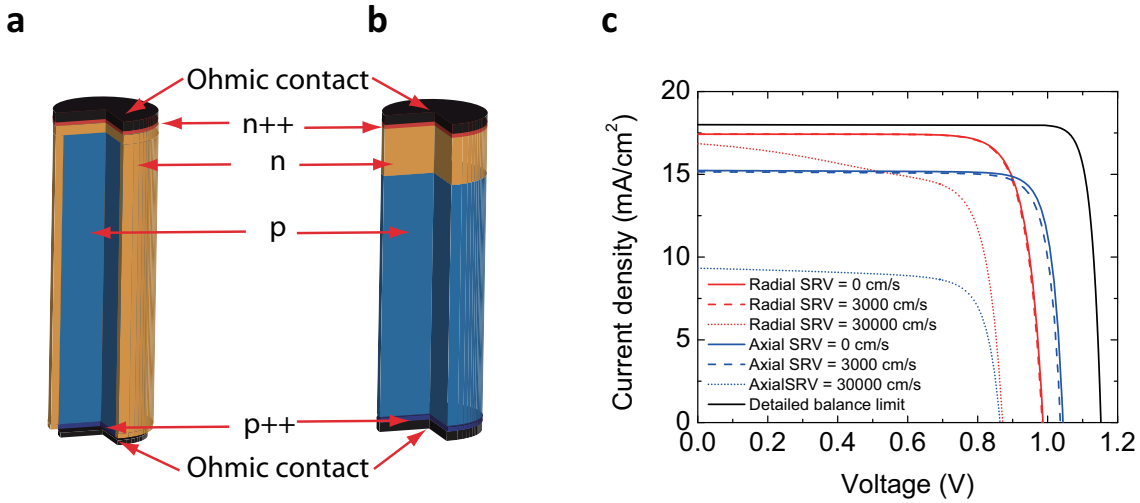

Figure 3.7: Simulated structures for (a) radial junction and (b) axial junction GaAs nanowire top cell. (c) $J-V$ curves for axial and radial junction geometries for varying SRV.

the Lumerical software package. Assuming that one photon generates one electron-hole pair, the position-dependent carrier generation rate can be calculated as

$$G(\mathbf{r}) = \int_{310\ \mathrm{nm}}^{867\ \mathrm{nm}} \frac{A(\mathbf{r},\lambda)I(\lambda)S\lambda}{hc}\mathrm{d}\lambda \tag{3.6}$$

where S is the unit cell area, $I(\lambda)$ is the AM1.5D solar irradiance, and hc/λ is the photon energy. We make the approximation that the field distribution in the nanowire is rotationally symmetric in order to reduce the problem to 2D. The 2D carrier generation rate is calculated using a circularly polarized source, which effectively time averages different incident polarizations. Figure 3.6 (c) shows the carrier generation rate profile. The effect of the contacts is not included in the optical simulations. We can see clearly that there is a highly concentrated hotspot at around 100 nm from the top surface.

We use the finite element method to calculate a realistic $J-V$ relation for the cell, given different p-n junction designs. In this part, we solve two current continuity equations (3.7) and (3.8) coupled with Poisson's equation (3.9) in COMSOL.

$$\nabla \cdot \mathbf{J}_{\mathrm{n}} = \nabla \cdot (n\mu_{\mathrm{n}} \nabla E_{\mathrm{F,n}}) = -e(G-R), \tag{3.7}$$

$$\nabla \cdot \mathbf{J}_{\mathrm{p}} = \nabla \cdot (p\mu_{\mathrm{p}} \nabla E_{\mathrm{F,p}}) = e(G-R), \tag{3.8}$$

$$\nabla^2 \psi = -e(p - n + N_{\mathrm{D}}^{+} - N_{\mathrm{A}}^{-}). \tag{3.9}$$

Here, μ_{n},μ_{p} are the electron and hole mobilities, and N_{D}^{+} and N_{A}^{-} are the donor and acceptor doping concentrations. G the carrier generation rate, from Equation 3.6. R the recombination rate. Here, only SRH recombination is taken into account in the simulation, and traps are assumed to be at mid-gap. SRH recombination can be written as

$$R_{\mathrm{SRH}} = \frac{np - n_{\mathrm{i}}^2}{\tau_{\mathrm{p}}(n + n_{\mathrm{i}}) + \tau_{\mathrm{n}}(p + n_{\mathrm{i}})} \tag{3.10}$$

where n_{i} is the intrinsic carrier density and τ_{n} and τ_{p} are the recombination lifetimes for electrons and holes, respectively. $E_{\mathrm{F,n}}$ and $E_{\mathrm{F,p}}$ are the quasi-Fermi energy levels for electrons and holes. Under Fermi statistics, the relation between electron and hole densities (n and p) and electron and hole quasi-Fermi energy levels ($E_{\mathrm{F,n}}$ and $E_{\mathrm{F,p}}$) are

$$n = N_{\mathrm{c}} \gamma_{\mathrm{n}} \exp\left(\frac{E_{\mathrm{F,n}} - E_{\mathrm{c}}}{k_B T}\right), \tag{3.11}$$

$$p = N_{\mathrm{v}} \gamma_{\mathrm{p}} \exp\left(\frac{E_{\mathrm{v}} - E_{\mathrm{F,p}}}{k_B T}\right), \tag{3.12}$$

where N_{c} and N_{v} are effective densities of states for the conduction band and valence band, respectively. E_{c} and E_{v} are the conduction and valence band edges. γ_{n} and γ_{p} are called "degeneration factors" and are defined as

$$\gamma_{\mathrm{n}} = F_{1/2}\left(\frac{E_{F,n} - E_c}{k_B T}\right) \Bigg/ \exp\left(\frac{E_{\mathrm{F,n}} - E_{\mathrm{c}}}{k_B T}\right), \tag{3.13}$$

$$\gamma_{\mathrm{p}} = F_{1/2}\left(\frac{E_{\mathrm{v}} - E_{\mathrm{F,p}}}{k_B T}\right) \Bigg/ \exp\left(\frac{E_{\mathrm{v}} - E_{\mathrm{F,p}}}{k_B T}\right), \tag{3.14}$$

where $F_{1/2}$ is the Fermi integral of order 1/2. Then Equations 3.7 and 3.8 can be expanded into

$$\frac{\nabla \cdot \mathbf{J}_{\mathrm{n}}}{-e} = \nabla \cdot (-D_{\mathrm{n}} \nabla n + D_{\mathrm{n}} n \nabla ln\gamma_{\mathrm{n}} + \mu_{\mathrm{n}} n \nabla \psi) = G - R, \tag{3.15}$$

$$\frac{\nabla \cdot \mathbf{J}_{\mathrm{p}}}{e} = \nabla \cdot (-D_{\mathrm{p}} \nabla p + D_{\mathrm{p}} p \nabla ln\gamma_{\mathrm{p}} + \mu_{\mathrm{p}} p \nabla \psi) = G - R, \tag{3.16}$$

where D_{n} and D_{p} are diffusion coefficients defined as $D_{\mathrm{n,p}} = \mu_{\mathrm{n,p}} k_B T/e$. Equations 3.9, 3.14, and 3.16 are three equations with three unknowns: electron density (n), hole density (p), and electrostatic potential (ψ). With proper boundary conditions, these coupled equations can be solved and the current-voltage response can be extracted from the solution. Note that γ_{n} and γ_{p} are defined by Equations 3.11-3.14.

The boundary conditions for electron and hole densities can be written as

$$\hat{\mathbf{n}} \cdot \mathbf{J}_{\mathrm{n}} = -ev_{\mathrm{th}}(n - n_0), \tag{3.17}$$

$$\hat{\mathbf{n}} \cdot \mathbf{J}_{\mathrm{p}} = ev_{\mathrm{th}}(p - p_0), \tag{3.18}$$

where $\hat{\mathbf{n}}$ is the outward normal to the nanowire surface. We have assumed that the carrier extractions are equal to the thermal velocity v_{th} and are set to 10^7 cm/s for both electrons and holes.

For an ideal ohmic contact, the potential ψ fixed by the external bias voltage (V_a),

$$\psi = \psi_0, \text{at the n contact} \tag{3.19}$$

$$\psi = \psi_0 + V_{\mathrm{a}}, \text{at the p contact} \tag{3.20}$$

where ψ_0 , n_0, and p_0 are the electrostatic potential, electron density, and hole density in thermal equilibrium, which can be solved by using Equations 3.9, 3.1, and 3.12, assuming that $E_{\mathrm{F,n}} = E_{\mathrm{F,p}} = E_{\mathrm{F}}$.

At the nanowire surface, the boundary conditions for n and p are

$$\hat{\mathbf{n}} \cdot \mathbf{J}_{\mathrm{n}} = -eR_{\mathrm{surf}} \tag{3.21}$$

$$\hat{\mathbf{n}} \cdot \mathbf{J}_{\mathrm{p}} = eR_{\mathrm{surf}} \tag{3.22}$$

where R_{surf} is the surface recombination rate. We assume SRH recombination with the traps at midgap. Then

$$R_{\mathrm{surf}} = \frac{v_{\mathrm{th}}\sigma_{\mathrm{n}}\sigma_{\mathrm{p}}(N_{\mathrm{dt}} + N_{\mathrm{at}})(np - n_{\mathrm{i}}^2)}{\sigma_{\mathrm{p}}(p + n_{\mathrm{i}}) + \sigma_{\mathrm{n}}(n + n_{\mathrm{i}})}, \tag{3.23}$$

where v_{th} is the thermal velocity of the carriers, σ is the trap cross section, and N_{dt} and N_{at} are the donor and acceptor-like trap density.

Because of the surface recombination, there is charge accumulation on the surface. The positive charges at the surface are caused by occupation of the donor-like states by holes and have the form

$$p_{\mathrm{s}} = \frac{N_{\mathrm{dt}}(\sigma_{\mathrm{n}} n_{\mathrm{i}} + \sigma_{\mathrm{p}} p)}{\sigma_{\mathrm{p}}(p + n_{\mathrm{i}}) + \sigma_{\mathrm{n}}(n + n_{\mathrm{i}})}. \tag{3.24}$$

The negative charges at the surface are caused by occupation of the acceptor-like states by electrons and have the form

$$n_{\mathrm{s}} = \frac{N_{\mathrm{at}}(\sigma_{\mathrm{p}} n_{\mathrm{i}} + \sigma_{\mathrm{n}} n)}{\sigma_{\mathrm{p}}(p + n_{\mathrm{i}}) + \sigma_{\mathrm{n}}(n + n_{\mathrm{i}})}. \tag{3.25}$$

The net surface charge density Q_{SS} is equal to $e(p_{\mathrm{s}} - n_{\mathrm{s}})$. The boundary condition for the electrostatic potential is

$$\nabla\psi = -\frac{Q_{\mathrm{ss}}}{\epsilon_0 \epsilon_{\mathrm{r}}}, \tag{3.26}$$

from Gauss' law.

In summary, solving the equations above yields the position-dependent potential (ψ), which is related to the applied voltage V and carrier concentrations (n and p), which can be used to calculate the current density J. Thus, the $J - V$ curve and efficiency can be obtained.

We carry out simulations using the parameters listed in Table 3.1. The electron and hole mobilities are assumed to have the same values as bulk materials, which are taken from Ref. [66]. SRH recombination lifetimes are taken from Ref. [67]. This set of parameters gives diffusion lengths of 15 μm for electrons and 3.87 μm for holes. The donor and acceptor concentrations are fixed to 1×10^{18} cm^{-3}. 10 nm-thick minority carrier reflectors with 1×10^{19} cm^{-3} doping concentration

Table 3.1: Device simulation parameters for nanowire top cells

Parameter	Description	Nominal values
d_{NW}	Diameter of nanowire	269 nm
h_{NW}	Height of nanowire	1000 nm
N_{c}	Effective density of states in conduction band	3.97×10^{17} cm^{-3}
N_{v}	Effective density of states in valance band	9.68×10^{18} cm^{-3}
μ_{n}	Electron mobility	2500 cm^2/Vs
μ_{p}	Hole mobility	150 cm^2/Vs
$\tau_{\mathrm{n}} = \tau_{\mathrm{p}}$	SRH recombination lifetimes	1 ns
N_{D}^{+}	Donor concentration (n-doping)	1×10^{18} cm^{-3}
N_{A}^{-}	Acceptor concentration (p-doping)	1×10^{18} cm^{-3}
N_{dt}	Surface donor like trap density	0, 1.5×10^{11} cm^{-2},$1.5\times$ 10^{12} cm^{-2}
N_{at}	Surface acceptor like trap density	0, 1.5×10^{11} cm^{-2},$1.5\times$ 10^{12} cm^{-2}
$v_{\mathrm{th}}^{\mathrm{n,p}}$	Thermal velocities for carriers	1×10^{7} cm/s
$\sigma_{\mathrm{n,p}}$	Trap cross-sections for carriers	1×10^{-15} cm^2
ϵ_{r}	Relative permittivity for GaAs	13.2

are put just below/above the top/bottom contacts to reduce recombination (shown as n++ and p++ regions in Figures 3.7(a)and 3.7(b)). We consider three kinds of surfaces here. The first case is a perfectly passivated nanowire surface. The second case is a surface with both donor and acceptor-like traps with densities of 1.5×10^{11} cm^{-2}. For this case, the surface recombination velocity (SRV) is 3000 cm/s, which has been demonstrated experimentally by AlGaAs passivation [68, 69]. The third case is a surface with poorer surface passivation, with donor and acceptor-like trap densities of 1.5×10^{12} cm^{-2}.

3.3.3 Design examples and results

Figure 3.7(c) shows sample $J - V$ curves for radial and axial junction geometries. For reference, we also plot the $J - V$ curve given by the detailed balance

limit. The junction depth is selected to be 35 nm for the radial junction and 100 nm for the axial junction. For no surface recombination (SRV=0 cm/s) and for low surface recombination (SRV =3000 cm/s), the radial junction has a higher short circuit current, while the axial junction has a higher open circuit voltage. The current density at zero voltage is higher for the radial junction because the distance required for carriers to diffuse to the junction is shorter, improving carrier extraction efficiency. However, the junction area is much larger for the radial junction than the axial junction. Therefore, under forward bias, recombination in the radial junction is more severe, reducing the open circuit voltage. When the surface recombination is severe (SRV=30,000 cm/s), the short circuit current of the radial junction is much larger than that of the axial junction. The open circuit voltages for both junctions have similar values.

From Figure 3.7(c), we can see that the radial junction is more tolerant to surface recombination than the axial junction. If the n-type shell is thin, most of the excess carriers are generated in p-region, which is protected from the surface. Once these electrons diffuse across the junction to become majority carriers, the effect of surface recombination is negligible. In contrast, for the axial junction, both n and p regions are exposed to surface.

Given the $J-V$ curve for a particular nanowire junction geometry, we calculate the maximum power and normalize by the maximum power for the detailed balance limit.

Figure 3.8 shows the normalized maximum power as a function of junction depth for radial and axial junctions from side wall and top, respectively, with the three cases of surface passivation considered above. In the case of no surface recombination, the radial junction's power increases with junction depth over the range shown. The axial junction's power reaches a maximum of 0.75 at a junction

depth of 260 nm and decreases as the junction depth is further increased. For low surface recombination (SRV=3000 cm/s), these trends remain without much power reduction. However, the drop in power in the axial junction is larger than in the radial junction. In the case with severe surface recombination, the difference is clearer. The normalized power of the radial junction is around 0.55 for a junction depth of 35 nm and drops with increasing junction depth. The axial junction can only achieve a normalized power of less than 0.35 with a junction depth of 100 nm. The optimal junction depth for the axial junction is close to the position of the absorption hotspot seen in Figure 3.6(c).

Two things are worth noticing here for the axial junction design. (1) Since the axial junction requires a long diffusion length of photogenerated carriers, high material quality and a carefully designed surface passivation technique may be required to achieve high efficiency. In this case, materials with band gap energy less than 1.7 eV are preferred because of their short optimal heights. (2) The performance of axial junction is sensitive to junction position, especially for the severe surface recombination case. Since the position of hot spot in Figure 3.6 (c) may vary in different structures, the optimal junction position may also vary.

3.4 Summary

In this chapter, we first use a perfect diode model to calculate the detailed-balance efficiency of III-V nanowire on silicon tandem solar cells. Our optimization results show that for all four III-V materials considered, a larger than 30% detailed-balance efficiency can be achieved by using 1 μm tall nanowire arrays with optimized lattice constants and diameters. For materials with bandgap smaller than the optimal value (1.7 eV), it is crucial to tune the structural parameters

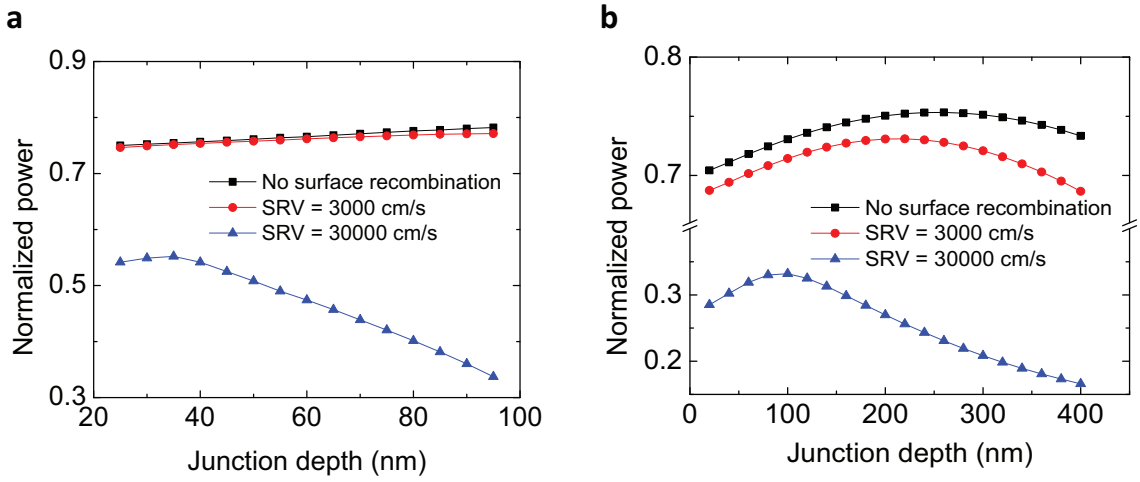

Figure 3.8: Normalized power of nanowire cells as functions of junction depth for (a) radial junction and (b) axial junction.

such that the number of absorbed photons in the top cell is no larger than the number absorbed in the silicon bottom cell. For materials with bandgap equal to or larger than optimal, the structural parameters should be tuned to maximize absorption in the nanowire cell.

We then conducted electrical transport simulations to illustrate how the output power of particular junction geometries, either radial or axial, compares to the detailed-balance limit. The simulation method allows for evaluation of the effects of surface recombination on output power. We find that the radial junction is more robust to the effects of surface recombination than the axial junction. For radial junction structures and a surface recombination velocity of 3000 cm/s, which has been achieved in experiments, the normalized power is decreased by less than 1.4% compared to the case of perfect surface passivation (no surface recombination). Our results indicate strong promise for high efficiency nanowire III-V tandem cells on silicon.

However, for the multiple junction nanowire solar cell, an axial junction is still preferable to a radial one. It is easier to stack different segments of the sub-cells in

the axial direction than to squeeze the different layers in the radial direction with only ~ 200 nm diameter. The result in Figure 3.7 also shows that the axial junction can potentially have higher open-circuit voltage if the surface issue is solved. In the next chapter, I will propose a design for a passivation layer on axial junction GaAs nanowire solar cells to mitigate the surface effect.

Chapter 4

Design of passivation layers on axial junction GaAs nanowire solar cells

A version of the results in this chapter was published as Ref.[70].

4.1 Introduction

Chapter 2 showed that periodic nanowire arrays possess ideal optical absorption properties for photovoltaic applications. Chapter 3 demonstrated that with the capability to provide natural strain relief, III-V nanowire arrays can be grown on lattice-mismatched silicon to construct double-junction solar cells with greatly enhanced efficiency. To further extend this approach, epitaxial growth techniques might be used to grow several segments of different III-V materials along the nanowire length. The material composition in each segment would be selected to obtain the ideal combination of bandgap energies for a multijunction cell [55, 71, 72]. Within each segment, the doping would be switched from p-type to n-type during growth to form an axial p-n junction. Such multijunction nanowire solar cells could potentially offer extremely high efficiencies, while relieving the lattice-matching constraints associated with planar junctions.

To achieve this vision, however, potential surface effects in the nanowires require careful consideration. Many III-V compounds such as gallium arsenide (GaAs) have a large density of surface states within the electronic bandgap. These mid-gap surface states have several negative effects on photovoltaic device performance [73, 74, 68, 69]. To date, experimental work has focused on the achievement of single-junction nanowire cells. Most reported works have adopted radial junctions [75, 76, 23, 77, 78, 79] to diminish surface effects. High-performance axial-junction nanowire solar cells have only been reported by using indium phosphide (InP) [80, 81, 53], a material known for its surface quality [82]. For GaAs, there has been previous investigation of surface passivation strategies to reduce detrimental surface effects [69, 76, 83, 84, 85, 86]. However, most of these efforts have been devoted to radial junction nanowires or uniformly doped nanowires only; little work has been done to deliberately investigate the effect of a surface passivation layer on an optimized axial p-n junction.

In this chapter, we demonstrate that high-efficiency axial junctions are feasible even for a material such as GaAs with poor surface quality. Specifically, we design a passivation scheme for axial junction GaAs nanowire-array solar cells using an AlGaAs shell layer. Using coupled optical and electrical simulations, we show that our passivation design greatly improves both the short-circuit current and open-circuit voltage relative to an unpassivated nanowire device, increasing efficiency by a factor of 2.7. Our surface passivation scheme should also enhance the performance of other axial junction nanowire devices, such as photodetectors, light-emitting diodes, field effect transistors, and tunneling diodes. Importantly, an extension of this approach to nanowires containing multiple junctions could open a path toward high-efficiency multijunction nanowire cells.

4.2 Passivation structure design

Figure 4.1(a) shows an axial-junction nanowire-array solar cell. We consider a periodic array of GaAs nanowires. Within each nanowire, an axial p-n junction is used to separate the photogenerated electron-hole pairs. Both the p-region and the n-region have exposed surfaces.

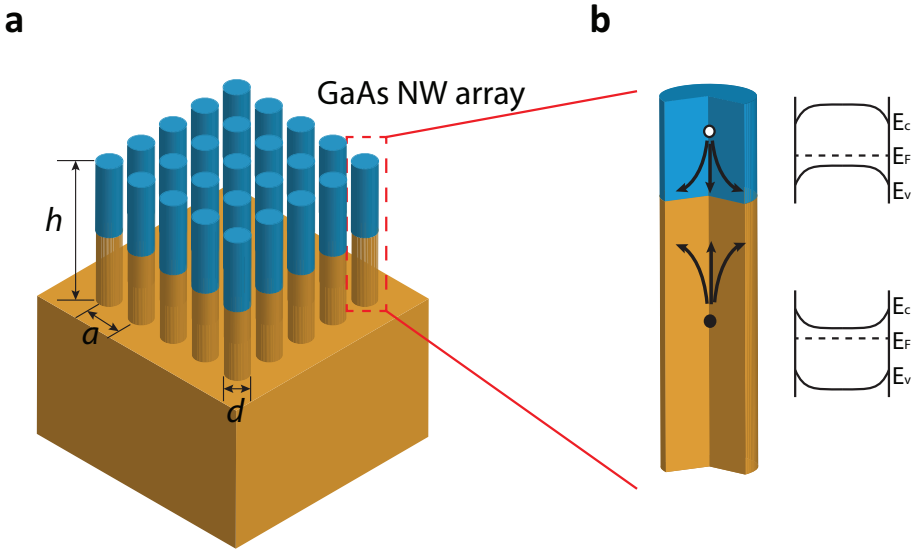

Figure 4.1: (a) Schematic of the axial junction GaAs nanowire-array solar cell on substrate. (b) Detailed illustration of the p-n junction and the direction of the generated carriers. (Insets show the band diagrams across the p and n regions.)

Due to the large surface-to-volume ratio of the nanowires, the surface has several negative effects on device performance. GaAs and many other III-V compounds have surface energy states within the bulk bandgap. The surface states deplete the majority carriers, bending the bands so as to shift the Fermi energy toward midgap, as shown in the insets to Figure 4.1(b). This effect increases the series resistance [69]. The induced field due to band bending also drives photogenerated minority carriers toward the surface, where they recombine, as shown by

the arrows in Figure 4.1(b). Due to these various surface effects, the efficiency of the nanowire solar cell decreases.

The goal of this chapter is to passivate the surface of an axial junction nanowire solar cell with a single epitaxial layer of uniformly doped material. We choose aluminum gallium arsenide (AlGaAs) for this purpose. Figure 4.2 shows our detailed design. For the core region, which is made of GaAs, we choose an intrinsic top segment and an n-type doped ($N_{\mathrm{D}} = 10^{18}$ cm^{-3}) bottom segment. The core region is covered with a 20-nm thick p-type doped ($N_{\mathrm{A}} = 10^{18}$ cm^{-3}) $Al_{0.8}Ga_{0.2}As$ shell. Carrier reflectors, made of 20-nm-thick heavily doped p and n GaAs (N_{A}=N_{D}=10^{19} cm^{-3}), are placed below/above the top/bottom contacts to reduce the recombination at the contacts.

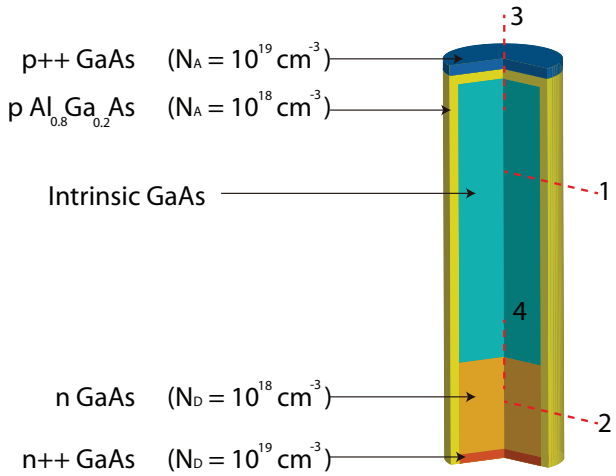

Figure 4.2: Specific passivation layer design and the doping concentration of each part.

As we show below, this design has the following features. First, AlGaAs with a high aluminum mole fraction has a large bandgap, which minimizes the optical loss in the shell. Second, AlGaAs creates large barriers for both electrons and holes throughout the structure, preventing the minority carriers from being recombined on the surface. Finally, the heterojunction between the p-type AlGaAs and the

intrinsic GaAs creates a p-type modulation doping in the GaAs region. The use of an intrinsic material maximizes the minority carrier diffusion length, ensuring a large short-circuit current.

In the following sections, we use coupled electromagnetic-electronic simulations to validate this design. We first introduce the modeling methods in Section 4.3. The optical performance of the passivation layer is discussed in Section 4.4. The device performance and the effects of the junction depth and surface recombination are shown in Section 4.5. Section 4.6 discusses the effects of the bulk lifetime on efficiency.

4.3 Methods

4.3.1 Optical simulation method

We use the finite-difference time-domain method (Lumerical Solutions, Inc.) to calculate the absorption profile in the nanowire as a function of position and wavelength, denoted $A(\mathbf{r}, \lambda)$. The optical constants of GaAs and AlGaAs used in the simulation (refractive index and absorption length) are taken from Ref. [45]. We assume the nanowires are placed on a semiinfinite GaAs substrate. The absorption spectrum $A(\lambda)$ is found by integrating over the nanowire:

$$A(\lambda) = \iiint_{\text{GaAs NW}} A(\mathbf{r}, \lambda) \mathrm{d}\mathbf{r}. \tag{4.1}$$

To obtain the carrier generation profile $G(\mathbf{r})$, we weight the absorption profile by the solar spectrum and assume that each photon absorbed generates one electron-hole pair:

$$G(\mathbf{r}) = \int_{300\ \text{nm}}^{\lambda_\mathbf{g}} \frac{A(\mathbf{r}, \lambda)\lambda}{hc} I(\lambda) S \mathrm{d}\lambda \tag{4.2}$$

where λ_g is the wavelength that corresponds to the semiconductor bandgap, h is Planck's constant, c is the speed of light in vacuum, $I(\lambda)$ is the AM 1.5D solar spectrum [1], and S is the area of the unit cell.

For a square array of nanowires, the absorption spectrum is independent of polarization at normal incidence. To reduce the size of the computation, we use a circularly polarized incident plane wave and approximate the generation profile as cylindrically symmetric. The generation profile is then exported to the device simulator as an excitation term.

4.3.2 Device simulation

We use Synopsys Sentaurus to model electrical transport in the device. The homojunction (core region) is simulated using a drift-diffusion model. The detailed simulation method for homojunctions is explained in Chapter 3. The heterojunction between AlGaAs and GaAs is modeled using the thermionic emission model [66]. The electron and hole currents (J_n and J_p) across the heterostructure have an exponential relation with the barrier heights (ΔE_c and ΔE_v):

$$J_n = a_n q \left[v_{n,2} n_2 - \frac{m_{n,2}}{m_{n,1}} v_{n,1} n_1 \exp\left(-\frac{\Delta E_c}{k_B T}\right) \right] \tag{4.3}$$

where a_n is an dimensionless coefficient, v_n is the emission velocity of the electrons (calculated using the equation $v_n = \sqrt{k_B T / 2\pi m_n}$),$n$ is the electron density, and m_n is the effective mass of the electrons. k_B is the Boltzmann constant, and T is the temperature set to be room temperature in the simulation. The subscripts 1

Table 4.1: Simulation parameters

Symbol	Description	Nominal values
$\mu_{\rm n}$,$\mu_{\rm p}$	electron and hole mobility	doping dependent [66]
$\Delta E_{\rm c}$	conduction band discontinuity between $Al_{0.8}Ga_{0.2}As$ and GaAs	0.315 eV [88]
$\Delta E_{\rm v}$	valance band discontinuity between $Al_{0.8}Ga_{0.2}As$ and GaAs	0.31 eV
$E_{\rm g,GaAs}$	band gap of GaAs	1.43 eV
$E_{\rm g,AlGaAs}$	band gap of $Al_{0.8}Ga_{0.2}As$	2.1 eV
$\tau_{\rm e}, \tau_{\rm h}$	SRH recombination lifetimes for electrons and holes	1 ns except in Figure 4.9
$D_{\rm dt}, D_{\rm at}$	surface donor, acceptor like trap densities	1.5×10^{12} cm^{-2} except in Figure 4.8
$a_{\rm n}, a_{\rm p}$	thermionic current coefficients	2
$m_{\rm n,GaAs}$	GaAs electron relative effective mass	0.067 m_0[a]
$m_{\rm p,GaAs}$	GaAs hole relative effective mass	0.485 m_0
$m_{\rm n,AlGaAs}$	AlGaAs electron relative effective mass	0.115 m_0
$m_{\rm p,AlGaAs}$	AlGaAs hole relative effective mass	0.598 m_0

[a] $m_0 = 9.1 \times 10^{-31}$ kg is the electron mass.

and 2 represent the materials with the lower and higher conduction band edges, respectively. A similar equation for the hole thermionic current is shown as follows:

$$J_{\rm p} = -a_{\rm p} q \left[v_{\rm p,2} p_2 - \frac{m_{\rm p,2}}{m_{\rm p,1}} v_{\rm p,1} p_1 \exp\left(-\frac{\Delta E_{\rm v}}{k_B T}\right)\right] \tag{4.4}$$

We assume that the interface between AlGaAs and GaAs is perfect without any additional recombination centers. This is usually valid for the lattice-matched epitaxy of AlGaAs on GaAs [87]. Surface recombination on the AlGaAs surface is modeled by surface traps at mid gap [51]. The donor-like and acceptor-like surface states are taken to have the same densities.

The parameters used in the device simulation are listed in Table 4.1.

4.4 Absorption properties of the design

We optimize the diameter and lattice constant of the nanowire array to maximize solar absorption. Figure 4.3 shows a map of the maximum achievable short-circuit current of a 3-μm-tall square array of GaAs nanowires on a semiinfinite GaAs substrate as a function of lattice constant (a) and diameter-to-lattice-constant (d/a) ratio. Only the absorption in the nanowire is considered here. The highest absorption is $\sim$25.93 mA/cm^2, which is achieved with a 320-nm lattice constant and a 160-nm diameter. This is close to the perfect absorption value of GaAs (27.94 mA/cm^2). We, therefore, adopt these parameters in our design.

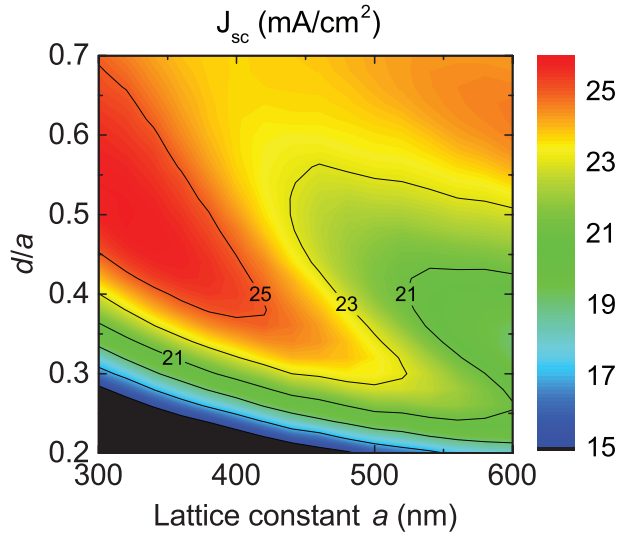

Figure 4.3: Maximum achievable short-circuit current of a square array of 3-μm tall GaAs nanowires as a function of lattice constant a and d/a ratio.

Figure 4.4 shows the carrier generation rate profiles for a nanowire in the array for a bare nanowire (a) and for a nanowire with a 20-nm passivation layer (b). We observe that the two structures have similar generation profiles within the core region. The generation rate in the AlGaAs shell is lower than that in the GaAs core. Figure 4.4(c) shows a magnified view of the top portion of the passivated

nanowire, indicated with the red dashed box in (b). We note that there is significant absorption in the thin p++ GaAs layer below the top contact. To investigate the spectral response, we plot the absorption spectra for the bare and passivated nanowires in Figure 4.5(a). Only the absorption in the core region is included. There is a large discrepancy between the two curves below 550 nm. However, the difference in absorption does not strongly affect carrier generation when the structures are illuminated by the solar spectrum. Figure 4.5(b) shows the absorption of the two structures weighted by the AM1.5D photon flux density. The photon flux under the blue curve (bare nanowire) is equivalent to a maximum current density of 25.93 mA/cm^2(as shown in Figure 4.3), while the one under the red curve (passivated NW) has a current density of 23.13 mA/cm^2.

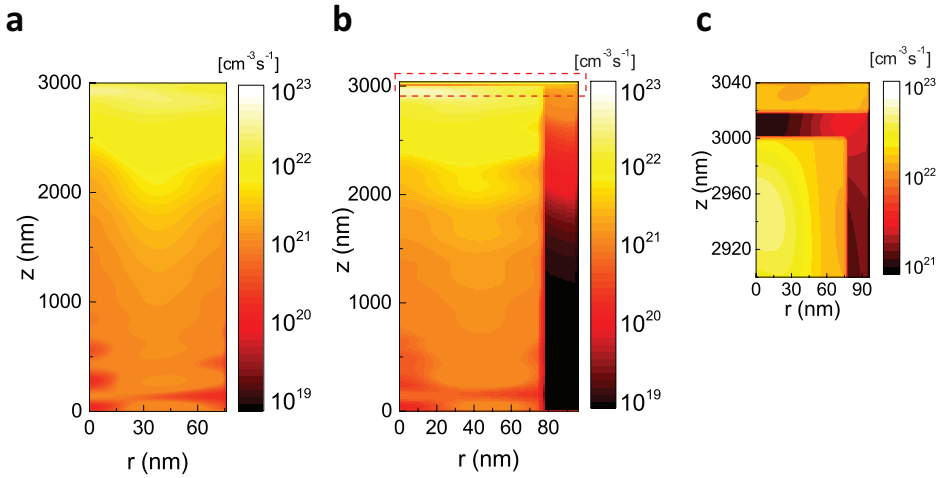

Figure 4.4: (a) Carrier generation rate profile in a bare GaAs nanowire. (b) Carrier generation rate profile in a passivated GaAs nanowire. (c) Magnified view of carrier generation rate profile near top of passivated GaAs nanowire.

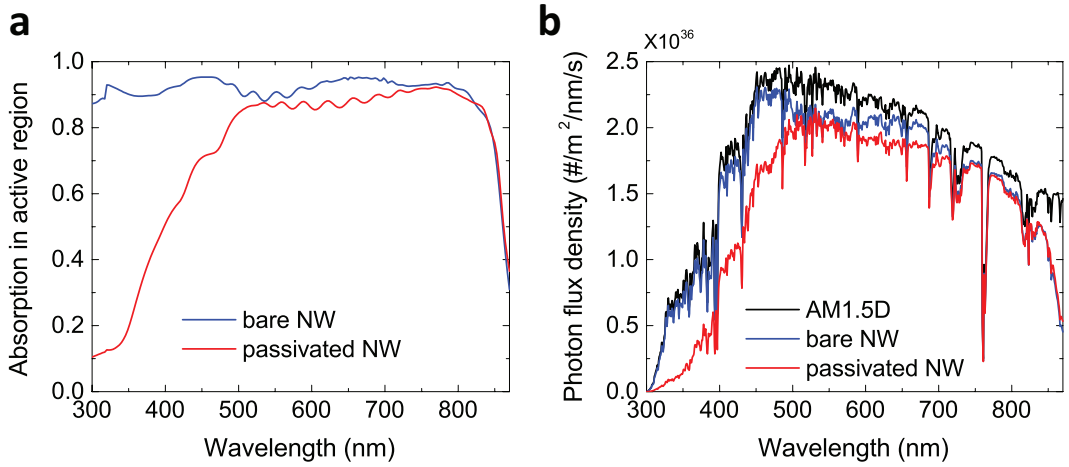

Figure 4.5: Effect of passivation layer on absorption in the nanowires. (a) Absorption spectra of GaAs NW array. (b) Absorbed photon flux densities (blue and red curves) shown relative to the incident photon flux density (black curve).

4.5 Carrier transport in the design

4.5.1 Band diagrams

We expect that the AlGaAs shell layer will form a barrier protecting both electrons and holes from reaching the nanowire surface. For $Al_{0.8}Ga_{0.2}As$, the commonly accepted value of the band offset at the GaAs/AlGaAs interface is approximately 0.3 eV for both the valence and conduction bands [88] (see Table 4.1). To investigate the effect of the shell layer on carrier transport, we first plot the electrostatic band diagrams in thermal equilibrium along the dashed lines in Figure 4.2. Figure 4.5(a)-(d) shows the diagrams for the lines running across the intrinsic region (dashed line 1), n-region (line 2), near the top contact (line 3), and near the junction (line 4), respectively.

It can be seen from Figure 4.6(a) that even though the core region (cyan) is intrinsic, the electrostatic Fermi level, shown as the dashed line, is very close to the valence band edge, indicating that the core region is effectively p-type doped.

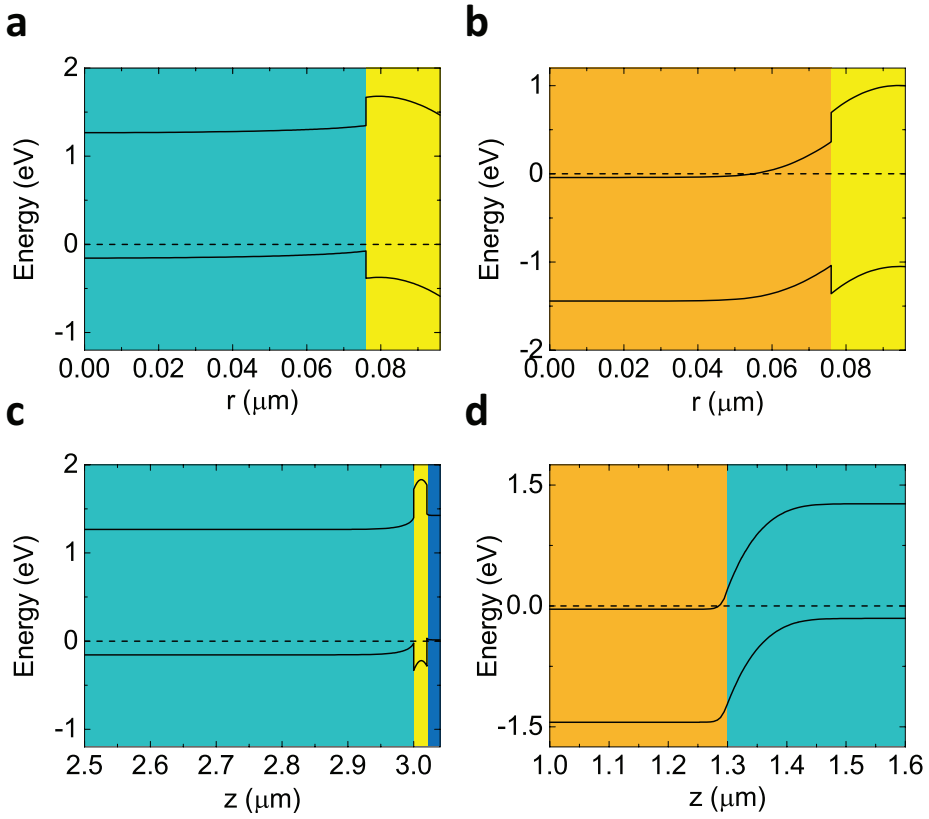

Figure 4.6: Band diagrams of the cross sections of (a) the intrinsic region, (b) the n-region, (c) below the top contact, and (d) near the junction, corresponding to dashed lines labeled 1, 2, 3, and 4 in Figure 4.2.

The effective doping concentration is 10^{16} cm^{-3}. This phenomenon is similar to modulation doping [89]. Because of the limited diameter of the core region (only ∼150 nm), the modulation dopants in the AlGaAs shell layer (yellow) dope the whole core, instead of only creating a doped layer near the surface. By placing the dopants in the shell, rather than in the carrier transport region, the design provides p-type behavior in the core with the long minority carrier diffusion length characteristic of an intrinsic material.

The band offset of the conduction band at the interface prevents generated minority electrons from being transported toward the surface, reducing surface recombination. Figure 4.6(b) shows the band diagram of the n-region (orange),

which is also covered by the p-type doped AlGaAs shell (yellow). The GaAs bands bend upward near the interface. However, due to the heavy doping of the core region, the space charge region only extends 10 nm below the interface. Most of the core region is still heavily doped and highly conductive.

Figure 4.6(c) shows the band diagram below the top contact. The thin layer of AlGaAs (yellow) between the nanowire (cyan) and the top contact (blue) serves as a carrier reflector to reflect generated minority electrons, reducing recombination at the top contact. There is a smaller barrier for the majority carriers (holes) below the top contact.

Figure 4.6(d) shows the band diagram near the interface between the n-type segment (orange) and the intrinsic segment (cyan). The interface is effectively a p-n junction, ensuring high open circuit voltage.

4.5.2 $J - V$ response

Figure 4.7(a) shows the $J - V$ curves for an optimized bare GaAs nanowire array device (blue line) and the device with the passivation layer (red line). For the passivated NW design, both the short-circuit current and the open-circuit voltage are much higher than for the bare nanowire(see Figure 4.7(a)). The surface passivation results in a 2.7 times higher efficiency. The optimized bare nanowire design had a top-n/bottom-p structure with 10^{17} cm^{-3} doping concentrations for both n- and p-regions. The junction depth was optimized with respect to power conversion efficiency, as shown in Figure 4.7(b). For the bare nanowire, the optimal junction depth is very close to the top surface at ~ 200 nm, close to the generation hot spot shown in Figure 4.4(b). The power conversion efficiency drops quickly with the junction depth. For the passivated NW, the efficiency is less sensitive to the junction depth, and the optimal depth is around 1.8 μm.

Figure 4.7(a) also shows the $J-V$ curves for the Shockley-Queisser limit [50], either for perfect absorption (gray, dashed line) or simulated absorption (black, solid line). The short-circuit current of the passivated NW design is close to the Shockley-Queisser limit with simulated absorption, indicating efficient carrier collection. However, the open-circuit voltage is substantially lower than the Shockley-Queisser limit. This is mainly due to the low effective doping (10^{16} cm^{-3}) in the intrinsic segment, which reduces the voltage drop across the p-n junction. However, the mobility increases with decreasing doping. As a result, the use of an intrinsic region, rather than a p-type doped region, also increases the minority carrier diffusion length and, thus, improves the minority carrier collection. The design represents a trade off between these two effects. We note that a high shell doping concentration is essential for achieving high efficiency. For a reduced shell doping concentration of 10^{17} cm^{-3}, the efficiency drops to 18.56% (compared with 21.26% at a shell doping of 10^{18} cm^{-3}). There is also a large discrepancy between the short-circuit current of the passivated NW design and the Shockley-Queisser limit assuming perfect absorption of photons above the bandgap of GaAs. This is mainly due to the incomplete absorption of the photons [10].

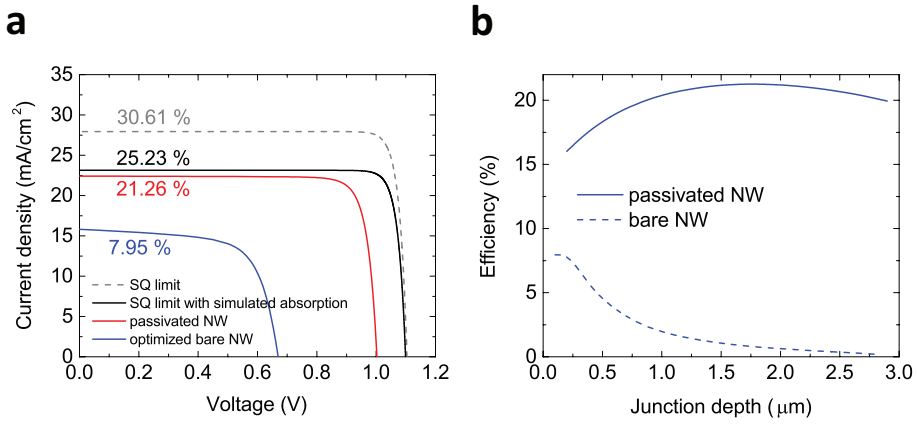

Figure 4.7: (a) $J-V$ curves for nanowire arrays without (blue) and with (red) the passivation layer. (b) Efficiencies as functions of junction depths.

Figure 4.8 shows the short-circuit current, open-circuit voltage, and efficiency as functions of the surface state density. We vary the surface state density from 1.5×10^9 to 1.5×10^{15} cm^{-2}, corresponding to surface recombination velocities from 3 to 3×10^7 cm/s. All three characteristics vary weakly as the surface state density changes by six orders of magnitude.

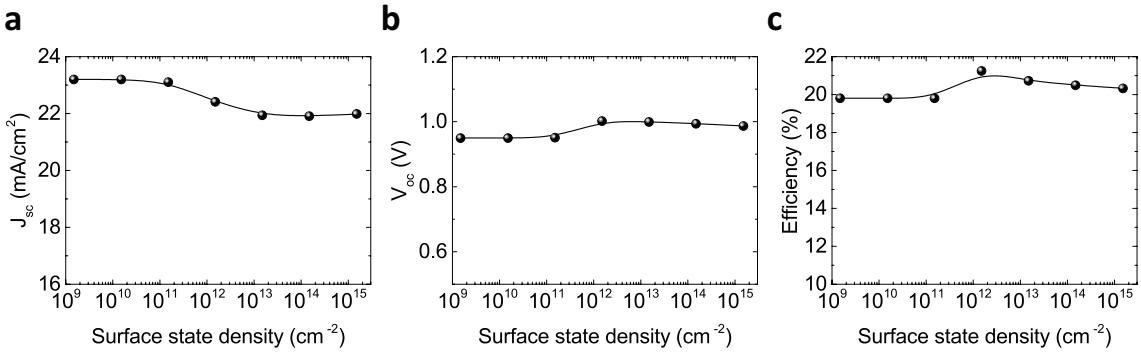

Figure 4.8: (a) Short-circuit current, (b) open-circuit voltage, and (c) efficiency as functions of surface state density.

4.6 Discussion

So far, we have assumed that the Shockley-Read-Hall recombination life time within the bulk is 1 ns, which is a reasonable estimate [86]. State-of-the-art growth techniques, such as MOCVD, can produce GaAs with high material quality, and the longest life time achieved in bulk structures is much greater than 1 ns [90]. The bulk diffusion lengths of the minority electrons and holes used in the calculations above are 4.6 μm and 935 nm, respectively, and are comparable with the nanowire height. However, for the bare nanowire, surface recombination effectively reduces the diffusion length below the bulk value, preventing carriers from being collected at the contacts. The key function of the AlGaAs passivation layer is to prevent surface recombination, increasing collected current.

For shorter values of the bulk diffusion lengths, the efficiency of the solar cell will decrease. To illustrate this, Figure 4.9 shows the power conversion efficiency as a function of junction depth for different bulk SRH recombination lifetimes. Figure 4.9(a) shows the efficiency for the passivated nanowire structure. The blue curves are the same as the curves in Figure 4.7(b). The red and black curves show the efficiency when the SRH lifetime is reduced to 0.1 and 0.01 ns, respectively. The corresponding minority electron diffusion lengths are 1.45 μm and 460 nm, respectively. The highest achievable efficiency drops with decrease in bulk diffusion length, and the optimal junction depth moves toward the top contact. When the diffusion length is shorter than the nanowire, placing the junction near the position where the most carriers are generated results in the largest current. Conversely, for larger values of the bulk diffusion length, the efficiency of the solar cell increases, and the optimal junction position moves toward the bottom of the wire, as shown by the green curve in Figure 4.9(a). For the bare nanowire (shown in Figure 4.9(b)),the efficiencies are lower than for the passivated nanowire, and this holds true for any value of the SRH lifetime. We conclude that surface passivation is a robust strategy for increasing efficiency across a range of material qualities.

One possible concern with a bare high-Al content AlGaAs layer is natural oxidation in the atmosphere. If this is a problem, one possible strategy is to reduce the Al content near the outer surface. Adding a thin GaAs outer layer is also an option [86]. The final device may also employ a polymer infill between the nanowires [91], which may inhibit nanowire oxidation.

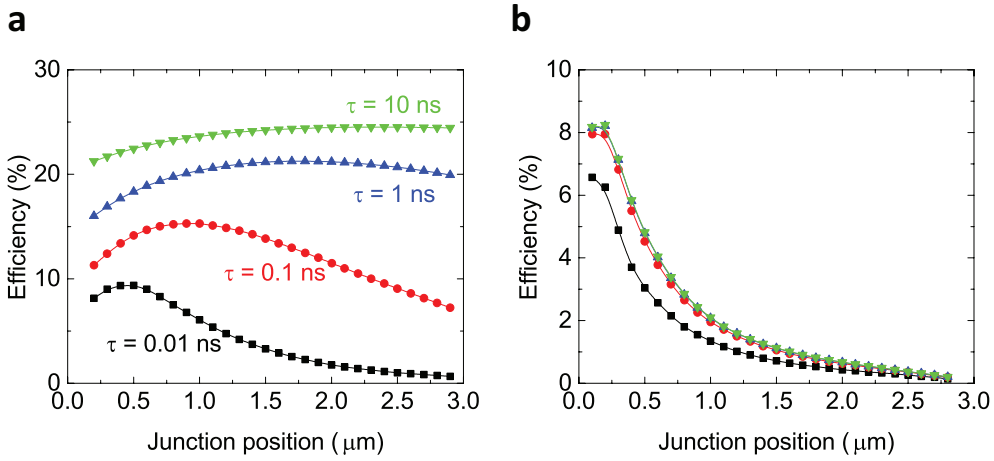

Figure 4.9: Efficiencies of (a) the passivated nanowire solar cells and (b) the bare nanowire solar cells with different bulk SRH lifetimes as functions of the junction depth.

4.7 Summary

In this chapter, we have designed a passivation scheme for axial junction nanowire-array solar cells. We used coupled optical and electrical transport simulations to validate our approach. We found that the absorption properties of the GaAs nanowire array with an AlGaAs passivation layer do not deviate much from the optimal bare GaAs nanowire design, due to the high bandgap energy of AlGaAs. Our design exhibits a 21.26% power conversion efficiency for the nanowire array with nonideal surface conditions, which is 2.7 times higher than the optimal bare nanowire design with the same surface conditions. The efficiency enhancement comes from the better protection of the generated minority carriers as well as the longer minority carrier diffusion length achieved by the modulation doping. The design also has great tolerance to the active layer doping concentration, surface conditions, and junction depth.

In this study, we designed a passivation layer specifically on a single-junction GaAs nanowire solar cell. The same concept can be applied to a nanowire multijunction tandem solar cell, with reoptimization for desirable band alignment by adjusting the shell's composition and doping. Furthermore, since this design can greatly enhance effective minority carrier lifetime and conductivity, it can also be used in other nanowire applications such as photodetectors, light-emitting diodes, field effect transistors, and tunneling diodes.

Chapter 5

Conclusion and outlook

5.1 Conclusion

The main contribution of the first part of this dissertation can be listed as following. Firstly, I used accurate electromagnetic simulations to carry out a systematic study of the optical absorption properties of vertically-aligned semiconductor nanowire arrays for photovoltaic applications. In general, I demonstrated that optimized nanowire arrays in six different materials and for a range of heights from 100 nm to 100 μm all outperform unpatterned thin films of equal height. More specifically, I found that the absorption properties depend strongly on the structural parameters of the nanowire arrays (wire diameter d, spacing between wires a and wire height h). For a certain semiconductor material, the absorption saturates to unity by a certain height of the nanowire array with the optimized diameter and spacing. Such saturation height is as short as 3 μm for the four direct band gap materials considered. This result is important for minimizing the material usage as well as the cost and time of the process. It is also important for the electrical solar cell device design when the efficiency is limited by the diffusion length of the minority carriers.

Secondly, I designed a III-V-nanowire-array-on-silicon double junction solar cell. I addressed the importance of the current matching in such design and optimize the structure to achieve such matching condition. For all four III-V materials considered, a larger than 30% detailed-balance efficiency can be achieved by using

1 μm-tall nanowire arrays with optimized lattice constants and diameters. This approach leverages previous development of highly optimized, single-junction, crystalline silicon solar cells, used here as the bottom cell. The efficiency of the silicon cell can be boosted above 30% by a very thin film ($\sim$ 1 μm) lattice-mismatched III-V nanowire array, which is impossible for a planar structure. The design methods I use in this work can also be extended to the designing of multijunction nanowire tandem cells.

Last but not the least, I used coupled optical and electrical transport simulations to design a high performance and robust surface passivation scheme on axial junction GaAs nanowire solar cells. This design exhibits a 21.26% power conversion efficiency for the nanowire array with nonideal surface conditions, which is 2.7 times higher than the optimal bare nanowire design with the same surface conditions. This design solves the common issue of the large surface-to-volume ratio nanowire semiconductor devices. Axial junction geometry is essential for the practical multiple junction nanowire solar cell device. The small junction area can potentially achieve high open circuit voltage for a photovoltaic cell and high speed for the nanowire photodetector.

5.2 Outlook

The theoretical work indicates a bright future for nanowire array photovoltaics, and recent experimental achievements also confirm that. Our collaborators at USC (Dapkus group and Zhou group) have demonstrated a single junction GaAs nanowire array solar cell [91] and a GaAs-on-silicon dual junction solar cell [92], following the designs described in Chapter 2 and Chapter 3. Both works feature high short circuit currents which are close to the theoretical limit. This confirms the

accuracy of the electromagnetic modeling and the excellent absorption properties of nanowire arrays without the need of an anti-reflective layer. Efficiency wise, the energy conversion efficiencies of 7.68% for single-junction cell and 11.4% for dual-junction cell are still far lower than the best existing cells in similar material systems. There is still plenty of room to improve the device performance. The open circuit voltage obtained in the experiments is far below the state-of-art GaAs solar cell. The main reason for the low open circuit voltage might be the large surface recombination velocity. This was observed in the electrical simulation result shown in Figure 4.7. I expect that the application of the surface passivation scheme discussed in Chapter 4 will greatly enhance the open circuit voltage.

In the simulation part, although we are confident enough about the accuracy of the electromagnetic simulation, it is always challenging to accurately decide the material parameters used in electrical simulations, such as mobilities, minority carrier lifetimes, doping concentrations and surface recombination velocities. While great effort has been put into experimentally characterize the values of the electrical transport parameters, a design which is robust for a wide range of the parameter is also desirable. In Chapter 4, I gave an example of such design, whose performance depends only weakly on the surface quality.

Part II

Optical Epitaxial Growth

Chapter 6

Introduction

6.1 Building photonic matter from the bottom up

Optical fields induce mechanical forces on matter, capable of pulling objects into precise positions [93, 94, 95]. Single-particle optical traps based on this principle have been demonstrated for biological cells [94, 96, 97, 98], dielectric particles [99, 100] and metal particles [101, 102, 103] and have widespread application in physics and biology. For small particles, the optical force on a particle is proportional to the gradient of the light intensity. Arrays of optical traps can be created by varying the optical field intensity in space, creating a periodic optical potential (Figure 6.2(a)). Holographic optical traps [104], interference optical lattices [105, 106], micro-optics arrays [107] and microphotonic near-field approaches [108, 109, 110] have all been used to trap arrays of objects. These techniques suggest the exciting possibility of on-demand assembly of photonic matter "from the bottom up." Nano- and micro-scale constituents such as dielectric particles [104], particle-molecule complexes [109], biological cells [107, 111], and microlenses [112] have been assembled into arrays to achieve various functionalities. Although initial attempts have been made to assemble metal particles [113, 114], optical trapping of a 2D periodic array has not been achieved. Periodic metallic nanoparticle arrays have unique and tunable optical properties with applications in Raman amplification [115], sensing [116]

and lasing [117], and the ability to assemble such structures optically would enable far-reaching dynamic control.

6.2 Optical binding

Metallic particles interact strongly through coherent light scattering, complicating optical trapping techniques. Scattering produces interparticle forces, a phenomenon known as optical binding [105]. Optical binding (Figure 6.1(b)) drives the formation of certain well-defined particle arrangements within an optical trap [105, 118, 119, 120, 121]; for extended, multi-particle patterns, the arrangements are in general aperiodic. To assemble metallic particles in a periodic optical trap array, the optical binding effect between particles in different trapping sites must be considered. In recent experiments, we used a photonic crystal slab to create a 2D periodic trap array [108, 122] (Figure 6.1(c)). While polystrene nanoparticles trap at every site in the array [108], gold nanoparticles trap in one-dimensional chains [113]. This difference can be attributed to stronger optical binding in the metallic nanoparticle system, which competes with trapping forces to prevent the filling of every trap site. However, because previous work on optical binding has not studied binding effects within multiple traps, no general theory is available to explain or predict the observed behavior.

6.3 Optics matter and optical epitaxial growth

Many of the breakthroughs in modern technology have resulted from the successful development of semiconductor materials and the control of their electrical properties. Due to the natural proclivity, the atoms in a semiconductor organize themselves into periodic structures. Figure 6.2(a) shows a unit cell of gallium

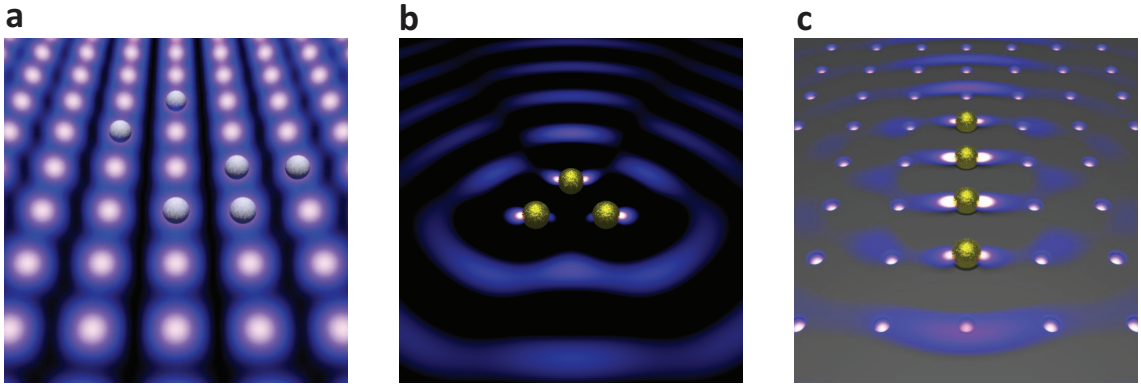

Figure 6.1: Pattern formation due to optical trapping and optical binding. (a) A periodic optical potential traps weakly interacting particles at intensity maxima, due to the optical gradient force. (b) Optical binding causes strongly interacting particles to arrange themselves into well-defined patterns, even in a nearly uniform light field. (c) Competition between a periodic optical potential and optical binding can give rise to pattern formation, preventing particles from trapping at every site. Here, particles form 1-D chains.

arsenide crystal. This unit cell repeats periodically in space. Periodic arrangement of atoms presents a periodic potential to electrons propagating through it and creates energy bands shown in Figure 6.2(b). Modern advanced epitaxy growth techniques such as molecular beam epitaxy (MBE) enable us to place these atoms into precise positions layer by layer (Figure 6.2(c)).

Photonic crystals are artificial optical analogues of semiconductor material used to precisely control the optical properties of materials [123, 124]. In a photonic crystal, shown in Figure 6.2(d), materials with different dielectric constants are placed into periodic structures on the length scale of the wavelength. Similar to electron band gaps in semiconductor materials, photonic crystals have photonic band gaps (Figure 6.2(e)), which prevent light from propagating in certain directions with specified frequencies (i.e., color of light).

Here we suggest that the analogy between natural crystalline materials and photonic crystals can be extended to the growth mechanism. In traditional epitaxial growth of "electronic matter", the growth substrate provides a 2D periodic potential landscape and atoms are essentially organized and held together by the exchange of electrons with both the growth substrate and the atoms on the same growth layer. Similarly, "optical matter" could be organized and held together by photons. A periodic array of optical traps serves as the growth substrate, with individual particles able to trap at any site. Particles also interact with one another via optical binding. Both effects determine the final arrangement of particles. To grow particular structures of interest, one must determine how to design the substrate so that optical trapping and optical binding forces cooperate, rather than compete.

6.4 Outline of PART II

In this part of the dissertation, I first introduce a Monte Carlo model to study the energetics of growth in Chapter 7. For square lattices, we find that 1D particle chains form perpendicular to the incident light polarization, in agreement with previous experiments [113]. For hexagonal lattices, we predict that a 2D particle array will be formed. Drawing upon this prediction, in Chapter 8, I design and fabricate a photonic crystal template with hexagonal symmetry. Using the template, I demonstrate low power optical trapping of a 2D periodic array of over fifty gold nanoparticles with spacing comparable to the wavelength. Due to optical binding interactions, the stability of the 2D array is much greater than for a single, trapped particle. To our knowledge, this is the first experimental demonstration of a periodic array of gold nanoparticles via optical trapping methods.

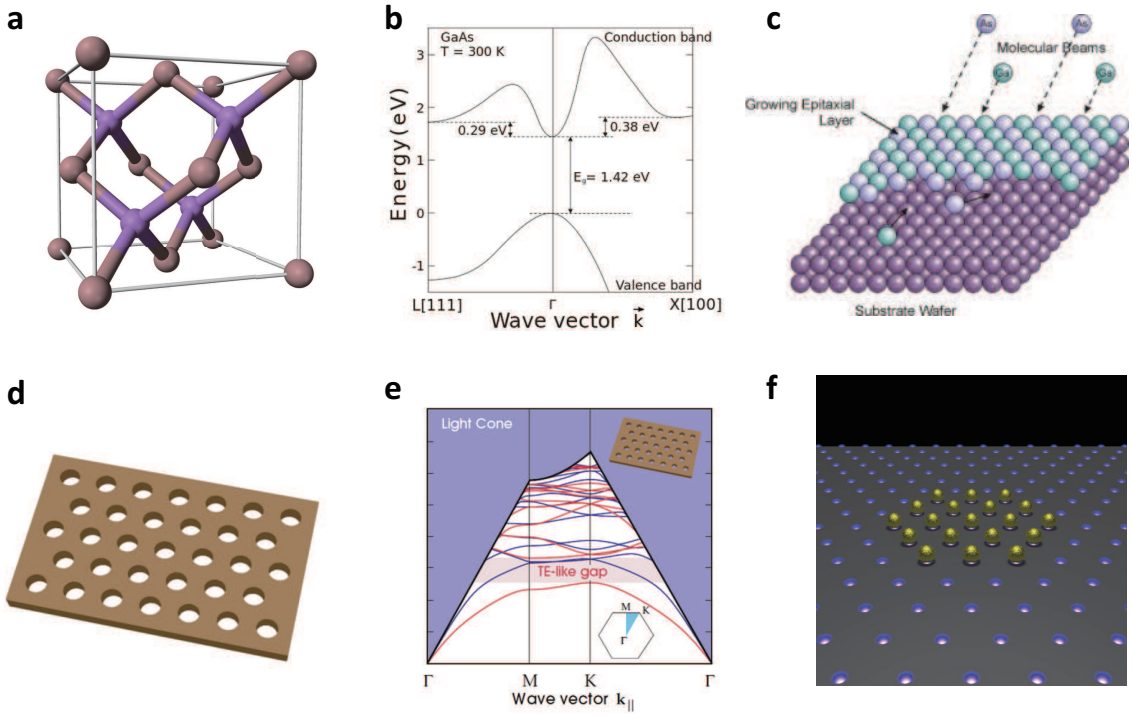

Figure 6.2: Comparisons between "electrical matter" and "optical matter". (a-b) A unit cell of gallium arsenide crystal and electron band diagram of gallium arsenide [2]. (c) Schematic of molecular beam epitaxy. (d-e) A photonic-crystal slab and photonic band diagram of the photonic-crystal slab [3]. (f) Optical epitaxial growth of a single layer of "optical matter".

Chapter 7

Monte Carlo simulation of optical epitaxial growth process

A version of the results in this chapter is contained in Ref.[125].

7.1 Introduction

The optical manipulations of nano-objects are often within two very distinct categories. The first one treats each optical trap individually [93, 94]. The optical force relies on the strong gradient of the optical intensities. One particle can be stably trapped near the strongest light intensity position. Even though many works involve multiple optical traps [104, 105, 106, 107], the interaction between particles trapped at different trapping sites were often neglected. The second category investigates the interaction between multiple particles with a single trap (a.k.a. optical binding), where the gradient force is comparatively weaker than the interaction force between particles [105, 118, 119, 121, 120]. Due to the multiple scattering of light, particles can arrange themselves into well-spaced regular patterns.

As introduced in Chapter 6, in this dissertation work, I am investigating a system involves an array of optical traps and strongly scattering metallic nanoparticles. The gradient force generated by a single optical trap can hold a metallic nanoparticle in place. At the same time, the particles trapped on the different

traps interact with each other by the scattering of the light. Two effects compete with each other and prevent the particle from filling of every trap site. So far, no general theory is available to explain or predict the observed behavior.

Here we suggest that the behavior of strongly interacting particles within a periodic array of optical traps can be viewed as an optical analogue to epitaxial growth. The array serves as the growth substrate, with individual particles able to trap at any site. Particles also interact with one another via optical binding. Both effects determine the final arrangement of particles. To grow particular structures of interest, one must determine how to design the substrate so that optical trapping and optical binding forces cooperate, rather than compete. We introduce a Monte Carlo model to study the energetics of growth. For square lattices, we find that 1D particle chains form perpendicular to the incident light polarization, in agreement with previous experiments. For hexagonal lattices, we predict that a 2D particle array will be formed.

7.2 Interparticle interaction between particles in light field

To model the interparticle interaction between particles in light field, we first study the scattering of the electric field by the single particle. If the particle dimension is small compare to the wavelength of the light, the particle can be modeled as oscillating dipoles.

For a dipole source ($\mathbf{p}$) at position ($\mathbf{r}_\mathrm{A}$), the emitted electric field ($\mathbf{E}$) at arbitrary position ($\mathbf{r}_\mathrm{B}$) can be written as

$$\mathbf{E}(\mathbf{r}) = \mathbf{G}(\mathbf{r}_\mathrm{B}, \mathbf{r}_\mathrm{A})\mathbf{p}(\mathbf{r}_\mathrm{A}) \tag{7.1}$$

where $\mathbf{G}(\mathbf{r}_\mathrm{B}, \mathbf{r}_\mathrm{A})$ is the dyadic Green's function, a tensor. For a dipole in a complicated environment (e.g. on top of a photonic-crystal slab), $\mathbf{G}(\mathbf{r}_\mathrm{B}, \mathbf{r}_\mathrm{A})$ can be solved numerically using the finite-difference time-domain (FDTD) method. A dipole source is placed at a given position $\mathbf{r}_\mathrm{A}$ with fixed polarization, and the field produced is monitored throughout the structure. At each position $\mathbf{r}_\mathrm{B}$, the three columns of the tensor $\mathbf{G}$ correspond to the fields due to an x-, y-, z-polarized source, respectively. The full function $\mathbf{G}$ can be mapped out by repeating the FDTD calculation for each source location $\mathbf{r}_\mathrm{A}$. The calculation time can generally be reduced by using any symmetries of the structure (e.g. mirror, translational) to reduce the total number of source locations required.

Figure 7.1 shows the detailed simulation geometry to obtain the Green's functions. I consider a silicon slab with 250 nm thickness. If we consider the translational symmetry in x- and y-directions and only at a certain height, the Green's function can be reduced to a two-dimensional tensor which only depends on the in-plane displacement ($\mathbf{G}(\mathbf{r}_\parallel) = \mathbf{G}(x, y)$). Two different simulations are performed to get all nine components in Green's function ($G_{xx}(x, y)$, $G_{xy}(x, y)$, $G_{xz}(x, y)$ etc.). In the first simulation, shown in Figure 7.1(a), the dipole (red arrow) is positioned along x direction and 125 nm above the slab. We perform FDTD simulation and monitor the vectorial electrical field $E_x(x, y)$, $E_y(x, y)$ and $E_z(x, y)$ at the same plane as the dipole, shown as a yellow plane. The first column components in the Green's function correspond to the field:

$$G_{xx}(x, y) = E_x(x, y) \tag{7.2}$$

$$G_{xy}(x, y) = E_y(x, y) \tag{7.3}$$

$$G_{xz}(x, y) = E_z(x, y) \tag{7.4}$$

By using rotational symmetry, the result can be converted to the second column in the Green's function. Another simulation with the dipole polarized along z direction is performed for the third column in the Green's function (G_{zx},G_{zy} and G_{zz}). The simulation mesh can be further reduced by considering the mirror symmetry of the field and the geometry. As shown in Figure 7.1, in the first simulation, symmetric and anti-symmetric symmetries have been applied along y- and x-axis to reduce the simulation mesh to one quarter. Similarly, symmetric boundary condition can be used in both x- and y-direction in the z-polarized dipole case.

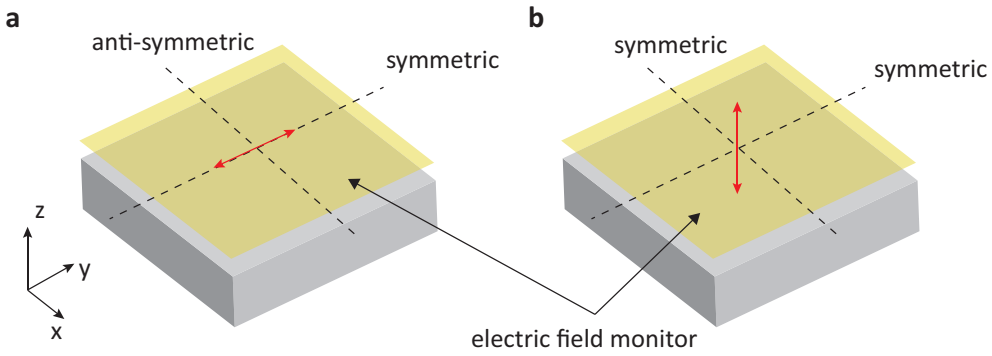

Figure 7.1: Simulation setup for Green's functions (a) simulation of the first and second columns in Green's function tensor. (b) simulation of the third column in Green's function tensor.

Once we obtain the scattered field from a particle, to investigate the inter-particle interaction, we need to investigate the mechanical effect (optical force) of the scattered field to other particles. In the dipole approximation, the time-averaged total force on a sphere in a time-harmonic electromagnetic field $\mathbf{E}(\mathbf{r},t) = \Re\left[\mathbf{E}_0 \exp(-i\omega t)\right]$ can be expressed as

$$\left\langle F^{\mathrm{i}} \right\rangle = \frac{1}{2}\Re\left[\alpha E_{0\mathrm{j}} \partial^i (E_0^{\mathrm{j}})^*\right], \tag{7.5}$$

where i and j are each one of the Cartesian components. For a complex polarizability $\alpha = \alpha' + i\alpha''$, the time-averaged force can be written as

$$\langle \mathbf{F} \rangle = \frac{1}{4}\alpha' \nabla E^2 + \frac{1}{2}\alpha'' E^2 \nabla \phi, \tag{7.6}$$

where ϕ is the position dependent phase of the electric field. The first term depends on the spatial variation of the intensity and is known as the gradient force. The second term depends on the spatial variation in the phase and is known as the dissipative or absorption force. For the particles considered in this work, the imaginary part of the polarizability is two orders of magnitude smaller than the real part, and so we will neglect the second term.

From the first term, we can define a potential energy

$$U = -\frac{1}{4}\alpha' E^2. \tag{7.7}$$

Suppose one particle (A) is sitting at position $\mathbf{r}_\mathrm{A}$ and another particle (B) at position $\mathbf{r}_\mathrm{B}$, denote the initial electric field at these two positions by $\mathbf{E}_\mathrm{A}$ and $\mathbf{E}_\mathrm{B}$, respectively. The scattered field from particle A at position B is

$$\begin{aligned} \Delta\mathbf{E} &= \mathbf{G}(\mathbf{r}_\mathrm{B}, \mathbf{r}_\mathrm{A})\alpha_\mathrm{B}\mathbf{E}_\mathrm{A} && (7.8) \\ &= \mathbf{G}(x, y)\alpha_\mathrm{A}\mathbf{E}_\mathrm{A}, && (7.9) \end{aligned}$$

where (x, y) is the displacement from particle B from particle A ($\mathbf{r}_\parallel = \mathbf{r}_\mathrm{B} - \mathbf{r}_\mathrm{A}$). If we only consider the first scattering process, the total field at position B is

$$\mathbf{E} = \mathbf{E}_\mathrm{A} + \Delta\mathbf{E} \tag{7.10}$$

and the potential energy for the two particle system is

$$U = -\frac{1}{4}\alpha'_{\mathrm{B}}\left(E_{\mathrm{B}}^2 + 2\Re(\mathbf{E}_{\mathrm{B}}^*\Delta\mathbf{E}) + \Delta E^2\right). \tag{7.11}$$

7.3 Induced energy shift in optical epitaxial growth

The equations derived in the last section (Equation 7.11) are universally correct as long as the local electric field ($\mathbf{E}_A$ and $\mathbf{E}_B$) at position $\mathbf{r}_A$ and $\mathbf{r}_B$ is carefully characterized and the Green's function $\mathbf{G}(\mathbf{r}_B, \mathbf{r}_A)$ is accurately simulated. In this section, I will discuss how to use the equation to calculate the induced energy shift in the optical epitaxial growth process.

Figure 7.2 shows a schematic of an optical epitaxial growth experiment. We use a 2D photonic-crystal slab as a growth substrate. The figure shows a side view of it. When light with the resonance wavelength is shined onto the photonic-crystal slab, the electric field intensity is greatly enhanced within the holes in the photonic-crystal slab, shown as red hot spots. The enhanced electric field exerts force and drag the particles towards the surface. Particle A and B are stably trapped particles and particle C is flowing around. This figure also shows the main characteristics of the electric field distribution of the guided resonance mode, plotted along two dashed lines. In the z-direction through the center of holes, the electric field peaks at the center of the slab and exponentially decays above and below the slab. The trapping of the particles rely on the tail of the exponentially decaying field at around 100 nm above the slab. When the position is very far from the slab (typically several hundred of nanometers), the electric field is negligible. In the x-direction across the trapped particle plane (125 nm above the slab in

the model), there is still significant field enhancement (typically $|\mathbf{E}|^2/|\mathbf{E_0}|^2 > 50$). The intensity oscillates periodically to create a 2D optical potential landscape (trapping sites). Because of the unique feature of the guided-resonance mode, the local electric field is in-phase at each trapping site. This fact is very important for simplifying the following simulation.

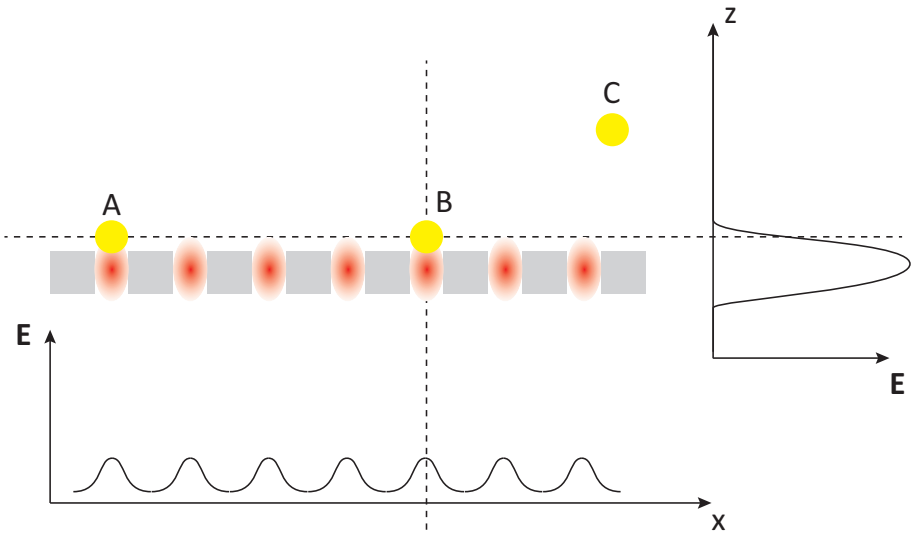

Figure 7.2: Schematic of electric field distribution in a photonic-crystal slab optical epitaxial growth substrate.

In this work, we are mainly interested in the particles which are stably trapped on the photonic-crystal slab (particle A and B). In this case, the local electric field ($\mathbf{E}_\mathrm{A}$ and $\mathbf{E}_\mathrm{B}$) are about the same. The scattered field from dipole A reaching position $\mathbf{r}_\mathrm{B}$ is much smaller than the original field $\mathbf{E}_\mathrm{B}$, by neglecting the second order term ΔE^2, the induced energy shift of the two-particle system due to the scattered field is

$$\Delta U \approx -\frac{1}{2}\alpha'_\mathrm{A}\Re\left(\mathbf{E}^*_\mathrm{A}\mathbf{G}(x,y)\alpha_\mathrm{B}\mathbf{E}_\mathrm{B}\right). \tag{7.12}$$

For the same reason, we can neglect the secondary scattering process and only consider the first scattering (a numerical example can be found in Appendix A).

Figure 7.3 is the graphical illustration of Equation 7.12. The particle A is positioned at origin while the particle B is moved throughout the 2D plane. We approximate the Green's function by that of a uniform dielectric slab (see Appendix A for validation of this approximation). The color at different positions shows the induced energy shift when particle B is positioned at that position. The electric field is polarized along x-direction with the same intensity and phase at the positions of particle A and B. The electromagnetic wavelength used to obtain the Green's function is 1550 nm in vacuum. The dipole is placed 125 nm above a 250 nm thick silicon slab ($n_{\mathrm{Si}} = 3.49$). The silicon slab is on top of a semi-infinite silicon dioxide substrate ($n_{\mathrm{SiO_2}} = 1.55$) and immersed in water ($n_{\mathrm{water}} = 1.318$).

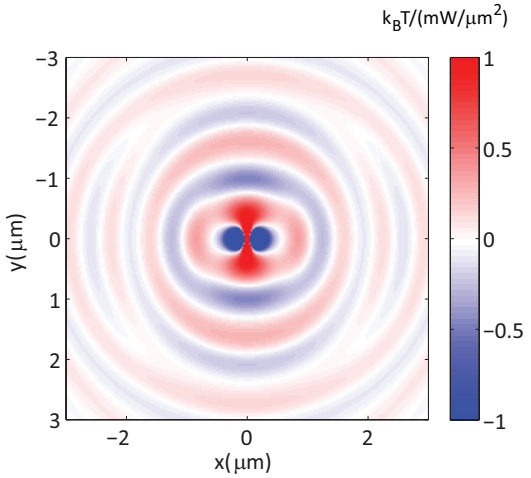

Figure 7.3: Graphical illustration of the energy shift in a two-particle system. (a) The xy-plane cross-section (b) The xz-plane cross-section.

Due to the scattering of the light, the energy shift of two-particle system can either be a positive value (less stable) or a negative value (more stable), depending on the relative position of the two particles. Figure 7.4 shows two cross-sections of Figure 7.3 along the x-axis (black curve) and y-axis (red curve). The interaction energy shift is non-monotonic and oscillates around zero. The interaction is long-range with a decaying envelope, as can be seen in Figure 7.4(b).

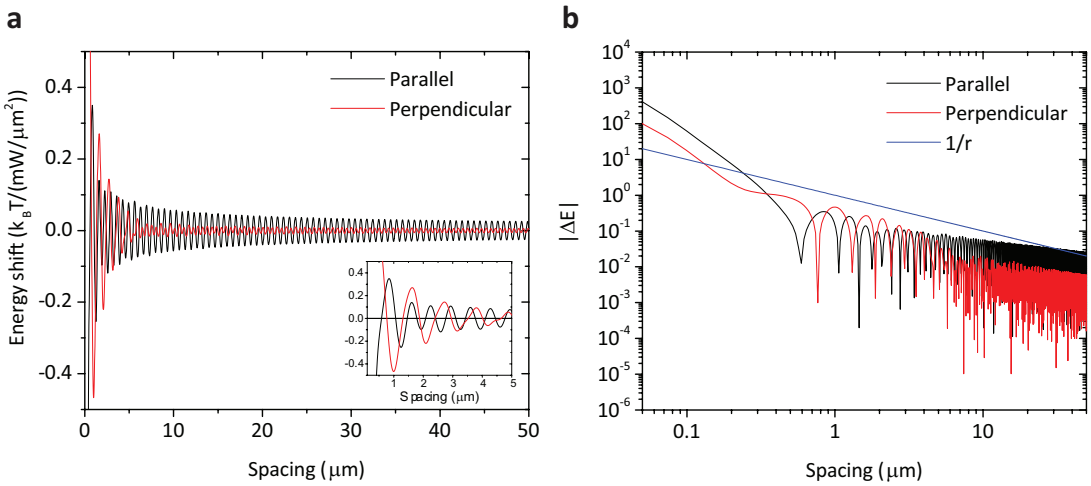

Figure 7.4: Induced energy shift due to interaction. (a) Energy shift as function of spacing between two particles for the polarization parallel to the particle pair (black) and perpendicular to the particle pair (red). (b) log-log plot of the energy shift magnitude. The function $1/r$ is plotted for reference.

For multiple particle system, because the scattered field is much smaller than the unperturbed field, the interference between the scattered field ($\Delta\mathbf{E}_\mathrm{i}^*\Delta\mathbf{E}_\mathrm{j}$) can also be neglect. The energy shift of particle i induced by all other particles can be written as

$$\Delta U = -\frac{1}{2}\Re(\alpha_\mathrm{i})\sum_{\mathrm{j}\neq\mathrm{i}}\Re\left(\mathbf{E}_\mathrm{i}^*\mathbf{G}(\mathbf{R},k)\alpha_\mathrm{j}\mathbf{E}_\mathrm{j}\right), \tag{7.13}$$

where α_i and α_j are the polarizabilities of particle i and particle j, and are the unperturbed local electric fields at particle i and particle j, $\mathbf{R}$ is the vector from particle i to particle j, k is the wave vector, and $\mathbf{G}(\mathbf{R},k)$ is the dyadic Green's function.

7.4 Monte Carlo simulation of optical epitaxial growth

The process of optical epitaxial growth can be described as following. The photonic-crystal slab creates a 2D array of viable trapping sites. When a single particle is considered, the particle can be trapped equally at each trapping site. The probability for this trapped particle to release from the trap depends on the energy created by the photonic-crystal slab ($P \propto \exp(U/k_B T)$), where U depends on the local electric field intensity and the polarizability of the particle (Equation 7.7). When multiple particles are trapped on the photonic-crystal slab, because of the scattering of the light, the energy barrier for a certain particle to release can shift either higher or lower, depending on the relative position of all the other particles. Because the less stable particles (with higher energy) are more likely to release from the surface or hop to the nearest trapping sites, the trapped particle will evolve to a more stable configuration with lower energy.

We use the Monte Carlo method to simulate this process and identify low-energy configurations. The Monte Carlo method only considers the local equilibrium state: in this case, trapped particles on a periodic lattice, and the transition between different states: hopping or release of the particles. We begin by randomly placing the particles at trapping sites. The energy shift for the particle ensemble ($\Delta E = \sum_{\mathrm{i}} \Delta U_{\mathrm{i}}$) is calculated from Equation 7.13. One particle is then selected at random. The particle is either moved to one of the nearest neighbor sites or released from the surface, with each possible option having equal probability. If a particle is released from the surface or hops outside of the device region, it is relocated at a random empty site. If the total energy of the new configuration ΔE_{new} is lower than the old one ΔE_{old} , the new configuration will be unconditionally

accepted. Otherwise, the new configuration will be accepted with the probability $\exp\left(-(\Delta E_{\text{new}} - \Delta E_{\text{old}})\right)/k_B T)$, where k_B is the Boltzmann constant and T is the temperature.

The simulation parameters are chosen to be closest to our typical experiments. The simulations used a 50 μm diameter area lattice with fixed 5% site coverage. The unperturbed field values were set assuming horizontal polarization, constant phase at all trapping sites, and overall amplitude given by a two-dimensional Gaussian envelope ($I = I_0 \exp(-\frac{x^2+y^2}{w_0^2})$), with the beam waist w_0 set to be 15 μm. The total incident power is assumed to be 15 mW, similar to experiment. The electric field intensity on each trapped site is assumed to be 50$\times$ higher than the incident plane wave, based on electromagnetic simulations (see Figure 8.1). Each simulation is run for 5 million steps.

Figure 7.5 shows the result of a typical simulation. It is a square lattice with the lattice constant of 0.93λ. An initial transient is observed in the energy shift, corresponding to loss of memory of the random initial configuration (shadowed area in Figure 7.5(a)). The energy then fluctuates around an equilibrium value. The statistics of energy shift (mean value and standard deviation) is calculated over the last 4.5 million steps. Figure 7.5 (b) shows the histogram of the energy shift over the last 4.5 million steps. Figure 7.5 (c) and (d) shows the configuration as well as the energy shift for individual particles at step 1000 and at the last step, respectively. Initially, the particles are at random positions and the energy shift is close to zero. At the end of the simulation, the particles arrange themselves into well-organized pattern with much lower energy, indicated as dark red.

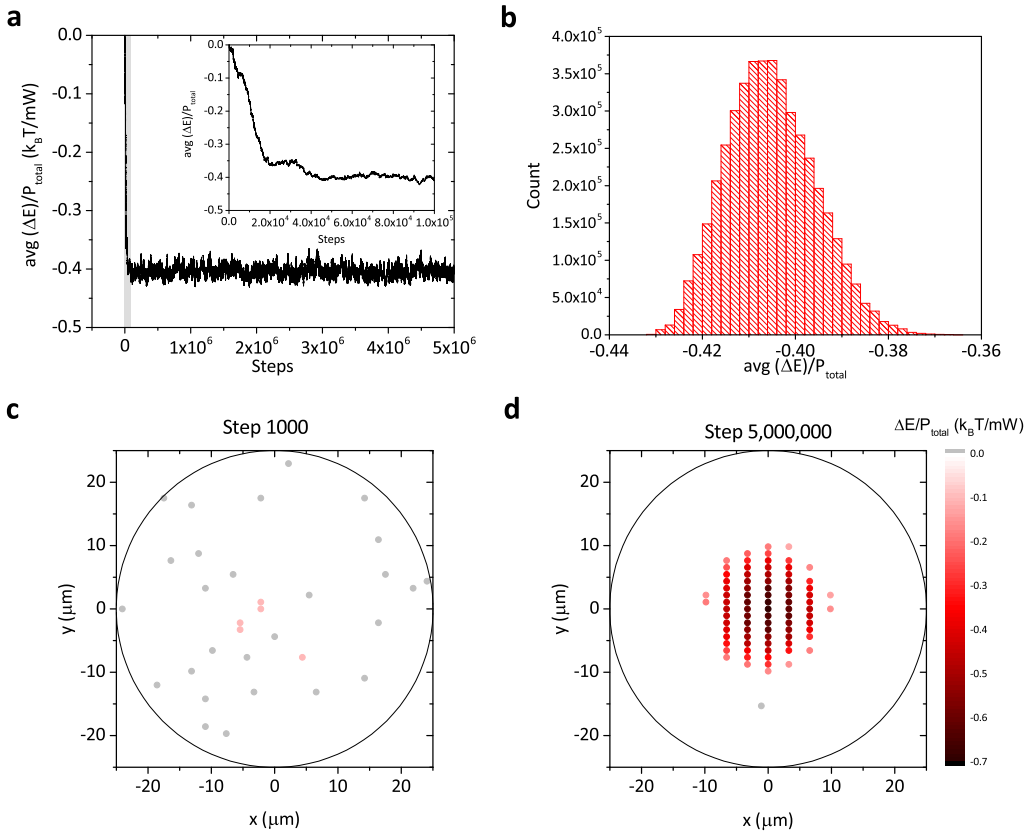

Figure 7.5: A typical Monte Carlo simulation. (a) Average energy shift normalized to the incident power as a function of simulation step. The inset shows the first 100,000 steps (shadowed area in the main figure). (b) The histogram of the normalized average energy shift over the last 4.5 million steps. (c-d) The configurations at step 1000 and step 5,000,000 step, respectively. The color map shows the normalized energy shift for individual particles.

7.5 Monte Carlo simulation result

Two lattice symmetries are considered in this study. They are the square lattice and hexagonal lattice, which are shown in Figure 7.6(a) and (b), respectively. The average energy shift per particle is plotted in Figure 7.6(c) as a function of lattice constant, for both the square and hexagonal arrays. The energy strongly depends on the lattice constant. Several local minima (marked with arrows) can be seen.

For the hexagonal lattice, there is a pronounced dip when the lattice constant is similar to the wavelength ($a/\lambda \sim 1$).

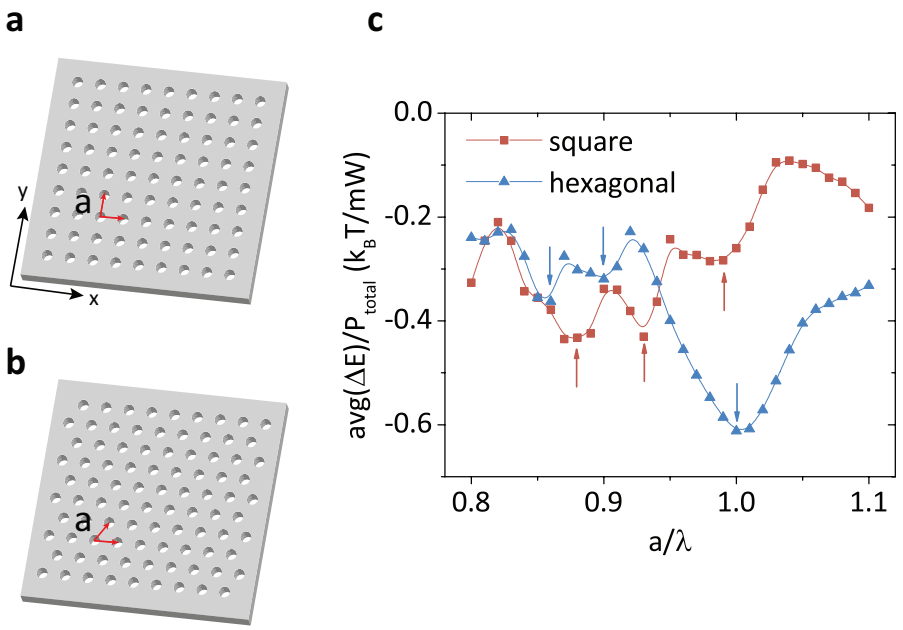

Figure 7.6: Strong interaction-induced pattern formation during optical epitaxial growth. (a-b) Square and hexagonal lattices, each with lattice constant a. (c) Monte-Carlo simulation results of energy shift per particle as a function of lattice constant. The solid lines are guides to the eye. Energy is plotted in arbitrary units.

Particle configurations corresponding to each of the local minima in Figure 7.6(c) are plotted in Figure 7.7(a-f). The configurations change dramatically with lattice type and lattice constant. For the square template (Figure 7.7(a-c)), we observe vertical chains with different spacings. The simulation result agrees well with our previously reported experiments, in which we observed chain formation on a lattice with $a/\lambda \sim 0.94$ [113]. In both simulation and experiments, the chains are oriented perpendicular to the polarization direction. For the hexagonal template, oblique chains are observed at $a/\lambda = 0.80$ and $a/\lambda = 0.90$. However, at the lowest-energy local minimum ($a/\lambda = 1.0$), we observe a close-packed array, or cluster. We have verified that an array is also formed for a wide range of lattice

constants nearby, from ~ 0.94 to ~ 1.1. The results suggest that for appropriate choice of lattice type and lattice constant, interparticle interactions act to stabilize the array, which is the lowest energy particle configuration of any shown in Figure 7.6(c).

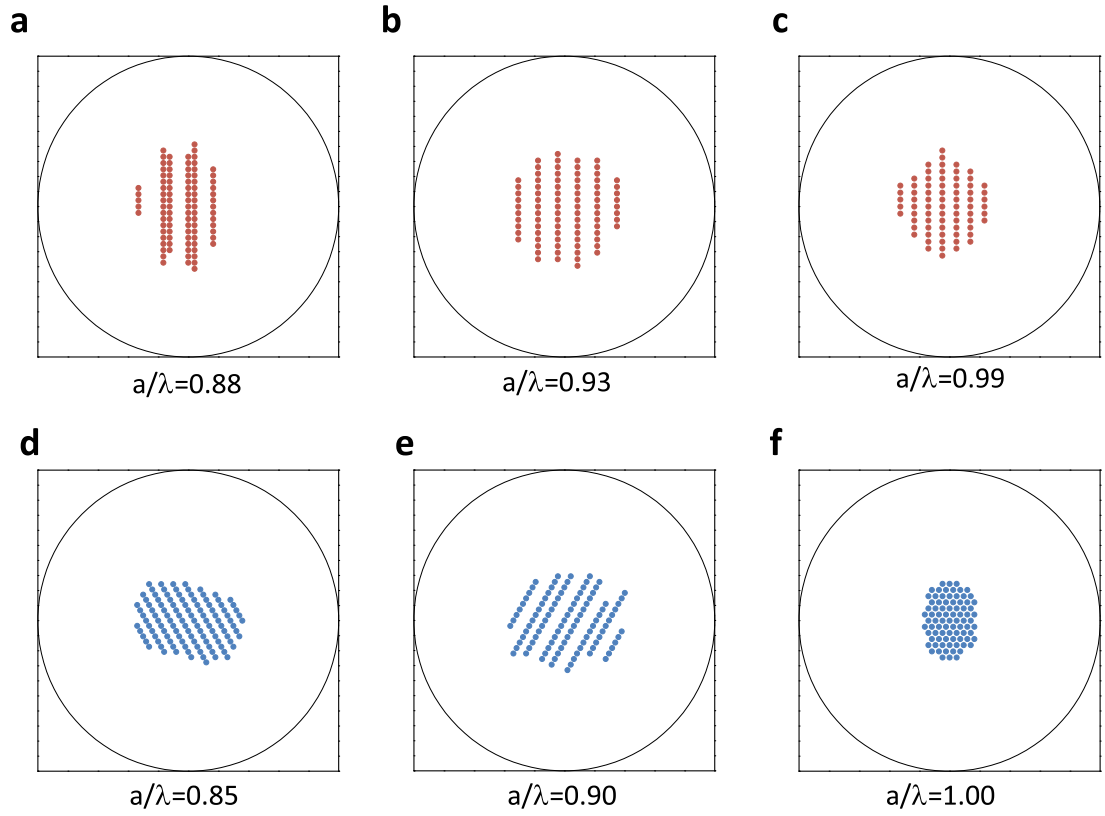

Figure 7.7: (a-c) Particle configurations obtained for square lattices with varying lattice constants. (d-f) Particle configurations obtained for hexagonal lattices with varying lattice constants. The circles show a 50 μm diameter device area.

7.6 Discussions

7.6.1 Effect of the growth substrate

It is worth noticing here that the simulation result shown before is only true for a certain wavelength of light (1550 nm in vacuum and 1176 nm in water) and a certain configuration (250 nm silicon-on-insulator wafer immersed in water). This is the configuration in our experimental work. The result is in general not valid for another configuration at another wavelength, and new simulation of the Green's function (Figure 7.4) is required. I illustrate this point in Figure 7.8. Here I show the energy shift of a two-particle system in different environments. Figure 7.8 (a) shows the energy shift in free space in water, while Figure 7.8(b) and (c) show the energy shifts of two particles which are 125 nm above a 250 nm and 340 nm SOI wafer, respectively. Figure 7.8(b) is the reproduction of Figure 7.4. The energy shift in all three cases oscillates around zeros throughout the 2D space. However, the oscillating behaviors are essentially different for the three cases shown. For clear illustration, a square dot array with the lattice constant of 1.1 μm are shown on top of each graphs. The oscillation along y-axis in case b is slightly faster than the one in case a, while the oscillation is x-axis is much faster (about two times). The thickness of the silicon layer also affects the energy shift. In Figure 7.8(b), when the particle is placed at $(0, 1.1)\mu$m, the energy shift is negative, indicating a more stable configuration. However, if a particle is placed at the same position above a 340 nm SOI (shown in Figure 7.8(c)), the energy shift is positive, which means a less stable structure.

This phenomenon enables a large design space of the optical epitaxial growth substrate, where we can not only design a symmetry and lattice constant, but also engineer the interaction (Green's function) between the particles. In this and

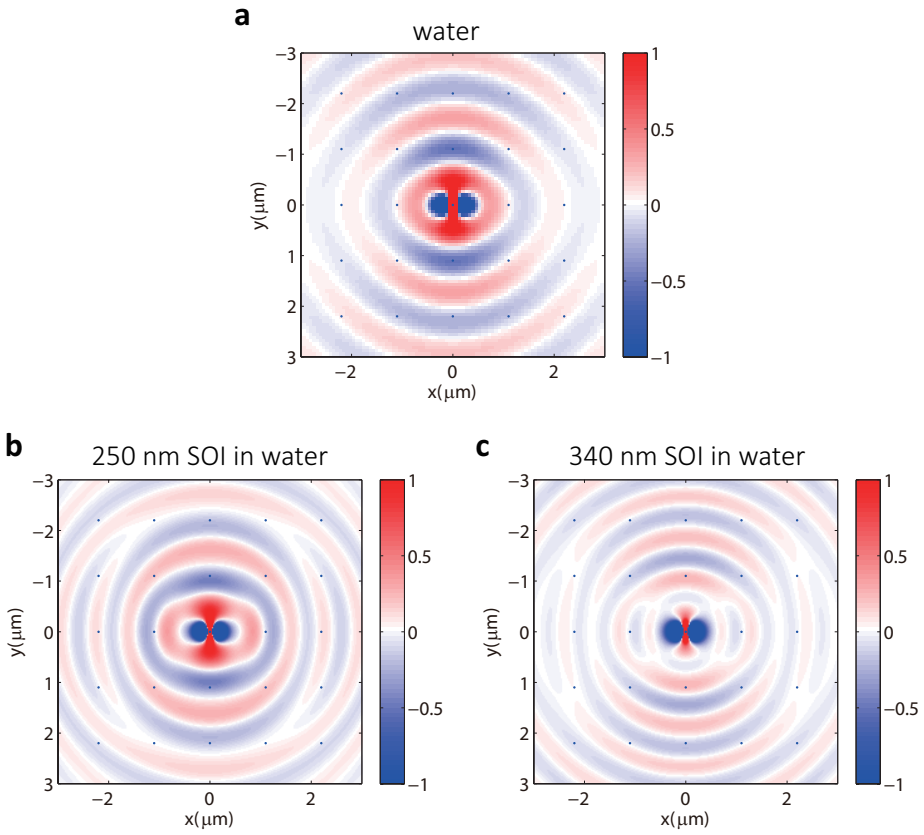

Figure 7.8: Energy shift in a two-particle system in different environments. (a) water. (b) 125 nm above the surface of a 250 nm thick SOI slab. (c) 125 nm above the surface of a 340 nm thick SOI slab.

the next chapters, I focus on design and growth on a 250 nm SOI platform. The result shows that chains can be formed on a square lattice where clusters can be formed on a hexagonal lattice. By using other thicknesses of the silicon layer, we might get a completely different result. When the optical trapping lattices are generated by free space optics such as a holographic optical tweezers array, it is also possible to engineer the particle-particle interactions. Different materials and different thicknesses of the substrate can be used.

7.6.2 Phase transition

Figure 7.9 shows the mean value and standard deviation of the average energy shift per particle as a function of the incident power. The energy shift is normalized by the incident power and has units of k_BTmW. A sharp transition can be observed on the mean value curve (black) when the power is around 10 mW. The average energy per particle is close to zero when the incident power is below 7 mW, and the energy shift per particle saturates to around -0.43 k_BTmW for power larger than 20 mW. These are the two distinct phases for the grown crystalline optical matter. At the low power end, the particle positions are random, similar to those shown in Figure 7.5(c). The system stays in this amorphous phase without forming any particular pattern. When the power increases to a certain value (around 7 mW), the interaction between particles start to bring particles together to form a chains of three or four particles. Occasionally, the chains can grow quite long. However, the interaction is still not strong enough to overcome thermal fluctuations. The system switches back and forth between the random amorphous phase and the well-patterned crystalline phase and cause the standard deviation of the energy shift to peak at this energy. When the power is large enough, the particles form a pattern with the lowest possible energy with only slight fluctuations around this state. Such phase transition behavior further supports the analogy between optical eptaxial growth and crystal growth in general. High incident power here can be seen as the low "growth temperature". This analogy suggests various strategies for improving the quality of the photonic material. Optimization of the "growth temperature" (laser intensity) and growth rate (particle delivery rate), along with the use of annealing, may increase the size and quality of the particle array.

In Figure 7.10 we plot two dimensional maps of the mean values and standard deviations as functions of power and lattice constant for both the square lattice and

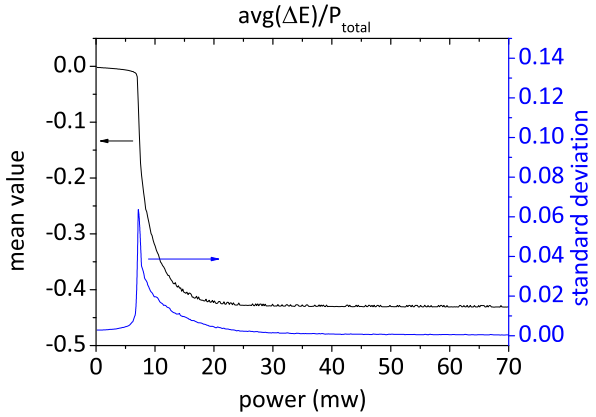

Figure 7.9: Mean value and standard deviation of the average energy shift per particle as a function of the incident power. The simulation is on a square lattice with $a = 0.93\lambda$ and a coverage of 5%.

hexagonal lattice. Cross-sections indicated by the white-dashed lines are plotted as the two curves in Figure 7.6(c). In general, the deeper the energy shift, the lower the power required for the phase transition. For all the local minima discussed in Figure 7.7, the system has already transited to a well-defined crystalline state with 30 mW power.

7.7 Summary

In summary, we have studied a system in which strong optical binding interactions between particles drive pattern formation within a periodic optical trapping potential. Monte Carlo simulations predict that patterns such as 1-D chains and 2-D arrays may be formed, depending on the lattice constant and lattice symmetry.

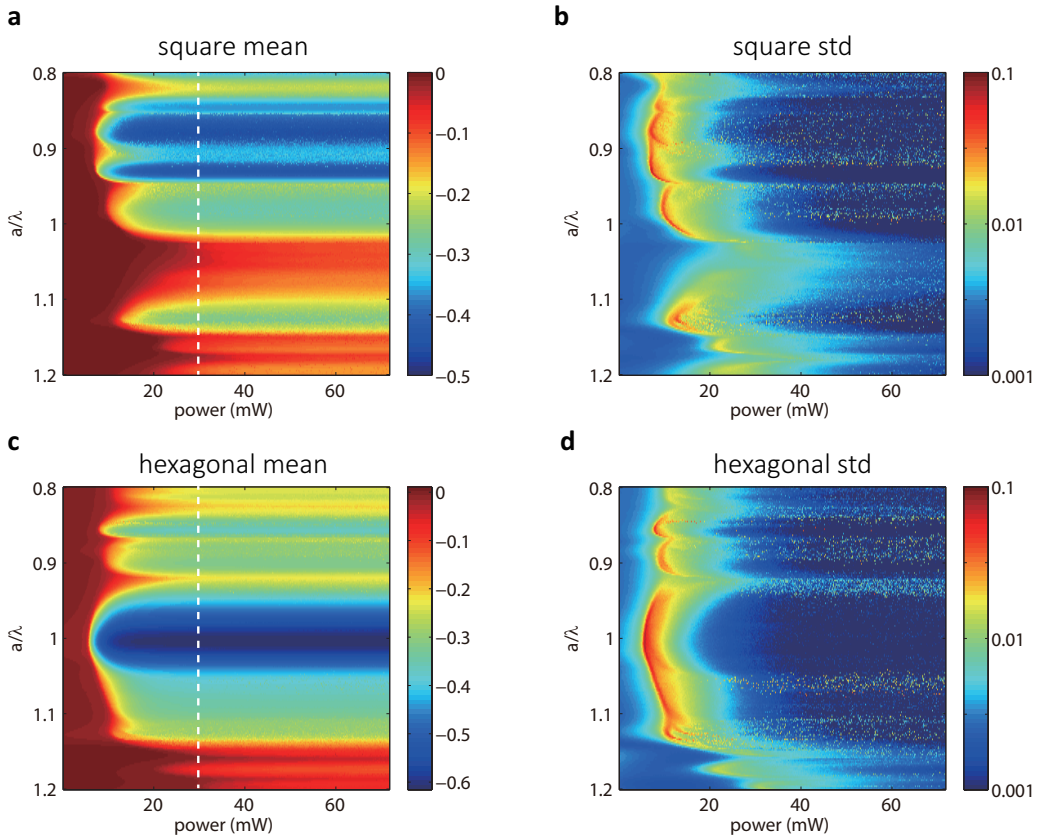

Figure 7.10: Mean values (a,c) and standard deviations (b,d) of the average energy shift as functions of power and lattice constant. The upper row shows the result for square lattices and the bottom row shows the result for hexagonal lattices.

Chapter 8

Optical epitaxial growth of a gold nanoparticle array

A version of the results in this chapter is contained in Ref.[125].

8.1 Introduction

The Monte Carlo simulation results in the last chapter indicate the important effect of inter-particle interactions (optical binding) on pattern formation in the optical epitaxial growth process. The simulation nicely explains the previously observed abnormal chain formation behavior in the trapping experiments of gold particles on a square lattice with a certain lattice constant. It also suggests that the particles trapped by a hexagonal symmetry template with a lattice constant close to the wavelength will form a closely packet cluster with lower energy (i.e. higher stability). In this chapter, I will discuss the photonic-crystal template design and the experiments to achieve the trapping of a 2D array of gold nanoparticles.

8.2 Epitaxial growth template design

Following the prediction of the simulation, we designed a photonic crystal slab with hexagonal symmetry and $a/\lambda \sim 1$. We patterned the 250 nm thick silicon device layer on a silicon-on-insulator wafer into a hybrid triangular-graphite lattice [126]. The larger holes form a hexagonal lattice, while the smaller holes form a

graphite lattice. Such design ensures the hole sizes on the photonic crystal are smaller than the size of the gold particles (d = 200 nm) we used in the experiment, which prevents the particles from sinking into the holes completely. This allows better visualization of trapped particles by optical microscopy. This design supports several low-dispersion photonic bands with high quality factors. The fabricated device is shown in Figure 8.1(a). The silicon layer is 250 nm. The spacing between the larger holes (i.e. lattice constant a) is 1.166 μm, and the laser wavelength in vacuum was 1550 nm; adjusting for the refractive index of water, a/λ = 0.99. The diameters of the larger and smaller holes are 0.134 a (156 nm) and 0.094 a (110 nm), respectively.

Figure 8.1(b) shows the measured transmission spectrum through the photonic-crystal slab. The spectrum shows a Fano resonance feature with an asymmetric dip. We fit this spectrum to the Fano formula as shown by the red curve [127]. The resonant wavelength is 1549 nm and the quality factor is 630.

Figure 8.1(c) shows the simulated electric field intensity of the guided-resonance mode shown in Figure 8.1(b). The field is taken on a plane which is 125 nm above the slab. The electric field of the mode is enhanced in the proximity of the holes.

I employed the Maxwell stress-tensor [128] to calculate the optical force acting upon a gold nanoparticle when the particle is in the proximity to the surface of the photonic-crystal slab. Finite-difference time-domain (FDTD) simulation is performed with the periodic boundary condition in x- and y-directions, and perfect matching layer (PML) boundary condition in z-direction in a supercell area of $3a \times 2\sqrt{3}a$, where a is the spacing between two adjacent large holes. Large supercell size minimizes the influence from the periodic boundary conditions.

Figure 8.2(a) and 8.2(b) show the calculated optical force exerted on a 200 nm diameter gold particle placed at different positions, where the bottom of the particle

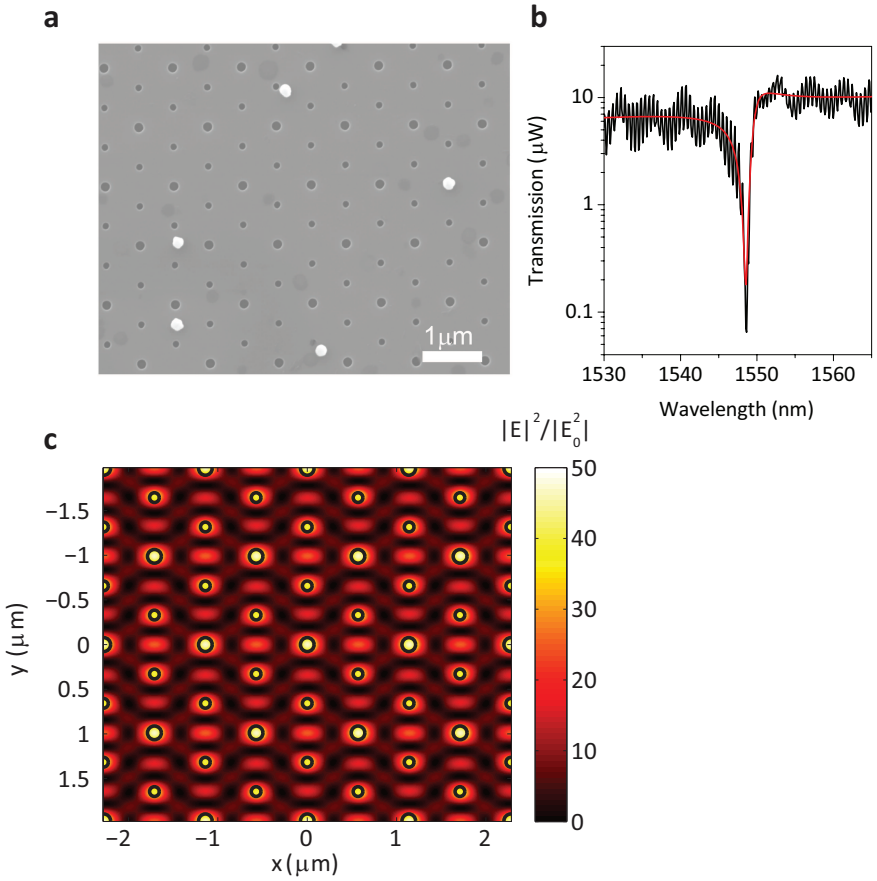

Figure 8.1: Design of the photonic crystal device for experiment. (a) A scanning electron micrograph (SEM) image of the fabricated photonic crystal slab device. The 200 nm diameter gold particles are also shown in this graph. (b) The measured transmission spectrum through the device. (c) The simulated electric field profile ($|\mathbf{E}|^2/|\mathbf{E}_0|^2$) of the guided-resonance mode used in the experiments on a plane 125 nm above the slab.

is 40 nm above the top surface of the photonic-crystal slab. The force is normalized to P/c, where P is the incident power per unit cell and c is the speed of the light in vacuum. The vertical force is strongly attractive in the proximity of the holes. The force at the position of the larger holes is stronger than that near the smaller holes. Strong repulsive forces can also be observed in the space between holes. Within the plane parallel to the photonic crystal slab, the trapping is stable in

the vicinities of the holes in both x- and y-directions. The in-plane forces near the larger holes are stronger than those near the smaller holes.

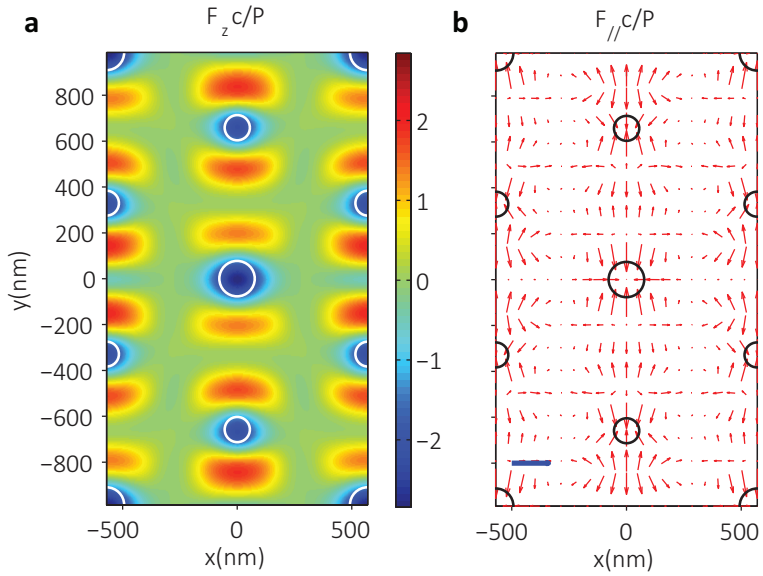

Figure 8.2: Calculated force and potential of the photonic crystal trap. (a) The normalized vertical force exerted on a 200 nm gold particle at different positions along a plane 40 nm above the photonic-crystal slab. Negative force indicates attraction toward the slab. (b) The normalized in-plane force. The blue scale bar indicates $Fc/P = 2$.

8.3 Experimental setup

Figure 8.3 shows the optical setup used for photonic-crystal device characterization and optical epitaxial growth experiments. A single-mode-fiber coupled tunable laser with the tuning range from 1500 nm to 1620 nm is collimated to free-space by an aspherical lens ($f = 11$ mm). Then a polarizer is used to improve the linearity of the polarization and a half-wave plate is used to control the polarization of the incident light beam. Then the linearly polarized light with certain polarization angle is focused by a achromatic doublet lens ($f = 30$ mm) onto the photonic-crystal device which is mounted on a translation stage. The beam spot at the device

position has a 2D Gaussian profile ($I = I_0 \exp[-2(x^2 + y^2)/w_0^2]$) with w_0 measured to be ~ 14 μm. The transmitted light through the photonic-crystal device is collected by another lens or a microscope objective. The collected transmission beam passes another polarization control set (half-wave plate and polarizer) and then be focused by another apherical lens to a fiber coupled photodetector. The transmission spectrum is obtained by swiping the laser wavelength and read the photodetector power accordingly. In the optical epitaxial growth experiment, the laser wavelength is tuned to the resonant wavelength of the photonic-crystal device and operates in a continuous wave (CW) mode. When the high power (P>15 mW) is desired, the laser output is first amplified by an erbium-doped fiber amplifier (EDFA) with the bandwidth from 1530 nm to 1560 nm. The peak power of the EDFA is around 300 mW. A polarization controller is used to gradually control the output power from the EDFA.

Figure 8.3 also shows the illumination and imaging configuration. A multimode-fiber coupled white light source is coupled to free-space and then is refocused onto the device by the microscope objective. The images and videos of the epitaxial growth are captured by a high pixel density CCD camera.

8.4 Optical epitaxial growth experiment

I perform the optical epitaxial growth experiment using the photonic-crystal template designed in Section 8.2. To clearly illustrate the growth process, a low density gold nanoparticle colloidal solution is used. The laser is tuned to 1549 nm, which is the resonant wavelength of the photonic-crystal device. The power is tuned to the minimal trapping threshold power (~ 30 mW), when the particles just start to be trapped. The low power lets the system freely evolve to the global energy

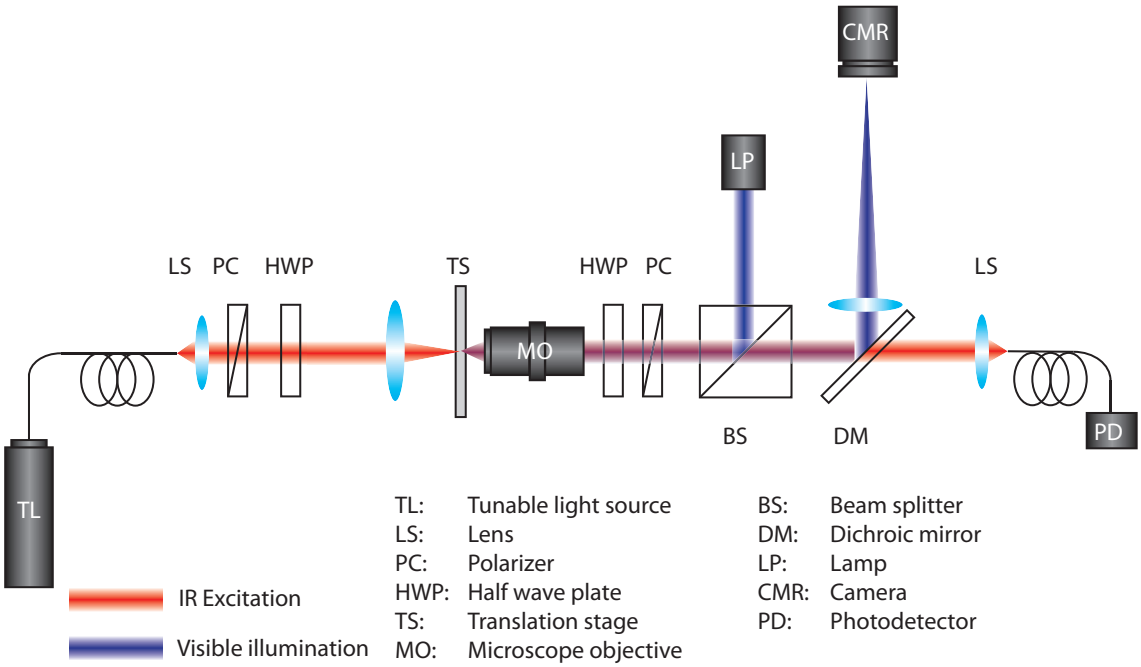

Figure 8.3: Schematic of the optical setup used in optical epitaxial growth experiments.

minimum without getting stuck in local energy minima. A shallow microfluidic chamber with the thickness around 500 nm is used to ensure the two-dimensional environment and minimize the thermal convection out of plane.

Figure 8.4 shows a series of optical microscope images from a typical experiment. The diameter of the gold nanoparticles is 200 nm, and a red arrow indicates incident light polarization. When the laser power was turned on, particles immediately began to trap near the slab (Figures 8.4(a,b)). The trapping sites are not close-packed, and release and re-trapping of particles were frequently observed. As time passed, the trapping area became smaller and the cluster became more filled-in (Figures 8.4(c-f)). Particles also appeared to be trapped more stably. After 40 minutes, a highly stable, close-packed array of nanoparticles was formed. When the laser is turned off, the particles released immediately and diffused back into solution (Figures 8.4(g,h)).

The final array shows evidence of extremely strong optical trapping. Movement of particles within each trapping site was negligible when seen by the naked eye. Analysis of video data for the experiment found that the stiffness of an individual trap was greater than 82.5 pN/nm/W, two orders of magnitude higher than values reported in previous experiments on polystyrene particles [108]. The total power used in the experiment was only 30 mW, for a maximum power of 85 μW per optical trap. The power per trap is orders of magnitude lower than for previously reported metallic nanoparticle traps. In particular, it is around 2,000 times lower than for standard optical tweezers, given similar particle size [101, 102, 103, 119, 120, 129]

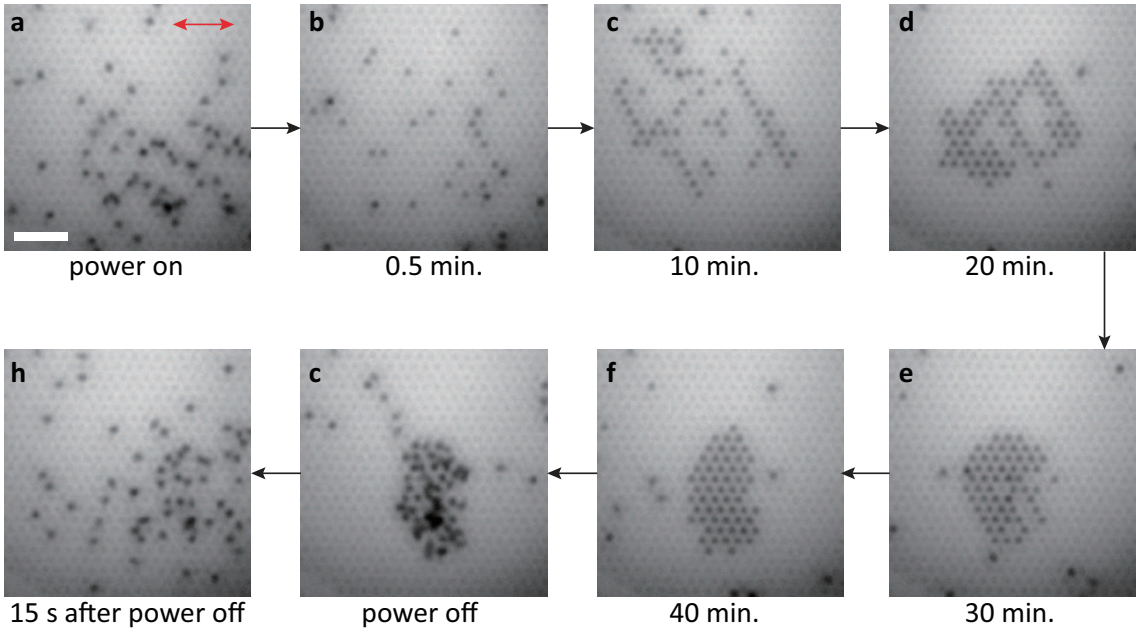

Figure 8.4: Optical epitaxial growth of a gold particle array. Optical microscope images show 200-nm diameter gold nanoparticles trapped on the photonic crystal slab, visible in the background. (a-f) Snapshots taken with the laser power on; elapsed time is shown below image. (g,h) Snapshots taken with laser power off. The scale bar indicates 5 μm.

The formation of the gold nanoparticle array in still solution relies on the Brownian motion of the particles to bring them close enough to the holes to get

trapped, which makes the assembly process slow. Moreover, in a still solution, the particle density drops as the trapping experiment progresses and eventually limits the size of the trapped gold cluster. To solve these issues, we fabricated a microfluidic flow channel to deliver particles. Figures 8.5(a-c) show snapshots during a LATS experiment in a microfluidic channel with flow. At the beginning, the diameter of the trapping region is over 25 μm, which is close to the incident beam size. The flow brings a large amount of gold particles to the center region of the photonic crystal device where the laser beam is focused. The number of trapped particles increases rapidly with time while the cluster becomes more close-packed. In six minutes, more than 120 particles are trapped in a preliminary cluster.

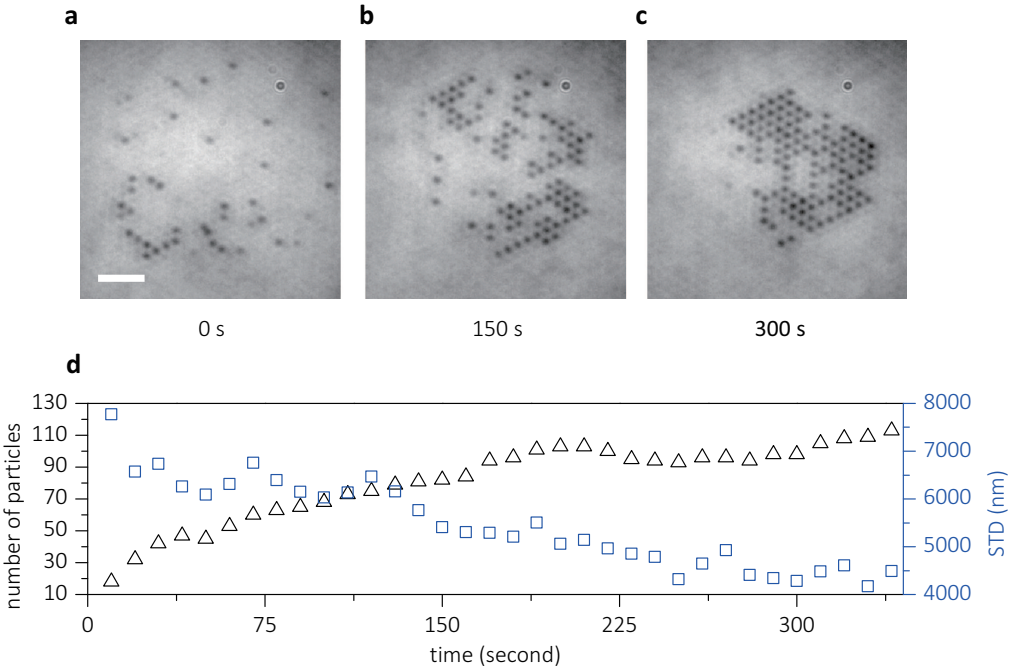

Figure 8.5: Optical epitaxial growth experiments in a microfluidic channel. (a-c) The snapshots when the beam is on for 0 s, 150 s and 300 s. (d) The number of trapped particles (black triangles) and the standard deviation of the particle positions (blue squares) as functions of time. The scale bar indicates 5 μm.

8.5 Discussion and conclusion

In this chapter, we use the prediction of the Monte Carlo simulation shown in the last chapter to successfully demonstrate growth of a periodic, hexagonal array of closely-spaced gold nanoparticles on top of a photonic crystal template. In this system, the optical force of the template on the particle cooperates with the optical binding interaction to produce a pattern that is energetically favorable and highly stable.

We attribute the ultra low threshold trapping and highly stable particle arrays to two facts. The first one is the cooperative interactions between particles, which has been shown in Figure 7.6(c). To further understand the energetics of the growth process, we calculated the energy shift as a function of time. Particle positions were extracted from the video, and the energy shift was calculated from Equation 7.13. Figures 8.6(a-c) show the energy shift for each particle at three different snapshots in the growth process, corresponding to the microscope images in Figures 8.4(d-f). At early times (Figure 8.6(a)), the particles sparsely attached to the substrate over a large area, and the energy was high (light red). Some oblique chains were formed, and the particles at the center of the chains had lower energy. As time passed (Figure 8.6(b)), the trapping area became smaller and the cluster became more filled-in. Meanwhile, the energy was greatly reduced (dark red), especially for particles at the center of the cluster (Figure 8.6(c)). This result correlates with the observation of greater trapping stability as the experiment proceeded. The average energy shift per particle is plotted in Figure 8.6(d), which confirms that the formation of the nanoparticle array was accompanied by minimization of the energy.

The second fact which contributes to the stable particle array is the strong interaction between the particle and photonic-crystal slab growth substrate. In

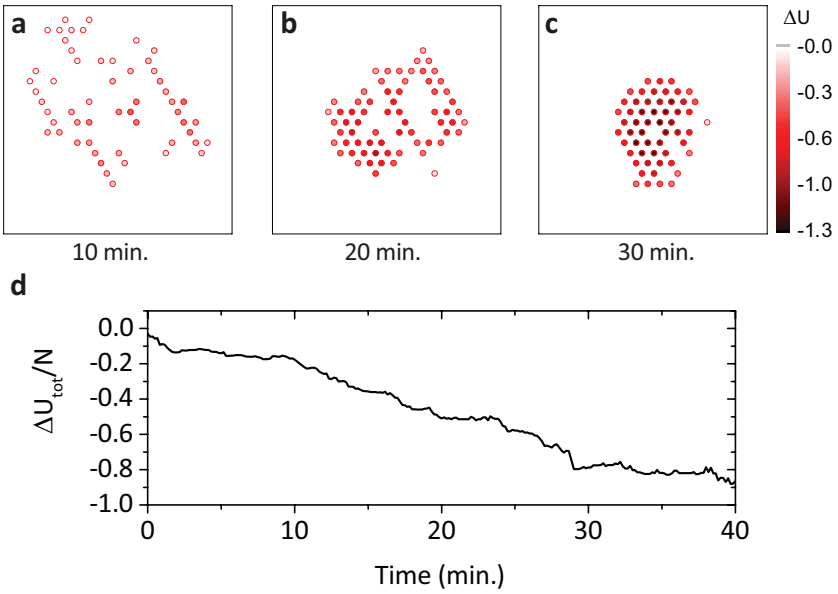

Figure 8.6: Energy lowering during the growth process. (a-c) The energy shift of each particle. (d) Average energy shift per particle as a function of time.

the last chapter's simulation, we only assume that the particles can be stably trapped by the substrate and polarized by the field. Here we perform detailed full-wave electromagnetic simulation to characterize the particle-template interaction. Calculations show that the optical force on a gold particle is much stronger than on a polystyrene particle of equal size. Figure 8.7(a) plots the normalized vertical force for a particle centered above one of the bigger holes in the template. As the gold particle approaches the slab, the electromagnetic field is significantly redistributed (Figures 8.7(b),(d)). This effect is present to a much lesser degree for polystyrene (Figures 8.7(c),(e)), which experiences an order of magnitude weaker optical force. The results suggest that the gold particle does not simply experience a "gradient" force due to the evanescent tail of the resonant mode of the photonic-crystal slab; the strong attraction is a cooperative effect between particle and slab, mediated by

field redistribution. Here, the incident laser wavelength is at 1550 nm, far above the plasmon resonance of the gold particle.

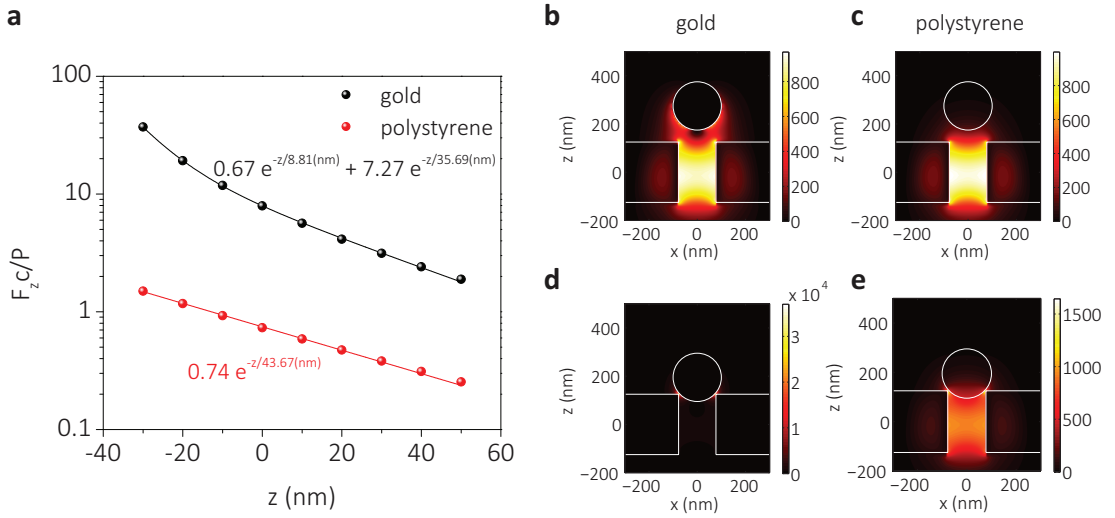

Figure 8.7: Comparison of optical forces on gold and polystyrene nanoparticles. (a) Calculated, normalized vertical force exerted on 200 nm gold and polystyrene particles at different heights. The force is in dimensionless units of Fc/P, where c is the speed of the light and P is the incident optical power within one unit cell. Positive force indicates attraction toward the slab. (b-d) Field intensity profiles for gold (b),(d), and polysytrene (a),(c), particles at different heights.

Chapter 9

Conclusions and outlook

The main contribution of the second part of this dissertation is to, for the first time, investigate an optical trapping system for assembling an array of nanoparticles, where both the particle-trap interaction and particle-particle interaction play important roles. I also suggest that the system can be seen as "optical epitaxial growth". An array of optical traps serves as a growth substrate to provide a two-dimensional potential. However, the stable growth structure depends not only on the particle-substrate interaction but also the particle-particle interactions. I develop the model and simulation techniques to investigate the pattern formation and verify the theory by the experiment.

This work is the initial exploration of "optical epitaxial growth", a rich and intriguing system which has both scientific and technological interest. The analogy between our system and traditional epitaxial growth suggests various strategies for improving the quality of the photonic material. Optimization of the "growth temperature" (laser intensity) and growth rate (particle delivery rate), along with the use of annealing, may increase the size and quality of the particle array. An expanded range of complex materials could be grown using different types of nanoparticles (dielectric, metal, semiconductor, magnetic) as building blocks, offering a wide range of valuable physical properties. Moreover, the ability to observe the optical epitaxial growth process directly in both space and time suggests that our system could form a versatile model for studying interaction-driven dynamics in microscopic systems, such as cold atoms in optical lattices [130].

In this work, I mainly investigated the in-plane scattering (interaction) between particles and the formation of a two-dimensional array. However, the electromagnetic scattering process is a three-dimensional phenomenon. The interference of the scattered field from first layer of trapped particles may create strong optical trapping sites on top of them. The strongly trapped second layer particles have already been observed in both the chain formation [113] and cluster formation [125] experiments. Careful design of the template (substrate) may repeatedly foster the scattering process and enable three-dimensional optical epitaxial growth.

In the force analysis in Figure 8.7, strong field redistribution leads to strong optical force. Strong field redistribution effects can also be exploited to design hybrid modes at shorter wavelengths, close to the plasmon resonance. Figure 9.1(a) shows a resonant mode of the photonic-crystal slab close to 1320 nm, while Figure 9.1(b) shows the coupled localized surface plasmon resonance of the gold nanoparticle array. Hybridization [131] of the resonances (Figure 9.1(c)) produces a mode with enhanced field intensity and deep subwavelength mode volume. Analysis of the spectral response (Figure 9.1(d)) shows that the lineshape of the hybrid mode is narrower than either the photonic or plasmonic resonances. We note that the plasmonic resonance of the gold nanoparticle array is itself narrower than that of an isolated gold nanoparticle [132]. The entire system, namely the gold nanoparticle array assembled on top of the photonic-crystal template, can thus be viewed as a form of all-optically tunable, hybridized photonic-plasmonic matter.

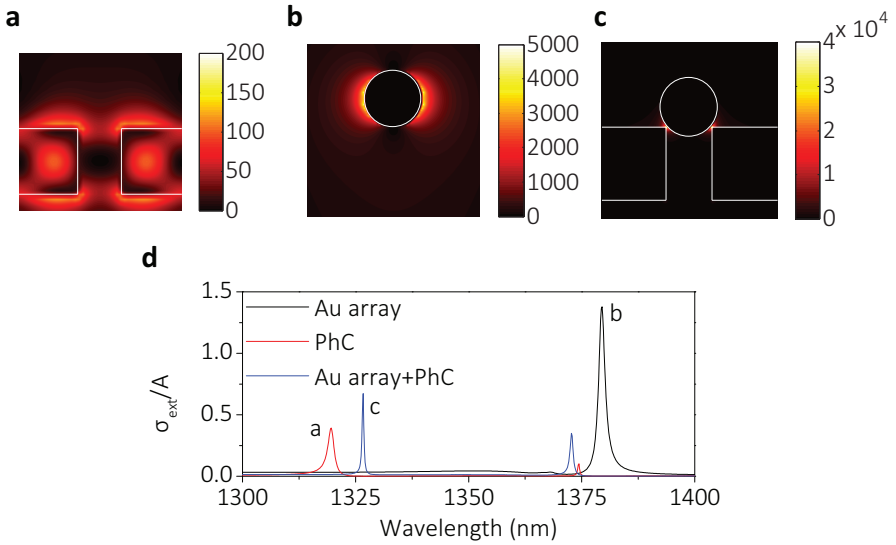

Figure 9.1: Hybridization of the photonic mode with the coupled plasmonic mode of the gold nanoparticle array. (a) Electric field intensity of a guided resonance mode in the photonic crystal slab. (b) Electric field intensity of a coupled plasmonic mode in the gold nanoparticle array. (c) Electric field intensity of a hybrid photonic-plasmonic mode between the trapped gold nanoparticle array and the photonic crystal trapping template. (d) The extinction cross-section spectrum of the structures shown in (a-c).

Reference List

[1] A. Standard, "G173, standard tables for reference solar spectral irradiances: Direct normal and hemispherical on 37 tilted surface," *Annual Book of ASTM Standards*, vol. 12, 2008.

[2] Wikipedia. Gallium arsenide. Wikipedia. [Online]. Available: http://en.wikipedia.org/wiki/Gallium_arsenide

[3] J. D. Joannopoulos, S. G. Johnson, J. N. Winn, and R. D. Meade, *Photonic crystals: molding the flow of light*. Princeton university press, 2011.

[4] (2015) Total solar irradiance data. University of Colorado Boulder. [Online]. Available: http://lasp.colorado.edu/home/sorce/data/tsi-data/

[5] (2015) International energy statistics, total primary energy consumption. U.S. Energy Information Administration. [Online]. Available: http://www.eia.gov/cfapps/ipdbproject/IEDIndex3.cfm?tid=44&pid=44&aid=2

[6] Wikipedia. (2015) Solar energy. [Online]. Available: http://en.wikipedia.org/wiki/Solar_energy

[7] E. P. I. Association *et al.*, "Global market outlook for photovoltaics 2014-2018," 2013.

[8] (2015) International energy statistics, total electricity installed capacity. U.S. Energy Information Administration. [Online]. Available: http://www.eia.gov/cfapps/ipdbproject/IEDIndex3.cfm?tid=2&pid=2&aid=7

[9] "Levelized cost and levelized avoided cost of new generation resources in the annual energy outlook 2014," *U.S. Energy Information Administration, Anuual Energy Outlook 2015*, 2015.

[10] N. Huang, C. Lin, and M. L. Povinelli, "Broadband absorption of semiconductor nanowire arrays for photovoltaic applications," *Journal of Optics*, vol. 14, no. 2, p. 024004, 2012.

[11] Y.-A. Dai, H.-C. Chang, K.-Y. Lai, C.-A. Lin, R.-J. Chung, G.-R. Lin, and J.-H. He, "Subwavelength Si nanowire arrays for self-cleaning antireflection coatings," *J. Mater. Chem.*, vol. 20, pp. 10 924–10 930, 2010.

[12] E. C. Garnett and P. Yang, "Silicon nanowire radial p-n junction solar cells," *Journal of the American Chemical Society*, vol. 130, no. 29, pp. 9224–9225, 2008.

[13] O. Gunawan and S. Guha, "Characteristics of vapor-liquid-solid grown silicon nanowire solar cells," *Solar Energy Materials and Solar Cells*, vol. 93, no. 8, pp. 1388 – 1393, 2009.

[14] K. Peng, Y. Xu, Y. Wu, Y. Yan, S.-T. Lee, and J. Zhu, "Aligned single-crystalline Si nanowire arrays for photovoltaic applications," *small*, vol. 1, no. 11, pp. 1062–1067, 2005.

[15] L. Tsakalakos, J. Balch, J. Fronheiser, B. Korevaar, O. Sulima, and J. Rand, "Silicon nanowire solar cells," *Applied Physics Letters*, vol. 91, no. 23, p. 233117, 2007.

[16] Y. Lu and A. Lal, "High-efficiency ordered silicon nano-conical-frustum array solar cells by self-powered parallel electron lithography," *Nano letters*, vol. 10, no. 11, pp. 4651–4656, 2010.

[17] M. D. Kelzenberg, D. B. Turner-Evans, M. C. Putnam, S. W. Boettcher, R. M. Briggs, J. Y. Baek, N. S. Lewis, and H. A. Atwater, "High-performance Si microwire photovoltaics," *Energy & Environmental Science*, vol. 4, no. 3, pp. 866–871, 2011.

[18] O. L. Muskens, J. G. Rivas, R. E. Algra, E. P. Bakkers, and A. Lagendijk, "Design of light scattering in nanowire materials for photovoltaic applications," *Nano Letters*, vol. 8, no. 9, pp. 2638–2642, 2008.

[19] T. Stelzner, M. Pietsch, G. Andrä, F. Falk, E. Ose, and S. Christiansen, "Silicon nanowire-based solar cells," *Nanotechnology*, vol. 19, no. 29, p. 295203, 2008.

[20] Z. Fan, R. Kapadia, P. W. Leu, X. Zhang, Y.-L. Chueh, K. Takei, K. Yu, A. Jamshidi, A. A. Rathore, D. J. Ruebusch *et al.*, "Ordered arrays of dual-diameter nanopillars for maximized optical absorption," *Nano letters*, vol. 10, no. 10, pp. 3823–3827, 2010.

[21] J. Caram, C. Sandoval, M. Tirado, D. Comedi, J. Czaban, D. Thompson, and R. LaPierre, "Electrical characteristics of core–shell p–n GaAs nanowire structures with te as the n-dopant," *Nanotechnology*, vol. 21, no. 13, p. 134007, 2010.

[22] G. Cirlin, A. Bouravleuv, I. Soshnikov, Y. B. Samsonenko, V. Dubrovskii, E. Arakcheeva, E. Tanklevskaya, and P. Werner, "Photovoltaic properties of p-doped GaAs nanowire arrays grown on n-type GaAs (111) B substrate," *Nanoscale research letters*, vol. 5, no. 2, pp. 360–363, 2010.

[23] C. Colombo, M. Heiβ, M. Gratzel, and A. F. Morral, "Gallium arsenide pin radial structures for photovoltaic applications," *Applied Physics Letters*, vol. 94, no. 17, pp. 173 108–173 108, 2009.

[24] S. L. Diedenhofen, O. T. Janssen, G. Grzela, E. P. Bakkers, and J. GoÌĄmez Rivas, "Strong geometrical dependence of the absorption of light in arrays of semiconductor nanowires," *ACS nano*, vol. 5, no. 3, pp. 2316–2323, 2011.

[25] A. Pierret, M. Hocevar, S. L. Diedenhofen, R. E. Algra, E. Vlieg, E. C. Timmering, M. A. Verschuuren, G. W. Immink, M. A. Verheijen, and E. P. Bakkers, "Generic nano-imprint process for fabrication of nanowire arrays," *Nanotechnology*, vol. 21, no. 6, p. 065305, 2010.

[26] Z. Fan, H. Razavi, J.-w. Do, A. Moriwaki, O. Ergen, Y.-L. Chueh, P. W. Leu, J. C. Ho, T. Takahashi, L. A. Reichertz *et al.*, "Three-dimensional nanopillar-array photovoltaics on low-cost and flexible substrates," *Nature materials*, vol. 8, no. 8, pp. 648–653, 2009.

[27] H. Goto, K. Nosaki, K. Tomioka, S. Hara, K. Hiruma, J. Motohisa, and T. Fukui, "Growth of core–shell InP nanowires for photovoltaic application by selective-area metal organic vapor phase epitaxy," *Applied Physics Express*, vol. 2, no. 3, p. 035004, 2009.

[28] J. Zhu, Z. Yu, G. F. Burkhard, C.-M. Hsu, S. T. Connor, Y. Xu, Q. Wang, M. McGehee, S. Fan, and Y. Cui, "Optical absorption enhancement in amorphous silicon nanowire and nanocone arrays," *Nano letters*, vol. 9, no. 1, pp. 279–282, 2008.

[29] A. Gu, Y. Huo, S. Hu, T. Sarmiento, E. Pickett, D. Liang, S. Li, A. Lin, S. Thombare, Z. Yu *et al.*, "Design and growth of III–V nanowire solar cell arrays on low cost substrates," in *Photovoltaic Specialists Conference (PVSC), 2010 35th IEEE*. IEEE, 2010, pp. 002 034–002 037.

[30] A. C. Tamboli, D. B. Turner-Evans, M. Malhotra, M. D. Kelzenberg, and H. A. Atwater, "GaP/Si wire array solar cells," in *Photovoltaic Specialists Conference (PVSC), 2010 35th IEEE*. IEEE, 2010, pp. 000 918–000 922.

[31] M. Adachi, M. Anantram, and K. Karim, "Optical properties of crystalline-amorphous core- shell silicon nanowires," *Nano letters*, vol. 10, no. 10, pp. 4093–4098, 2010.

[32] O. Gunawan, K. Wang, B. Fallahazad, Y. Zhang, E. Tutuc, and S. Guha, "High performance wire-array silicon solar cells," *Progress in Photovoltaics: Research and Applications*, vol. 19, no. 3, pp. 307–312, 2011.

[33] E. Garnett and P. Yang, "Light trapping in silicon nanowire solar cells," *Nano letters*, vol. 10, no. 3, pp. 1082–1087, 2010.

[34] H. Bi and R. LaPierre, "A GaAs nanowire/P3HT hybrid photovoltaic device," *Nanotechnology*, vol. 20, no. 46, p. 465205, 2009.

[35] J.-J. Chao, S.-C. Shiu, S.-C. Hung, and C.-F. Lin, "Gaas nanowire/poly (3, 4-ethylenedioxythiophene): poly (styrenesulfonate) hybrid solar cells," *Nanotechnology*, vol. 21, no. 28, p. 285203, 2010.

[36] L. Hu and G. Chen, "Analysis of optical absorption in silicon nanowire arrays for photovoltaic applications," *Nano letters*, vol. 7, no. 11, pp. 3249–3252, 2007.

[37] C. Lin and M. L. Povinelli, "Optical absorption enhancement in silicon nanowire arrays with a large lattice constant for photovoltaic applications," *Optics express*, vol. 17, no. 22, pp. 19 371–19 381, 2009.

[38] J. Li, H. Yu, S. M. Wong, G. Zhang, X. Sun, P. G.-Q. Lo, and D.-L. Kwong, "Si nanopillar array optimization on Si thin films for solar energy harvesting," *Applied Physics Letters*, vol. 95, no. 3, p. 033102, 2009.

[39] J. Kupec and B. Witzigmann, "Dispersion, wave propagation and efficiency analysis of nanowire solar cells," *Optics express*, vol. 17, no. 12, pp. 10 399–10 410, 2009.

[40] N. Anttu and H. Xu, "Coupling of light into nanowire arrays and subsequent absorption," *Journal of nanoscience and nanotechnology*, vol. 10, no. 11, pp. 7183–7187, 2010.

[41] Z. Gu, P. Prete, N. Lovergine, and B. Nabet, "On optical properties of GaAs and GaAs/AlGaAs core-shell periodic nanowire arrays," *Journal of Applied Physics*, vol. 109, no. 6, p. 064314, 2011.

[42] E. D. Palik, *Handbook of optical constants of solids*. Academic press, 1998, vol. 3.

[43] Filmetrics. (2011) Refractive index database. [Online]. Available: www.filmetrics.com/refractive-index-database

[44] S. Adachi, *Properties of semiconductor alloys: group-IV, III-V and II-VI semiconductors*. John Wiley & Sons, 2009, vol. 28.

[45] ——, *Optical constants of crystalline and amorphous semiconductors: numerical data and graphical information*. Springer Science & Business Media, 1999.

[46] M. Li, X. Hu, Z. Ye, K.-M. Ho, J. Cao, and M. Miyawaki, "Higher-order incidence transfer matrix method used in three-dimensional photonic crystal coupled-resonator array simulation," *Optics letters*, vol. 31, no. 23, pp. 3498–3500, 2006.

[47] M. Li, Z. Li, K.-M. Ho, J. Cao, and M. Miyawaki, "High-efficiency calculations for three-dimensional photonic crystal cavities," *Optics letters*, vol. 31, no. 2, pp. 262–264, 2006.

[48] J. Pendry, "Photonic band structures," *Journal of Modern Optics*, vol. 41, no. 2, pp. 209–229, 1994.

[49] D. Whittaker and I. Culshaw, "Scattering-matrix treatment of patterned multilayer photonic structures," *Physical Review B*, vol. 60, no. 4, p. 2610, 1999.

[50] W. Shockley and H. J. Queisser, "Detailed balance limit of efficiency of p-n junction solar cells," *Journal of applied physics*, vol. 32, no. 3, pp. 510–519, 1961.

[51] N. Huang, C. Lin, and M. L. Povinelli, "Limiting efficiencies of tandem solar cells consisting of iii-v nanowire arrays on silicon," *Journal of Applied Physics*, vol. 112, no. 6, p. 064321, 2012.

[52] T. J. Kempa, B. Tian, D. R. Kim, J. Hu, X. Zheng, and C. M. Lieber, "Single and tandem axial pin nanowire photovoltaic devices," *Nano letters*, vol. 8, no. 10, pp. 3456–3460, 2008.

[53] M. Heurlin, P. Wickert, S. FaÌĺlt, M. T. BorgstroÌĺm, K. Deppert, L. Samuelson, and M. H. Magnusson, "Axial InP nanowire tandem junction grown on a silicon substrate," *Nano letters*, vol. 11, no. 5, pp. 2028–2031, 2011.

[54] A. Kandala, T. Betti, and A. Fontcuberta i Morral, "General theoretical considerations on nanowire solar cell designs," *physica status solidi (a)*, vol. 206, no. 1, pp. 173–178, 2009.

[55] C. H. Henry, "Limiting efficiencies of ideal single and multiple energy gap terrestrial solar cells," *Journal of applied physics*, vol. 51, no. 8, pp. 4494–4500, 1980.

[56] M. S. Gudiksen, L. J. Lauhon, J. Wang, D. C. Smith, and C. M. Lieber, "Growth of nanowire superlattice structures for nanoscale photonics and electronics," *Nature*, vol. 415, no. 6872, pp. 617–620, 2002.

[57] F. Glas, "Critical dimensions for the plastic relaxation of strained axial heterostructures in free-standing nanowires," *Physical Review B*, vol. 74, no. 12, p. 121302, 2006.

[58] S. Sburlan, P. D. Dapkus, and A. Nakano, "Critical dimensions of highly lattice mismatched semiconductor nanowires grown in strain-releasing configurations," *Applied Physics Letters*, vol. 100, no. 16, p. 163108, 2012.

[59] A. R. Madaria, M. Yao, C. Chi, N. Huang, C. Lin, R. Li, M. L. Povinelli, P. D. Dapkus, and C. Zhou, "Toward optimized light utilization in nanowire arrays using scalable nanosphere lithography and selected area growth," *Nano letters*, vol. 12, no. 6, pp. 2839–2845, 2012.

[60] J. C. Shin, K. H. Kim, K. J. Yu, H. Hu, L. Yin, C.-Z. Ning, J. A. Rogers, J.-M. Zuo, and X. Li, "In x Ga1-x As nanowires on silicon: One-dimensional heterogeneous epitaxy, bandgap engineering, and photovoltaics," *Nano letters*, vol. 11, no. 11, pp. 4831–4838, 2011.

[61] T. Mårtensson, C. P. T. Svensson, B. A. Wacaser, M. W. Larsson, W. Seifert, K. Deppert, A. Gustafsson, L. R. Wallenberg, and L. Samuelson, "Epitaxial III-V nanowires on silicon," *Nano Letters*, vol. 4, no. 10, pp. 1987–1990, 2004.

[62] C. P. T. Svensson, T. Mårtensson, J. Trägårdh, C. Larsson, M. Rask, D. Hessman, L. Samuelson, and J. Ohlsson, "Monolithic GaAs/InGaP nanowire light emitting diodes on silicon," *Nanotechnology*, vol. 19, no. 30, p. 305201, 2008.

[63] K. Tomioka, Y. Kobayashi, J. Motohisa, S. Hara, and T. Fukui, "Selective-area growth of vertically aligned GaAs and GaAs/AlGaAs core–shell nanowires on Si (111) substrate," *Nanotechnology*, vol. 20, no. 14, p. 145302, 2009.

[64] J. C. Shin, K. H. Kim, H. Hu, K. J. Yu, J. A. Rogers, J.-M. Zuo, and X. Li, "Monolithically grown In x Ga 1- x As nanowire array on silicon tandem solar cells with high efficiency," in *Photonics Conference (PHO), 2011 IEEE*. IEEE, 2011, pp. 391–392.

[65] S. R. Kurtz, P. Faine, and J. Olson, "Modeling of two-junction, series-connected tandem solar cells using top-cell thickness as an adjustable parameter," *Journal of Applied Physics*, vol. 68, no. 4, pp. 1890–1895, 1990.

[66] S. M. Sze and K. K. Ng, *Physics of semiconductor devices*. John Wiley & Sons, 2006.

[67] R. LaPierre, "Numerical model of current-voltage characteristics and efficiency of GaAs nanowire solar cells," *Journal of Applied Physics*, vol. 109, no. 3, p. 034311, 2011.

[68] O. Demichel, M. Heiss, J. Bleuse, H. Mariette, and A. F. i Morral, "Impact of surfaces on the optical properties of GaAs nanowires," *Applied Physics Letters*, vol. 97, no. 20, p. 201907, 2010.

[69] C.-C. Chang, C.-Y. Chi, M. Yao, N. Huang, C.-C. Chen, J. Theiss, A. W. Bushmaker, S. LaLumondiere, T.-W. Yeh, M. L. Povinelli *et al.*, "Electrical and optical characterization of surface passivation in GaAs nanowires," *Nano letters*, vol. 12, no. 9, pp. 4484–4489, 2012.

[70] N. Huang and M. Povinelli, "Design of passivation layers on axial junction gaas nanowire solar cells," *Photovoltaics, IEEE Journal of*, vol. 4, no. 6, pp. 1511–1517, Nov 2014.

[71] L. Wen, X. Li, Z. Zhao, S. Bu, X. Zeng, J.-h. Huang, and Y. Wang, "Theoretical consideration of III–V nanowire/Si triple-junction solar cells," *Nanotechnology*, vol. 23, no. 50, p. 505202, 2012.

[72] R. LaPierre, "Theoretical conversion efficiency of a two-junction III-V nanowire on Si solar cell," *Journal of Applied Physics*, vol. 110, no. 1, p. 014310, 2011.

[73] D. Aspnes, "Recombination at semiconductor surfaces and interfaces," *Surface Science*, vol. 132, no. 1, pp. 406–421, 1983.

[74] D. S. Mui and L. Coldren, "Effects of surface recombination on carrier distributions and device characteristics," *Journal of applied physics*, vol. 78, no. 5, pp. 3208–3215, 1995.

[75] J. A. Czaban, D. A. Thompson, and R. R. LaPierre, "Gaas core- shell nanowires for photovoltaic applications," *Nano Letters*, vol. 9, no. 1, pp. 148–154, 2008.

[76] G. Mariani, A. C. Scofield, C.-H. Hung, and D. L. Huffaker, "Gaas nanopillar-array solar cells employing in situ surface passivation," *Nature communications*, vol. 4, p. 1497, 2013.

[77] G. Mariani, P.-S. Wong, A. M. Katzenmeyer, F. Léonard, J. Shapiro, and D. L. Huffaker, "Patterned radial GaAs nanopillar solar cells," *Nano letters*, vol. 11, no. 6, pp. 2490–2494, 2011.

[78] C. Gutsche, A. Lysov, D. Braam, I. Regolin, G. Keller, Z.-A. Li, M. Geller, M. Spasova, W. Prost, and F.-J. Tegude, "n-GaAs/InGaP/p-GaAs core-multishell nanowire diodes for efficient light-to-current conversion," *Advanced Functional Materials*, vol. 22, no. 5, pp. 929–936, 2012.

[79] E. Nakai, M. Yoshimura, K. Tomioka, and T. Fukui, "GaAs/InGaP core–multishell nanowire-array-based solar cells," *Japanese Journal of Applied Physics*, vol. 52, no. 5R, p. 055002, 2013.

[80] J. Wallentin, N. Anttu, D. Asoli, M. Huffman, I. Åberg, M. H. Magnusson, G. Siefer, P. Fuss-Kailuweit, F. Dimroth, B. Witzigmann *et al.*, "InP nanowire array solar cells achieving 13.8% efficiency by exceeding the ray optics limit," *Science*, vol. 339, no. 6123, pp. 1057–1060, 2013.

[81] Y. Cui, J. Wang, S. R. Plissard, A. Cavalli, T. T. Vu, R. P. van Veldhoven, L. Gao, M. Trainor, M. A. Verheijen, J. E. Haverkort *et al.*, "Efficiency enhancement of InP nanowire solar cells by surface cleaning," *Nano letters*, vol. 13, no. 9, pp. 4113–4117, 2013.

[82] H. J. Joyce, C. J. Docherty, Q. Gao, H. H. Tan, C. Jagadish, J. Lloyd-Hughes, L. M. Herz, and M. B. Johnston, "Electronic properties of GaAs, InAs and InP nanowires studied by terahertz spectroscopy," *Nanotechnology*, vol. 24, no. 21, p. 214006, 2013.

[83] H. Hasegawa and M. Akazawa, "Surface passivation technology for III–V semiconductor nanoelectronics," *Applied Surface Science*, vol. 255, no. 3, pp. 628–632, 2008.

[84] N. Tajik, Z. Peng, P. Kuyanov, and R. LaPierre, "Sulfur passivation and contact methods for GaAs nanowire solar cells," *Nanotechnology*, vol. 22, no. 22, p. 225402, 2011.

[85] C. K. Yong, K. Noori, Q. Gao, H. J. Joyce, H. H. Tan, C. Jagadish, F. Giustino, M. B. Johnston, and L. M. Herz, "Strong carrier lifetime enhancement in gaas nanowires coated with semiconducting polymer," *Nano letters*, vol. 12, no. 12, pp. 6293–6301, 2012.

[86] N. Jiang, Q. Gao, P. Parkinson, J. Wong-Leung, S. Mokkapati, S. Breuer, H. Tan, C. Zheng, J. Etheridge, and C. Jagadish, "Enhanced minority carrier lifetimes in GaAs/AlGaAs core–shell nanowires through shell growth optimization," *Nano letters*, vol. 13, no. 11, pp. 5135–5140, 2013.

[87] L. Molenkamp and H. VanâĂŹt Blik, "Very low interface recombination velocity in (Al, Ga) As heterostructures grown by organometallic vapor-phase epitaxy," *Journal of applied physics*, vol. 64, no. 8, pp. 4253–4256, 1988.

[88] W. Mönch, *Semiconductor surfaces and interfaces*. Springer Science & Business Media, 2001, vol. 26.

[89] R. Dingle, H. Störmer, A. Gossard, and W. Wiegmann, "Electron mobilities in modulation-doped semiconductor heterojunction superlattices," *Applied Physics Letters*, vol. 33, no. 7, pp. 665–667, 1978.

[90] G. Gilliland, D. Wolford, T. Kuech, J. Bradley, and H. Hjalmarson, "Minority-carrier recombination kinetics and transport in "surface-free"GaAs/AlxGa1- xAs double heterostructures," *Journal of applied physics*, vol. 73, no. 12, pp. 8386–8396, 1993.

[91] M. Yao, N. Huang, S. Cong, C.-Y. Chi, M. A. Seyedi, Y.-T. Lin, Y. Cao, M. L. Povinelli, P. D. Dapkus, and C. Zhou, "GaAs nanowire array solar cells with axial p–i–n junctions," *Nano letters*, vol. 14, no. 6, pp. 3293–3303, 2014.

[92] M. Yao, S. Cong, S. Arab, N. Huang, M. L. Povinelli, S. B. Cronin, P. D. Dapkus, and C. Zhou, "Tandem solar cells using GaAs nanowires on Si: Design, fabrication, and observation of voltage addition," *submitted for review*, 2015.

[93] A. Ashkin, J. Dziedzic, J. Bjorkholm, and S. Chu, "Observation of a single-beam gradient force optical trap for dielectric particles," *Optics letters*, vol. 11, no. 5, pp. 288–290, 1986.

[94] A. Ashkin, J. Dziedzic, and T. Yamane, "Optical trapping and manipulation of single cells using infrared laser beams," *Nature*, vol. 330, no. 6150, pp. 769–771, 1987.

[95] O. M. Maragò, P. H. Jones, P. G. Gucciardi, G. Volpe, and A. C. Ferrari, "Optical trapping and manipulation of nanostructures," *Nature nanotechnology*, vol. 8, no. 11, pp. 807–819, 2013.

[96] M.-C. Zhong, X.-B. Wei, J.-H. Zhou, Z.-Q. Wang, and Y.-M. Li, "Trapping red blood cells in living animals using optical tweezers," *Nature communications*, vol. 4, p. 1768, 2013.

[97] X. Wang, S. Chen, M. Kong, Z. Wang, K. D. Costa, R. A. Li, and D. Sun, "Enhanced cell sorting and manipulation with combined optical tweezer and microfluidic chip technologies," *Lab on a Chip*, vol. 11, no. 21, pp. 3656–3662, 2011.

[98] H. Zhang and K.-K. Liu, "Optical tweezers for single cells," *Journal of The Royal Society Interface*, vol. 5, no. 24, pp. 671–690, 2008.

[99] A. Grigorenko, N. Roberts, M. Dickinson, and Y. Zhang, "Nanometric optical tweezers based on nanostructured substrates," *Nature Photonics*, vol. 2, no. 6, pp. 365–370, 2008.

[100] A. H. Yang, S. D. Moore, B. S. Schmidt, M. Klug, M. Lipson, and D. Erickson, "Optical manipulation of nanoparticles and biomolecules in sub-wavelength slot waveguides," *Nature*, vol. 457, no. 7225, pp. 71–75, 2009.

[101] K. Svoboda and S. M. Block, "Optical trapping of metallic rayleigh particles," *Optics letters*, vol. 19, no. 13, pp. 930–932, 1994.

[102] P. M. Hansen, V. K. Bhatia, N. Harrit, and L. Oddershede, "Expanding the optical trapping range of gold nanoparticles," *Nano letters*, vol. 5, no. 10, pp. 1937–1942, 2005.

[103] S. Lin, W. Zhu, Y. Jin, and K. B. Crozier, "Surface-enhanced raman scattering with ag nanoparticles optically trapped by a photonic crystal cavity," *Nano letters*, vol. 13, no. 2, pp. 559–563, 2013.

[104] D. G. Grier, "A revolution in optical manipulation," *Nature*, vol. 424, no. 6950, pp. 810–816, 2003.

[105] M. M. Burns, J.-M. Fournier, and J. A. Golovchenko, "Optical matter: crystallization and binding in intense optical fields," *Science*, vol. 249, no. 4970, pp. 749–754, 1990.

[106] M. MacDonald, G. Spalding, and K. Dholakia, "Microfluidic sorting in an optical lattice," *Nature*, vol. 426, no. 6965, pp. 421–424, 2003.

[107] M. Werner, F. Merenda, J. Piguet, R.-P. Salathé, and H. Vogel, "Microfluidic array cytometer based on refractive optical tweezers for parallel trapping, imaging and sorting of individual cells," *Lab on a Chip*, vol. 11, no. 14, pp. 2432–2439, 2011.

[108] E. Jaquay, L. J. Martínez, C. A. Mejia, and M. L. Povinelli, "Light-assisted, templated self-assembly using a photonic-crystal slab," *Nano letters*, vol. 13, no. 5, pp. 2290–2294, 2013.

[109] M. Soltani, J. Lin, R. A. Forties, J. T. Inman, S. N. Saraf, R. M. Fulbright, M. Lipson, and M. D. Wang, "Nanophotonic trapping for precise manipulation of biomolecular arrays," *Nature nanotechnology*, vol. 9, no. 6, pp. 448–452, 2014.

[110] M. Righini, A. S. Zelenina, C. Girard, and R. Quidant, "Parallel and selective trapping in a patterned plasmonic landscape," *Nature Physics*, vol. 3, no. 7, pp. 477–480, 2007.

[111] U. Mirsaidov, J. Scrimgeour, W. Timp, K. Beck, M. Mir, P. Matsudaira, and G. Timp, "Live cell lithography: using optical tweezers to create synthetic tissue," *Lab on a Chip*, vol. 8, no. 12, pp. 2174–2181, 2008.

[112] E. McLeod and C. B. Arnold, "Array-based optical nanolithography using optically trapped microlenses," *Optics express*, vol. 17, no. 5, pp. 3640–3650, 2009.

[113] E. Jaquay, L. J. Martínez, N. Huang, C. A. Mejia, D. Sarkar, and M. L. Povinelli, "Light-assisted, templated self-assembly of gold nanoparticle chains," *Nano letters*, vol. 14, no. 9, pp. 5184–5188, 2014.

[114] L. Wong and C. Bain, "Optical trapping and binding in evanescent optical landscapes," in *SPIE NanoScience+ Engineering*. International Society for Optics and Photonics, 2009, pp. 74 001F–74 001F.

[115] N. Felidj, J. Aubard, G. Levi, J. Krenn, A. Hohenau, G. Schider, A. Leitner, and F. Aussenegg, "Optimized surface-enhanced raman scattering on gold nanoparticle arrays," *Applied Physics Letters*, vol. 82, no. 18, pp. 3095–3097, 2003.

[116] H. Jiang, T. Li, J. Yang, S. Mittler, and J. Sabarinathan, "Optimization of gold nanoring arrays for biosensing in the fiber-optic communication window," *Nanotechnology*, vol. 24, no. 46, p. 465502, 2013.

[117] W. Zhou, M. Dridi, J. Y. Suh, C. H. Kim, D. T. Co, M. R. Wasielewski, G. C. Schatz, T. W. Odom *et al.*, "Lasing action in strongly coupled plasmonic nanocavity arrays," *Nature nanotechnology*, vol. 8, no. 7, pp. 506–511, 2013.

[118] P. Chaumet and M. Nieto-Vesperinas, "Optical binding of particles with or without the presence of a flat dielectric surface," *Physical Review B*, vol. 64, no. 3, p. 035422, 2001.

[119] V. Demergis and E.-L. Florin, "Ultrastrong optical binding of metallic nanoparticles," *Nano letters*, vol. 12, no. 11, pp. 5756–5760, 2012.

[120] Z. Yan, S. K. Gray, and N. F. Scherer, "Potential energy surfaces and reaction pathways for light-mediated self-organization of metal nanoparticle clusters," *Nature communications*, vol. 5, 2014.

[121] K. Dholakia and P. Zemánek, "Colloquium: gripped by light: optical binding," *Reviews of modern physics*, vol. 82, no. 2, p. 1767, 2010.

[122] C. A. Mejia, A. Dutt, and M. L. Povinelli, "Light-assisted templated self assembly using photonic crystal slabs," *Optics express*, vol. 19, no. 12, pp. 11 422–11 428, 2011.

[123] E. Yablonovitch, "Inhibited spontaneous emission in solid-state physics and electronics," *Physical review letters*, vol. 58, no. 20, p. 2059, 1987.

[124] S. John, "Strong localization of photons in certain disordered dielectric superlattices," *Physical review letters*, vol. 58, no. 23, p. 2486, 1987.

[125] N. Huang, L. J. Martínez, A. Jaquay, Eric Nakano, and M. L. Povinelli, "Optical epitaxial growth of gold nanoparticle arrays," *submitted for review*, 2015.

[126] L. J. Martínez, B. AlÚn, I. Prieto, J. Galisteo-LËĞpez, M. Galli, L. C. Andreani, C. Seassal, P. Viktorovitch, and P. A. Postigo, "Two-dimensional surface emitting photonic crystal laser with hybrid triangular-graphite structure," *Optics express*, vol. 17, no. 17, pp. 15 043–15 051, 2009.

[127] N. Huang, L. J. Martínez, and M. L. Povinelli, "Tuning the transmission lineshape of a photonic crystal slab guided-resonance mode by polarization control," *Optics express*, vol. 21, no. 18, pp. 20 675–20 682, 2013.

[128] J. D. Jackson and J. D. Jackson, *Classical electrodynamics*. Wiley New York etc., 1962, vol. 3.

[129] C. Min, Z. Shen, J. Shen, Y. Zhang, H. Fang, G. Yuan, L. Du, S. Zhu, T. Lei, and X. Yuan, "Focused plasmonic trapping of metallic particles," *Nature communications*, vol. 4, 2013.

[130] L. Hackermüller, U. Schneider, M. Moreno-Cardoner, T. Kitagawa, T. Best, S. Will, E. Demler, E. Altman, I. Bloch, and B. Paredes, "Anomalous expansion of attractively interacting fermionic atoms in an optical lattice," *Science*, vol. 327, no. 5973, pp. 1621–1624, 2010.

[131] X. Yang, A. Ishikawa, X. Yin, and X. Zhang, "Hybrid photonic- plasmonic crystal nanocavities," *ACS nano*, vol. 5, no. 4, pp. 2831–2838, 2011.

[132] B. Auguié and W. L. Barnes, "Collective resonances in gold nanoparticle arrays," *Physical review letters*, vol. 101, no. 14, p. 143902, 2008.

[133] L. Novotny and B. Hecht, *Principles of nano-optics*. Cambridge university press, 2012.

[134] Z. Yan, R. A. Shah, G. Chado, S. K. Gray, M. Pelton, and N. F. Scherer, "Guiding spatial arrangements of silver nanoparticles by optical binding interactions in shaped light fields," *ACS nano*, vol. 7, no. 2, pp. 1790–1802, 2013.

[135] C. F. Bohren and D. R. Huffman, *Absorption and scattering of light by small particles*. John Wiley & Sons, 2008.

Appendix A

Supporting Information of Optical Potential Calculation

A.1 Numerical Calculation of the Polarizability

When a small particle is positioned in electromagnetic field, the field will induce dipole moment at the particle's position. The relation between the induced dipole moment ($\mathbf{p}$) and the local electric field ($\mathbf{E}_0$) is defined as

$$\mathbf{p} = \alpha \mathbf{E}_0 \tag{A.1}$$

where α is the *polarizability* of the particle. In electrostatic approximation, the polarizability can be written using the permittivities of the particle material (ϵ_1) and the surrounding medium (ϵ_m).

$$\alpha = 4\pi\epsilon_m a^3 \frac{\epsilon_1 - \epsilon_m}{\epsilon_1 + 2\epsilon_m} \tag{A.2}$$

Equation A.2 is only valid for small particles with diameter much smaller than the wavelength of the light. For larger particle which is considered in this dissertation, this equation need to be corrected by considering the radiation reaction [133]. Full-vector FDTD simulations can also be used to obtain a more accurate value of polarizability [134].

In the electrostatics approxmiation, the absorption and scattering efficiencies of a small sphere may be written [135]

$$Q_{abs} = 4x\Im\frac{\epsilon_1 - \epsilon_m}{\epsilon_1 + 2\epsilon_m} \tag{A.3}$$

$$Q_{sca} = \frac{8}{3}x^4\left|\frac{\epsilon_1 - \epsilon_m}{\epsilon_1 + 2\epsilon_m}\right|^2 \tag{A.4}$$

where $x = ka = 2\pi Na/\lambda$ is the *size parameter*. The cross-sections can be obtained by numerical (FDTD) simulation by monitoring the scattered power around a particle. Once the absorption and scattering efficiencies are obtained, we can calculate the polarizability by using Equation A.2, A.3 and A.4. The polarizability of a 200 nm diameter gold particle in water is calculated to be $(2.37 - 0.033j) \times 10^{-31}(\mathrm{Cm}^2/\mathrm{V})$.

A.2 Full-vector force simulation versus the dipole approximation

In Chapter 7, we characterize the interaction between particles by introducing the energy shift written as Equation 7.13. The derivative of the potential energy is the optical force. In this section, we compare the force generated by taking the derivative of Equation 7.13 and the force simulated by FDTD and Maxwell stress-tensor formula. For the full-vector FDTD simulation, we put a 200 nm diameter gold particle in the simulation region and put a total-field-scattered-field source to shine the plane-wave onto it. A cubic field monitor is put around the particle to monitor the electromagnetic field and the force is calculated by the Maxwell stress-tensor formula. For the dipole approximation, we take the derivative of Equation 7.12.

Figure A.1 shows the comparison result. Figure A.1 (a) shows the optical force between two particles in water, which is the same case shown in Figure 7.8 (a). The result for the light polarization along both directions is shown. In this case, the forces calculated by FDTD simulation and by the dipole approximation are nearly identical with each other for both polarization cases without any correction. Figure A.1 (b) show the optical force between particles with the center 125 nm above a 250 nm SOI wafer. For a 200 nm diameter particle, the bottom of the particle is 25 nm above the slab. For the dipole approximation, the Green's function is calculated by putting the dipole 125 nm above the slab. The FDTD simulation and the dipole approximation are still similar, with all the features recovered.

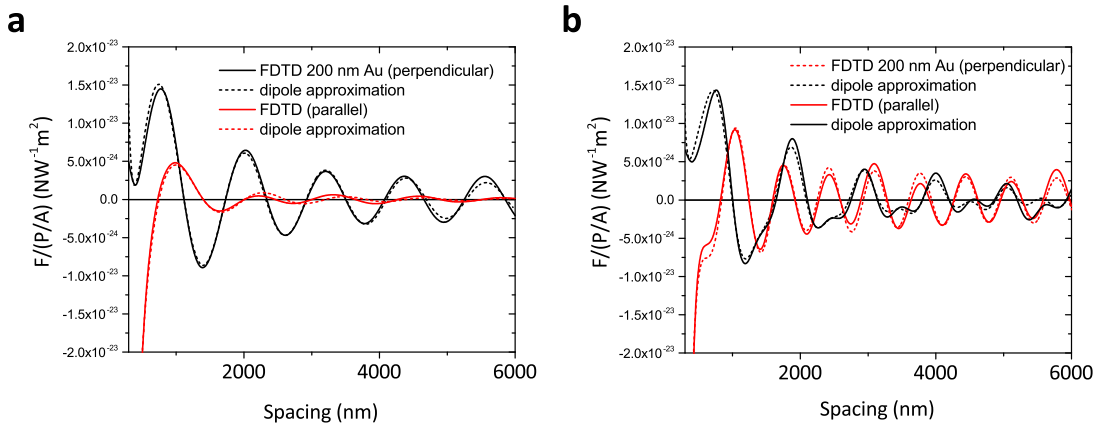

Figure A.1: Comparison between the full-vector force simulation versus the dipole approximation energy formula. (a) the optical force between two particles in water. (b) the optical force between two particles in water on a plane 125 nm above a 250 nm SOI.

This comparison validates the usage of the dipole approximation (Equation 7.12 and 7.13) in this work. It also shows that the secondary multiple scattering is negligible. In Figure A.1, only the first scattering is considered in dipole approximation.

A.3 The effect of holes on the photonic-crystal slab

In this work, we approximate the Green's function of a photonic-crystal slab to a Green's function on an uniform slab without holes in it. The simulation method introduced in Section 7.2 can be used to simulate the Green's function in any kind of environment including the case on top of a photonic-crystal slab. The reason that I made this approximation is that in Chapter 7, I investigate photonic-crystal templates with a wide range of lattice constant (from $0.8a$ to $1.1a$). For a certain lattice constant, the photonic-crystal slab needs to be carefully designed to support a guided-resonance mode around the operating wavelength of the laser ($\sim$ 1550 nm), and sometimes it becomes very challenging. The approximation to an uniform slab makes the systematic study shown in Figure 7.6 possible.

To validate this approximation, we design a photonic crystal template with a lattice constant of 1.1 μm that supports a guided resonance at 1558 nm. The template has a perturbed square lattice similar to the one used in Ref [113]. The radii of the big and small holes are 80 nm and 70 nm, respectively. Figure A.2 (a) shows the Green's function for a dipole at 125 nm above the surface of the photonic-crystal slab. The holes are also drawn on top of the Green's function. Figure A.2 (b) shows the Green's function for a dipole 125 nm above an uniform slab at the same wavelength. The dots only indicate the position of the large holes. The holes on the photonic-crystal slab perturb the Green's function slightly, however, the main features, especially for the position closest to the center dipole, remain. The amplitude is also similar.

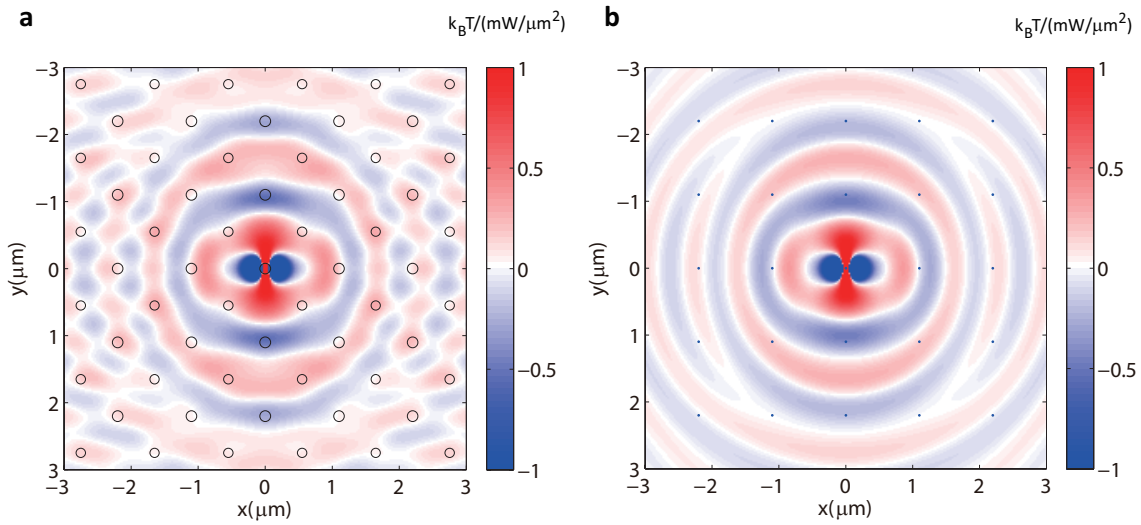

Figure A.2: Comparison between the Green's function on a photonic-crystal slab (a) and on an uniform slab (b).